

1 **The linked complexity of coseismic and postseismic**
2 **faulting revealed by seismo-geodetic dynamic inversion**
3 **of the 2004 Parkfield earthquake**

4 Nico Schliwa ¹, Alice-Agnes Gabriel ^{2,1}, Jan Premus ³, František Gallovič ⁴

5 ¹Ludwig-Maximilians-Universität München, Munich, Germany

6 ²Scripps Institution of Oceanography, UC San Diego, La Jolla, CA, USA

7 ³Côte d'Azur University, Nice, France

8 ⁴Charles University, Prague, Czech Republic

9 This is a non-peer-reviewed preprint submitted to EarthArXiv.

10 **Key Points:**

- 11 • We perform a joint seismo-geodetic dynamic rupture and afterslip inversion of the
12 2004 Parkfield event.
- 13 • We find that coseismic rupture is separated into a strongly radiating pulse-like and
14 a mildly radiating crack-like phase.
- 15 • Distinct dynamic rupture arrest mechanisms imprint on afterslip evolution and
16 afterslip may drive delayed aftershocks.

Corresponding author: Nico Schliwa, nico.schliwa@lmu.de

Abstract

Several regularly recurring moderate-size earthquakes motivated dense instrumentation of the Parkfield section of the San Andreas fault, providing an invaluable near-fault observatory. We present a seismo-geodetic dynamic inversion of the 2004 Parkfield earthquake, which illuminates the interlinked complexity of faulting across time scales. Using fast-velocity-weakening rate-and-state friction, we jointly model coseismic dynamic rupture and the 90-day evolution of postseismic slip in a 3D domain. We utilize a parallel tempering Markov chain Monte Carlo approach to solve this non-linear high-dimensional inverse problem, constraining spatially varying prestress and fault friction parameters by 30 strong motion and 12 GPS stations. From visiting >2 million models, we discern complex coseismic rupture dynamics that transition from a strongly radiating pulse-like phase to a mildly radiating crack-like phase. Both coseismic phases are separated by a shallow strength barrier that nearly arrests rupture and leads to a gap in the afterslip, reflecting the geologic heterogeneity along this segment of the San Andreas Fault. Coseismic rupture termination involves distinct arrest mechanisms that imprint on afterslip kinematics. A backward propagating afterslip front may drive delayed aftershock activity above the hypocenter. Trade-off analysis of the 10,500 best-fitting models uncovers local correlations between prestress levels and the reference friction coefficient, alongside an anticorrelation between prestress and rate-state parameters $b-a$. We find that a complex, fault-local interplay of dynamic parameters determines the nucleation, propagation, and arrest of both, co- and postseismic faulting. This study demonstrates the potential of inverse physics-based modeling to reveal novel insights and detailed characterizations of well-recorded earthquakes.

Plain Language Summary

The Parkfield section of the San Andreas plate boundary hosts regularly recurring moderate-size earthquakes. Seismic ground motions and slow deformation following the 2004 Parkfield earthquake were recorded by more than 30 seismometers and 13 GPS stations. While this is arguably one of the best-recorded earthquakes, it remains challenging to constrain the physics and properties at depth governing the earthquake from surface observations. Data-driven earthquake models solving inverse problems usually describe the kinematics of rupture. Here, we employ an computationally expensive numerical algorithm to invert observations dynamically and find a physics-based set of param-

eters that simultaneously explain the earthquake and its afterslip, slow deformation following an earthquake. We find two separate phases of the earthquake that cause a similar amount of permanent displacement, but the rapid rupture of the first phase radiates much more potentially damaging seismic waves. The permanent displacement caused by the afterslip of the 2004 Parkfield earthquake exceeded its coseismic displacement. The local frictional properties that arrest the earthquake imprint on the subsequent afterslip evolution. Our approach illustrates that physics-based models utilizing modern computing techniques can reveal new insights and unprecedented detail even of well-studied events.

1 Introduction

The Parkfield section marks the transition between a locked part of the main strand of the San Andreas Fault (SAF) system and a creeping section to the northwest, with slip rates of 20–30 mm/yr (Titus et al., 2005; Tong et al., 2013; Jolivet et al., 2015). The transition between the creeping and locked sections is approximately at Middle Mountain (Murray & Langbein, 2006). Several earthquakes of $M_w \approx 6$ struck the Parkfield section in 1857, 1881, 1901, 1922, 1934, and 1966, corresponding to an average recurrence time of 22 ± 3 years (Bakun & McEvelly, 1984). The Parkfield earthquake prediction experiment (Bakun & Lindh, 1985) anticipated another $M_w \approx 6$ earthquake in 1988 ± 5 years and motivated dense seismic and geodetic instrumentation in the area. However, the anticipated Parkfield earthquake only happened in 2004 without noticeable short-term precursory signals (Bakun et al., 2005; Bilham, 2005). More than 40 strong-motion instruments and 13 GPS stations (Fig. 1) recorded the 2004 Parkfield earthquake and its afterslip within an epicentral distance of less than 32 km (e.g., Liu et al., 2006; Johnson et al., 2006).

1.1 Kinematic source inversion and back-projection imaging

Kinematic source inversions and back-projection studies of the 2004 Parkfield earthquake reveal a heterogeneous rupture process regarding slip, rupture speed, and rise time. The inferred kinematic models generally agree that the rupture process was complex despite its moderate size, with coseismic slip mainly confined within a depth range of 4–10 km (e.g., Langbein et al., 2006). Most models suggest a primary high slip patch surrounding the hypocenter and a second major slip area, 15–20 km northwest of the hypocen-

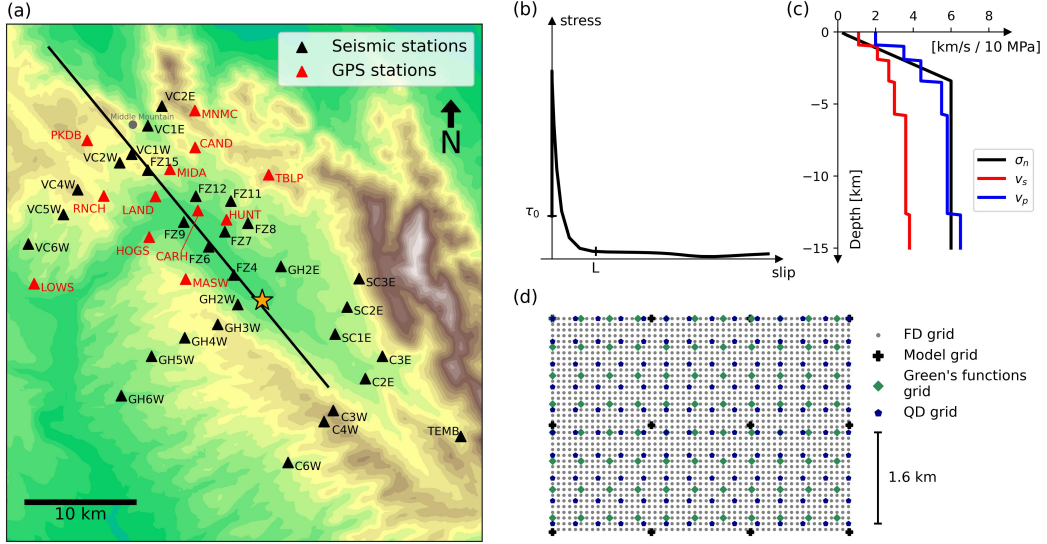


Figure 1. (a) Map view of the model domain with near-fault stations utilized in the dynamic inversion. Black triangles show seismic stations, red triangles are GPS stations, the black line is the fault trace, and the star marks the epicenter location. Topography is shown for regional context but is not accounted for in our forward models. (b) Exemplary stress evolution during coseismic dynamic rupture governed by the fast-velocity-weakening rate-and-state friction law measured in one of our dynamic rupture simulations. τ_0 represents the prestress and L the characteristic slip distance. (c) Assumed depth-dependent normal stress σ_n and averaged seismic velocity profile used in the finite difference solver. We use two different seismic velocity profiles to compute different Green's functions for each side of the fault, respectively, following Custódio et al. (2005). (d) Illustration of the four different grids discretizing the fault plane used in the dynamic source inversion. Dynamic model parameters are defined on the coarsest grid (model grid, black crosses) and bilinearly interpolated on the finest grid used in the finite-difference dynamic rupture solver (FD grid, grey dots) and the grid used in the quasi-dynamic boundary element method (QD grid, blue dots). Slip rates and slip from the FD or QD grids are averaged on the Green's functions grid (green dots) to compute synthetic seismograms and GPS displacements.

80 ter (Johanson et al., 2006; Liu et al., 2006; Custódio et al., 2009; Twardzik et al., 2012),
 81 with purely geodetic models being generally smoother (Kim & Dreger, 2008; Page et al.,
 82 2009). Some studies (Fletcher et al., 2006; Custódio et al., 2009) concluded that there
 83 was rapid rupture onset with rupture velocities close to the S-wave speed (≈ 3.6 km/s
 84 at hypocentral depth) and rise times shorter than 1 s. Propagating to the northwest, rup-
 85 ture speed may have decreased and rise times increased (Fletcher et al., 2006; Ma et al.,
 86 2008; Custódio et al., 2009).

87 Data-driven, kinematic earthquake models use various datasets to illuminate the
 88 space-time evolution of both coseismic rupture and afterslip. Still, they typically can-
 89 not probe dynamically consistent pre-, co-, and post-seismic mechanical conditions of fault-
 90 ing. Dynamic rupture forward modeling, on the other hand, is typically limited to the
 91 coseismic timescale and compares simulation results selectively to observational data or
 92 kinematic models (e.g., Ulrich et al., 2019; Tinti et al., 2021; Taufiqurrahman et al., 2023;
 93 Wen et al., 2024).

94 1.2 Results from previous dynamic modeling

95 Several studies investigated the dynamic source process of the 2004 Parkfield earth-
 96 quake. Ma et al. (2008) constructed a dynamic rupture forward model using a linear slip-
 97 weakening friction law with mostly uniform frictional properties and a constant seismic
 98 S parameter (Andrews, 1976) for regions with a positive stress drop. S is the ratio of
 99 the strength excess over the expected stress drop, $S = \frac{\tau_y - \tau_0}{\tau_0 - \tau_d}$, where τ_y is the yield stress
 100 ($\sigma_n \mu_s$), τ_0 is the initial stress, and τ_d is the dynamic frictional stress ($\sigma_n \mu_d$). μ_s and μ_d
 101 are the static and dynamic friction coefficients, respectively. Their spatial distribution
 102 of the initial stress τ_0 is initially informed by a kinematic slip model (Custódio et al., 2005).
 103 They successively modify the initial stresses, τ_0 , and choose the S parameter and the char-
 104 acteristic slip-weakening distance D_c by trial and error to match near-source ground mo-
 105 tions.

106 Twardzik et al. (2014) performed a simple dynamic inversion to constrain the dy-
 107 namic parameters that governed coseismic rupture. They assumed that the slip was con-
 108 fined to two elliptical patches and inverted for the geometry of the patches, the maxi-
 109 mum S parameter within the patches, and the uniform background frictional properties
 110 of the fault plane. Barbot et al. (2012) created a long-term fully dynamic seismic cycle

111 simulation of the Parkfield section, using a Dieterich-Ruina aging rate-and-state friction
 112 law (Ruina, 1983; Dieterich, 1992). They prescribed a heterogeneous spatial distribu-
 113 tion of the difference between the friction parameters a and b , determining velocity-strengthening
 114 (VS) and velocity-weakening (VW) behavior. All other friction parameters were kept con-
 115 stant. Their model reproduced an earthquake sequence of irregular M_w 6.0 mainshocks
 116 with varying propagation directions. Kostka and Gallovič (2016) modified the dynamic
 117 model of Barbot et al. (2012) and showed that a stress perturbation, possibly caused by
 118 the nearby 1983 Coalinga-Nuñez earthquakes, may have delayed the occurrence of the
 119 2004 Parkfield mainshock.

120 **1.3 Afterslip and aftershocks**

121 An extended period of exceptionally large postseismic deformation followed the 2004
 122 Parkfield earthquake. At the surface, the San Andreas fault zone at Parkfield consists
 123 of two main fault branches, the main San Andreas fault (SAF) and the Southwest Frac-
 124 ture Zone (SWFZ), which are likely connected below 6 km depth (Simpson et al., 2006).
 125 During the 2004 Parkfield earthquake, the SWFZ ruptured coseismically. The SAF slipped
 126 postseismically, and afterslip at the surface was detected only hours after the event (Rymer
 127 et al., 2006; Langbein et al., 2006; Lienkaemper et al., 2006; Jiang et al., 2021a). Murray
 128 and Langbein (2006) estimated the moment of the postseismic slip during the first 60
 129 days following the earthquake to be 2×10^{18} Nm, which is larger than the coseismic mo-
 130 ment release of 1.3×10^{18} Nm. Postseismic slip occurred mainly above the coseismic rup-
 131 ture zone and further to the northwest (Langbein et al., 2006; Johanson et al., 2006).
 132 Surface afterslip reached 20–30 cm one year after the earthquake (Lienkaemper et al.,
 133 2006). Barbot et al. (2009) demonstrated that a purely rate-strengthening friction law
 134 applied on a planar fault can explain most of the observed postseismic surface displace-
 135 ments. Jiang et al. (2021a) combined high-rate with daily GPS solutions to study the
 136 early afterslip of the 2004 Parkfield event and found that early afterslip-associated stress
 137 changes appear synchronized with local aftershock rates.

138 Stress changes induced by coseismic slip and/or afterslip have been proposed to drive
 139 aftershock activity (e.g., Churchill et al., 2024). The 2004 Parkfield aftershocks appear
 140 mainly concentrated in two near horizontal streaks bordering the coseismic rupture zone,
 141 one between 4–6 km depth and the other one between 8–10 km depth (Thurber et al.,
 142 2006). Seismicity migrated along-strike and along-dip during the months after the earth-

quake, which has been interpreted as an indication of afterslip acting as the main driver of aftershocks (Peng & Zhao, 2009; Jiang et al., 2021a). However, Cattania et al. (2015) suggest that secondary triggering of aftershocks by earlier aftershocks may have played a more important role, and Churchill et al. (2022)’s global statistical analysis found no correlation between the relative afterslip moment and large aftershock activity.

1.4 Dynamic earthquake source inversion

The benefits of inverting for dynamic parameters to construct physically consistent source models have been recognized long ago (Fukuyama & Mikumo, 1993; Peyrat & Olsen, 2004; Twardzik et al., 2014), and recent advances in computational capabilities enable inverting for multiple spatial-variable dynamic parameters. Gallovič et al. (2019a) established a Bayesian dynamic source inversion framework, constraining the spatially variable linear slip-weakening friction dynamic parameters (fault prestress, strength and characteristic slip-weakening distance) across a finite, planar fault. This method has been applied to the 2016 M_w 6.2 Amatrice (Gallovič et al., 2019b) and 2020 M_w 6.8 Elazığ earthquake (Gallovič et al., 2020), using strong ground motion observations to constrain dynamic rupture parameters and quantify their uncertainties. Premus et al. (2022) extended the method to rate-and-state friction, which enables jointly simulating coseismic slip and afterslip in the same framework. Their dynamic source inversion of the 2014 M_w 6.0 South Napa California earthquake constrained by co- and postseismic strong ground motion and GPS data illuminated how variable prestress and frictional conditions on the fault govern the spatial separation between shallow coseismic and postseismic slip, the progression of afterslip driving deep off-fault aftershocks, and the coseismic slip distribution.

Here, we apply the approach introduced in Premus et al. (2022) to the extensive seismic and geodetic observations of the 2004 Parkfield earthquake. We are especially interested in investigating the interrelation of coseismic slip and the exceptionally large amount of afterslip in a uniform, data-driven modeling framework. We jointly invert this data to establish an ensemble of dynamic models that simultaneously describe the coseismic and three months of postseismic slip evolution. We detail the complex coseismic and postseismic faulting dynamics of a preferred joint model. We find new evidence for the coseismic rupture phase involving distinctly different rupture styles and explore the complex fault slip transition from the coseismic to the postseismic phase. We investi-

175 gate which dynamic parameters govern different coseismic and afterslip rupture styles
176 and analyze trade-offs between the dynamic parameters. Additionally, we observe that
177 different mechanisms for terminating coseismic rupture leave distinct imprints on after-
178 slip evolution. We jointly quantify the average values and variability of coseismic source
179 characteristics, including stress drop, fracture energy, and radiation efficiency, as well as
180 afterslip kinematics such as rise time, propagation speed, and spatial heterogeneity and
181 extent based on physics-based *and* data-driven models.

182 **2 Methods**

183 This section summarizes the forward and inverse modeling methods and seismic
184 and geodetic data sets used in this study. We present the two stages of our forward model
185 and the respective numerical solvers. Then, we detail the data used to constrain the in-
186 version and our model parameterization. Lastly, we present our inversion strategy. We
187 introduce the friction law that facilitates the dynamic description of our problem and
188 our Parallel Tempering Markov chain Monte Carlo Bayesian inversion method in the Sup-
189plementary Information (Texts S1 and S2).

190 **2.1 Joint dynamic rupture and afterslip forward model**

191 The forward model consists of two stages, the coseismic and the postseismic phase,
192 implemented using a 3D fully dynamic and a 3D quasi-dynamic method, respectively (Premus
193 et al., 2022). In the coseismic stage, we model the earthquake dynamic rupture prop-
194 agation with the code FD3D-TSN (Premus et al., 2020) based on an efficient GPU im-
195 plementation of a finite-difference method. The code uses a fourth-order accurate staggered-
196 grid method with a traction-at-split node implementation (Dalguer & Day, 2007) of the
197 frictional fault interface condition.

198 The postseismic phase is modeled with a 3D quasi-dynamic boundary element ap-
199 proach (Gallović, 2008). The method solves the elastodynamic equation but replaces the
200 inertial term with a radiation damping term (Rice, 1993), facilitating complex afterslip
201 effects such as migrating afterslip fronts. We solve the quasi-dynamic problem with a
202 fifth-order Runge-Kutta method with adaptive time stepping. Both stages share the same
203 planar fault geometry and the same distribution of dynamic parameters but will be con-
204 strained by complementary observations. The final coseismic distributions of the shear

Table 1. Minimum and maximum values of the dynamic parameters subject to the inversion. \dot{s}_w and \dot{s}_{init} can only vary in the velocity-strengthening areas of the fault and have constant values of 0.1 m/s and 10^{-12} m/s in the velocity-weakening areas, respectively.

Label	Parameters	Minimum Value	Maximum Value
τ_0	Shear prestress	10^3 Pa	2×10^9 Pa
$b - a$	Difference between the direct effect and the state evolution parameter	-0.03	0.03
f_0	Reference friction coefficient at $\dot{s}_0 = 10^{-6}$	0.2	1.5
L	Characteristic slip distance	0.004 m	1.0 m
\dot{s}_w	Weakening slip rate	0.01 m/s	2.0 m/s
\dot{s}_{init}	Initial slip rate	10^{-13} m/s	1.21×10^{-9} m/s
h_x	Along-strike position of nucleation patch	28.0 km	32.0 km
h_z	Along-dip position of nucleation patch	6.5 km	9.0 km
r_{nuc}	Radius of the nucleation patch	225 m	450 m
σ_{nuc}	Stress increase within the nucleation patch	1%	60%

205 stress, slip rate, and state variable are used as the initial values of the postseismic stage.
 206 Synthetic seismograms and static displacements are calculated via precomputed Green's
 207 functions (Okada, 1985; Cotton & Coutant, 1997).

208 3D dynamic rupture simulations are computationally expensive, and using rate-
 209 and-state friction laws increases this cost compared to linear-slip weakening friction (e.g.,
 210 Heinecke et al., 2014; Uphoff et al., 2017; Krenz et al., 2021). Monte-Carlo-based Bayesian
 211 inversion approaches require many forward models (e.g., Press, 1968). Therefore, our joint
 212 dynamic coseismic and afterslip inversion requires large computational resources. The
 213 coseismic dynamic rupture propagation stage spans the first 21 s of the forward model,
 214 after which slip rates are low enough ($< 10^{-2}$ m/s) to switch to the quasi-dynamic sim-
 215 ulation in the postseismic stage lasting for 90 days. We use a finite-difference grid spac-
 216 ing of 100 m (Fig. 1d), which sufficiently samples the critical length scale of dynamic rup-
 217 ture, the process zone at the rupture tip, with an average of 6.3 points, ensuring accu-
 218 racy (Day et al., 2005). The grid spacing of the quasi-dynamic solver is 400 m.

219 **2.2 Seismic and geodetic data**

220 We include seismic and geodetic measurements, both on coseismic and postseismic
 221 time scales, as inversion data. To constrain the coseismic rupture dynamics, we use strong-
 222 motion observations at 30 near-fault stations (Fig. 1a). We excluded several near-fault
 223 stations due to missing origin times, strong fault zone effects apparent even at low fre-
 224 quencies, or pronounced site amplifications (Liu et al., 2006). We include only horizon-
 225 tal components due to the worse signal-to-noise ratio of vertical components and because
 226 we do not allow for dip-slip (see Sec. 2.3). De-emphasizing vertical components is a com-
 227 mon assumption for strong-motion inversions of the 2004 Parkfield strike-slip earthquake,
 228 e.g., Liu et al. (2006) down-weighted the vertical components by a factor of 10. The strong-
 229 motion data is integrated to velocities and filtered by a fourth-order causal Butterworth
 230 filter between 0.16 Hz and 0.5 Hz. We choose a low-frequency limit of 0.16 Hz to ensure
 231 a flat frequency response of all instruments (Custódio et al., 2005). The chosen upper
 232 limit of 0.5 Hz mitigates the impact of the 3D velocity structure, in particular, of the
 233 low-velocity fault zone, which may affect all near-fault stations (Li et al., 1990; Lewis
 234 & Ben-Zion, 2010). We use 25 s long seismic waveforms during the convergence phase
 235 (see Sec. 2.4). In the subsequent sampling phase, we limited the coseismic waveforms
 236 to 15 s long waveforms. The chosen relatively short time windows of 25 s or 15 s reduce
 237 contamination from seismic reverberations due to the 3D subsurface structure. We as-
 238 sume a universal data uncertainty of $\sigma = 0.05$ m/s when computing the posterior prob-
 239 ability density function (PDF) of the data (Eq. 7 in Text S2). The assumed data un-
 240 certainty corresponds to approximately half of the maximum data amplitude, in agree-
 241 ment with estimates derived from numerical experiments involving randomly varied ve-
 242 locity models (Hallo & Gallovič, 2016).

243 We use the preprocessed horizontal GPS data by Jiang et al. (2021a) that span both
 244 coseismic and postseismic periods. Namely, we include the coseismic displacements at
 245 12 GPS stations (Fig. 1a) and postseismic displacements at 11 GPS stations during the
 246 90-day postseismic period. We compare the postseismic observations with our synthet-
 247 ics at 35 logarithmically-spaced points in time to increase the weight and resolution of
 248 the early afterslip phase. We excluded the postseismic data from the GPS station CARH
 249 as it is located between the main trace of the SAF and the secondary SWFZ branch south-
 250 west of the SAF. Afterslip migrating from the SWFZ to the SAF likely led to the po-
 251 larity change of the postseismic deformation measured at CARH (Murray & Langbein,

252 2006; Jiang et al., 2021a), an effect which our single fault model cannot capture. We com-
 253 pletely exclude the GPS station POMM from our analysis since it is located directly above
 254 the SWFZ and is likely strongly affected by small-scale complexities in fault geometry
 255 that we cannot capture in our planar fault model (Murray & Langbein, 2006; Custódio
 256 et al., 2009). We assign an individual uncertainty value to each GPS station calculated
 257 from the mean of the data uncertainty as given by Jiang et al. (2021a) during the included
 258 90-day period.

259 **2.3 Model setup**

260 Our dynamic rupture and afterslip forward model incorporates a single planar fault
 261 with a strike of 320.5° and dip of 87.2° based on the fault geometry of the SWFZ of Jiang
 262 et al. (2021a). The Green’s functions account for the fault dip, but the dynamic rupture
 263 and quasi-dynamic models assume a vertical fault plane similar to (Galovič et al., 2019a,
 264 2019b; Premus et al., 2022). We place the hypocenter in the initial dynamic rupture model
 265 at 35.8154°N , 120.3667°W , and 7.5 km depth based on a matched filter relocated earth-
 266 quake catalog (Neves et al., 2022). We use two different 1D velocity profiles (Custódio
 267 et al., 2005) to calculate Green’s functions accounting for different materials on each side
 268 of the fault (Table S1). The coseismic dynamic rupture model assumes an average of both
 269 1D layered velocity profiles, while the postseismic model assumes a homogenous medium,
 270 with $v_s = 3600$ m/s, $v_p = 5800$ m/s, and $\rho = 2700$ kg/m³. The coseismically used
 271 Green’s functions account for anelastic attenuation. We assume variable Q values based
 272 on the empirical relationship v_s : $Q_s = 0.1 v_s$ (in m/s) and $Q_p = 1.5 Q_s$ (Olsen et al.,
 273 2003).

274 Table 1 summarizes the six dynamic parameters ($\tau_0, b-a, f_0, L, \dot{s}_w, \dot{s}_{init}$) and four
 275 coseismic rupture nucleation parameters ($h_x, h_z, r_{nuc}, \sigma_{nuc}$) subject to Bayesian inver-
 276 sion. We fix the weakened friction coefficient f_w to a constant value of $f_w=0.3$ follow-
 277 ing Ma et al. (2008) and vary only the reference friction coefficient f_0 , and, thereby, the
 278 “reference friction drop”, $f_0 - f_w$. Similarly, we fix the direct effect parameter a to a
 279 constant value of $a = 0.015$ and allow the state evolution parameter b to vary, altering
 280 the difference $b-a$. We assume pure strike-slip faulting without dip-slip. Thus, the pre-
 281 stress τ_0 and the initial slip rate \dot{s}_{init} are scalars. The dynamic parameters (prestress
 282 and friction parameters) are defined on the model grid with 24 points along-strike and
 283 9 points along-dip (Fig. 1d). In between the grid points, the dynamic parameters are

284 bilinearly interpolated on the denser FD (finite-difference) and QD (quasi-dynamic) grids.
 285 The such defined number of potentially free dynamic inversion parameters is 1300. How-
 286 ever, the weakening slip rate \dot{s}_w and \dot{s}_{init} can only vary in the velocity-strengthening ar-
 287 eas of the fault and have constant values of 0.1 m/s and 10^{-12} m/s in the velocity-weakening
 288 areas, respectively. The constant \dot{s}_w and \dot{s}_{init} in the velocity-weakening regions simu-
 289 late locked asperities. Therefore, the number of effectively free parameters is approxi-
 290 mately 1100 and can dynamically change throughout the inversion.

291 We use a temporary (for 1 s) overstressed nucleation patch around the hypocen-
 292 ter to initiate dynamic rupture. We invert for the radius of this nucleation patch and
 293 the associated shear stress increase. The along-strike and along-dip location of the cen-
 294 ter of the nucleation patch, the hypocenter, is also subject to the inversion (see Table
 295 1).

296 The effective normal stress linearly increases until a depth of 3.5 km (Fig. 1c) and
 297 then remains constant at 60 MPa at deeper depths (Rice, 1992; Suppe, 2014; Madden
 298 et al., 2022), reflecting the transition from a hydrostatic to a lithostatic pore fluid pres-
 299 sure gradient. Our profile is similar to the normal stress profile in a previous 2004 Park-
 300 field dynamic rupture forward model (Ma et al., 2008).

301 **2.4 Inversion strategy**

302 Dynamic source inversion is challenging due to the nonlinear, ill-posed nature of
 303 the very high-dimensional problem and the complicated non-convex shape of the mis-
 304 fit function. We aim to increase the inversion’s performance by choosing an initial model
 305 (IM) with a high probability density (close to the optimal model). We split the dynamic
 306 inversion workflow into a convergence phase and a sampling phase. The latter generates
 307 the ensemble for uncertainty quantification. During the convergence phase, we manu-
 308 ally modify model parameters, adjust weights and datasets, and restart the Markov chains
 309 to achieve faster convergence. Thus, only the sampling phase represents an undisturbed
 310 MCMC inversion. The maximum likelihood model of the convergence phase serves as
 311 the starting model of the sampling phase. Only a few Markov chain links separate this
 312 starting model from our preferred model (Sec. 3.2). A diagram illustrating the dynamic
 313 source inversion approach is provided in the Supporting Information (Fig. S1).

314 A randomly chosen IM may not nucleate self-sustained rupture or produce a much
 315 larger moment magnitude than the target earthquake. Therefore, we construct an ini-
 316 tial dynamic rupture model based on the stress drop and final slip distribution of “Model
 317 B” of Ma et al. (2008), who use linear slip-weakening friction to model the coseismic rup-
 318 ture of the 2004 Parkfield earthquake. We choose the prestress τ_0 distribution of our
 319 IM to resemble the final slip distribution of Ma et al. (2008). Then, we adapt our ref-
 320 erence friction f_0 and the characteristic slip distance L to approximately reproduce their
 321 rupture velocity distribution using a few trial-and-error simulations. In addition, we ran-
 322 domly perturb the characteristic slip distance L and the prestress τ_0 by up to $\pm 10\%$ to
 323 include small-scale heterogeneity and rupture complexity (see Fig. S2). Ma et al. (2008)
 324 prefer their Model B over their Model A because Model B generates surface displace-
 325 ments more consistent with GPS observations and its slip distribution is more consis-
 326 tent with aftershock locations. For these same reasons, we select their Model B to con-
 327 struct our IM.

328 Despite the random perturbations, the rupture of the IM is very homogeneous (Fig.
 329 S3). The IM’s fit to the data is moderate (see Figs. S4 and S5). It yields a seismic vari-
 330 ance reduction of 0.04 and a coseismic GPS variance reduction of 0.87 ($VR = 1 - \frac{\sum_{i=1}^N \|\mathbf{s}_i(\mathbf{m}) - \mathbf{d}_i\|^2}{\sum_{i=1}^N \|\mathbf{d}_i\|^2}$,
 331 \mathbf{d}_i are the observed data, $\mathbf{s}_i(\mathbf{m})$ are the synthetics, and N is the total number of stations).

332 The first $\approx 500,000$ models generated during the convergence phase focus on the
 333 coseismic dynamic rupture phase (21 seconds) and 69 seconds of early afterslip. Then,
 334 we modify the best-fit model from this convergence ensemble to capture long-term (90-
 335 day) afterslip observations. We manually increase the initial slip rate and potential stress
 336 drop in certain velocity-strengthening areas to approximately match the afterslip dis-
 337 tribution of Jiang et al. (2021a) and the GPS-only model of Johanson et al. (2006). To
 338 suppress anomalously high afterslip at the free surface, we set the reference friction co-
 339 efficient to 1.2 and the prestress below 1 MPa at the free surface’s model grid points.

340 The convergence phase, including long-term afterslip, additionally visits $\approx 700,000$
 341 models. During the convergence phase, we adjust the weighting of the different data sets
 342 (strong-motion, coseismic GPS, and postseismic GPS) to ensure their respective misfits
 343 remain of the same order of magnitude. Similarly, we successively reduce the step size
 344 of the inversion parameter perturbations to keep the model acceptance rate above 10%
 345 (Table S2). We restart the Markov chains several times after finding a model with a sig-

346 nificantly improved misfit. This model then serves as a new starting model for all oth-
 347 erwise independent MPI ranks of the inversion algorithm (see Text S2).

348 We start the sampling phase after reaching a satisfying data misfit. In this final
 349 phase representing a true MCMC inversion, we let the chains sample the model space
 350 without manual interventions to obtain an ensemble of best-fitting models that can ex-
 351 plain the data similarly well. The final sampling phase of the inversion visits $\approx 800,000$
 352 models. The resulting best-fitting model ensemble contains 10,500 unique models. Dur-
 353 ing the sampling phase, all inversion meta-parameters are kept constant.

354 We run the inversion on a server with 8 Nvidia RTX A5000-GPUs and 32 AMD-
 355 EPYC-7313 CPU cores with a 3 GHz base frequency. We compute the coseismic stage
 356 on the GPUs and the postseismic stage on the CPUs. This hybrid approach allows us
 357 to exploit the hardware architecture efficiently using 24 MPI ranks (3 ranks per GPU).
 358 One simulation of the joint forward model takes, on average, 3 minutes for the coseis-
 359 mic phase and 2 minutes for the postseismic phase, totaling 5 minutes. Therefore, we
 360 can visit, on average, 4.8 joint forward models per minute. Overall, the inversion visited
 361 more than 2 million joint simulations. This sums up to over 300 days of runtime on our
 362 server or $>57,000$ hours on a single GPU.

363 **3 Results**

364 **3.1 Initial dynamic rupture model**

365 Our initial dynamic rupture model (IM), which is extended from the dynamic rup-
 366 ture model by Ma et al. (2008), already reveals interesting dynamic aspects of the 2004
 367 Parkfield rupture. We find that an unusually low potential stress drop ($\tau_0 - \sigma_n f_w$) and
 368 reference friction drop ($f_0 - f_w$) are needed to match the large-scale rupture character-
 369 istics of the 2004 Parkfield earthquake. However, in the rate-and-state framework, both
 370 parameters are only approximations of the actual stress drop and friction drop ($f_{max} -$
 371 f_{min}). The earthquake ruptured over an area larger than 20 km along strike while co-
 372 seismic slip remained mostly below 25 cm, which is small considering its magnitude of
 373 M_w 6.0 (Breneman et al., 2019) and in agreement with previous observational studies
 374 (e.g., Liu et al., 2006; Custódio et al., 2009). The IM requires a low average potential
 375 stress drop to facilitate dynamic rupture across a wide area with a small average slip.
 376 Differences in the dynamic parameters in our IM compared to Ma et al. (2008), who use

377 linear slip-weakening friction, arise from the distinct friction laws. For example, the ad-
 378 ditional weakening at high slip rates in our friction law permits rupture propagation at
 379 lower prestress levels (Thomas et al., 2014), resulting in smaller potential stress drops.
 380 In the IM, we set the potential stress drop to 3.0 MPa within the hypocentral area and
 381 to only 0.6 MPa elsewhere, where we expect coseismic rupture (see Fig. S6). Outside
 382 of the expected rupture area, the potential stress drop gradually decreases to -3.0 MPa.

383 A lower stress drop generally reduces rupture velocity (Andrews, 1976; Gabriel et
 384 al., 2012). However, several studies observed that the average rupture velocity of the 2004
 385 Parkfield earthquake is relatively fast at 2.5–3.5 km/s (e.g., Fletcher et al., 2006; Ma et
 386 al., 2008; Custódio et al., 2009). To achieve a dynamic rupture model that combines a
 387 low stress drop with moderate-to-high rupture velocity, we set the characteristic slip dis-
 388 tance within the coseismic rupture area to a value of $L = 2$ cm and assume a small S
 389 parameter. We compute the S parameter as $S = \frac{f_0\sigma_n - \tau^0}{\tau^0 - f_w\sigma_n}$, which represents only an
 390 approximation because the minimum and maximum friction coefficients are dynamically
 391 determined in rate-and-state friction (Gabriel et al., 2012). Our L is smaller than D_c from
 392 the dynamic rupture model by Ma et al. (2008). An equivalent D_c might potentially be
 393 inferred from our L parameter if a proper scaling relation (Cocco & Bizzarri, 2002) could
 394 be derived for the fast-velocity weakening rate-and-state friction law. Since the weak-
 395 ened friction coefficient ($f_w = 0.3$) and the potential stress drop are already prescribed
 396 in the IM, we choose a small reference friction $f_0 = 0.313$. This leads to a reference fric-
 397 tion drop of only 0.013, which is unusually low compared to common dynamic rupture
 398 simulation parameterizations (e.g., 0.4 in Harris et al., 2018). However, such a small ref-
 399 erence friction value is in line with results obtained from dynamic modeling of afterslip
 400 following the 2004 Parkfield earthquake (Chang et al., 2013).

401 **3.2 Preferred joint dynamic rupture and afterslip model**

402 Next, we present our preferred joint dynamic rupture and afterslip model (PM) in
 403 terms of coseismic and postseismic rupture characteristics, fit to the seismic and geode-
 404 tic observations, and distribution of dynamic parameters. We chose the PM, which is
 405 a joint dynamic rupture and 90-day afterslip simulation, to maximize the sum of the seis-
 406 mic and combined (coseismic + postseismic) GPS data variance reductions (VR). The
 407 PM model selected by this criterion achieves a better seismic fit compared to the max-
 408 imum likelihood model of the inversion.

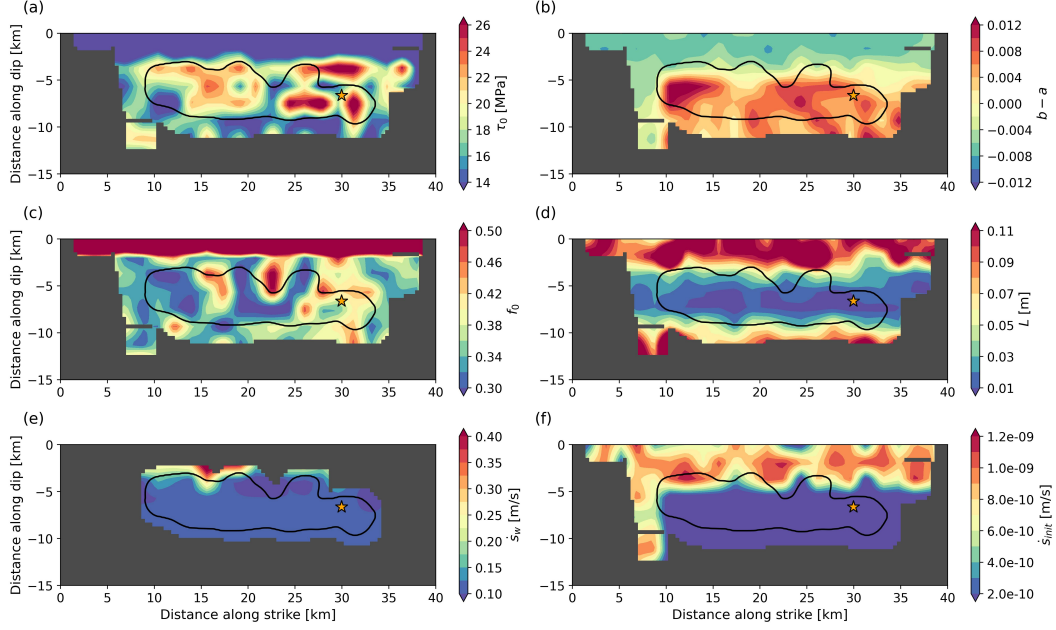


Figure 2. Dynamic parameters of the preferred joint dynamic rupture and afterslip model (PM) resulting from the dynamic source inversion. The parameters are bilinearly interpolated from the model grid (Fig. 1d) onto the grid of the quasi-dynamic solver, which has a 400 m spacing. We consider parameters to be unconstrained in all areas of the fault where the overall fault slip (coseismic + postseismic) does not exceed 10 cm within a radius of 1.2 km. For the weakening slip rate \dot{s}_w , we only consider coseismic slip, as locally larger \dot{s}_w values do not directly affect the afterslip evolution because postseismic slip rates are generally smaller than \dot{s}_w . We do not show dynamic parameters on these unconstrained fault grid points. The black line indicates the extent of the coseismic rupture, and the star marks the hypocenter of the mainshock. (a) Prestress τ_0 . (b) Difference between the state evolution and the direct effect parameter, $b - a$. (c) Reference friction f_0 . (d) Characteristic slip distance L . (e) Weakening slip rate \dot{s}_w . (f) Initial slip rate \dot{s}_{init} , 10^{-9} m/s \approx 31.56 mm/yr.

409 **3.2.1 Dynamic parameters of the preferred joint dynamic rupture and**
 410 **afterslip model**

411 Fig. 2 shows the six dynamic parameters of our PM, which are subject to the in-
 412 version. We do not show parameters on those parts of the faults that we consider un-
 413 constrained by the inversion due to the fact that the sum of the co- and postseismic slip
 414 amplitudes remains too small. We note that dynamic parameters below the coseismic

415 rupture extent are less well constrained due to the limited afterslip and low GPS sen-
 416 sitivity.

417 *3.2.1.1 Prestress, velocity-weakening and velocity-strengthening friction*

418 The spatial average of the prestress within the coseismic rupture area is 18.6 MPa with
 419 a standard deviation of 3.4 MPa. We define the coseismic rupture area as the region where
 420 coseismic slip exceeds 0.01 m, and the fault slip area as the region where the overall slip
 421 (coseismic + postseismic) exceeds 0.1 m within a radius of 1.2 km (visible area in Fig.
 422 2). The fault slip area also includes well-constrained strength barriers. When consider-
 423 ing the fault slip area, the spatial average prestress reduces to 14.9 MPa, and the stan-
 424 dard deviation increases to 6.6 MPa.

425 Within the coseismic rupture area, $b-a$ remains dominantly positive, which is as-
 426 sociated with VW behavior. The spatial average value is 0.0037, and the standard de-
 427 viation is 0.0048. The standard deviation being larger than its average is associated with
 428 the dynamic rupture penetrating the shallowest portion of the fault where $b-a$ is neg-
 429 ative. For the fault slip area, including regions hosting afterslip, the spatial average of
 430 $b-a$ drops to 0.000 with a standard deviation of 0.0059. The respective $b-a$ averages
 431 in the VS and VW regions are comparable to the non-constant values of Barbot et al.
 432 (2012)'s dynamic seismic cycling model, which can be approximated by $b-a = 0.004$
 433 within the coseismic rupture area and $b-a = -0.004$ within the VS regions. The range
 434 of $b-a$ within the shallow VS region agrees with the values obtained from a dynamic
 435 afterslip inversion (Chang et al., 2013).

436 *3.2.1.2 Reference friction and characteristic slip distance*

437 The spatial average reference friction within the coseismic rupture area is 0.358, and
 438 its standard deviation is 0.049. The average coseismic reference friction clearly increases
 439 compared to the IM (0.313) but is still small. The average reference friction increases
 440 considerably to 0.464 when including the afterslip regions. However, this value is strongly
 441 affected by the high reference friction coefficients at the free surface.

442 The average characteristic slip distance L within the coseismic rupture area is 0.030 m
 443 with a standard deviation of 0.024 m, corresponding to a coefficient of variation (CV;
 444 the ratio of standard deviation to average value) of $CV = 0.80$. The average and the stan-
 445 dard deviation increase to values of 0.057 m and 0.045 m, respectively, when including

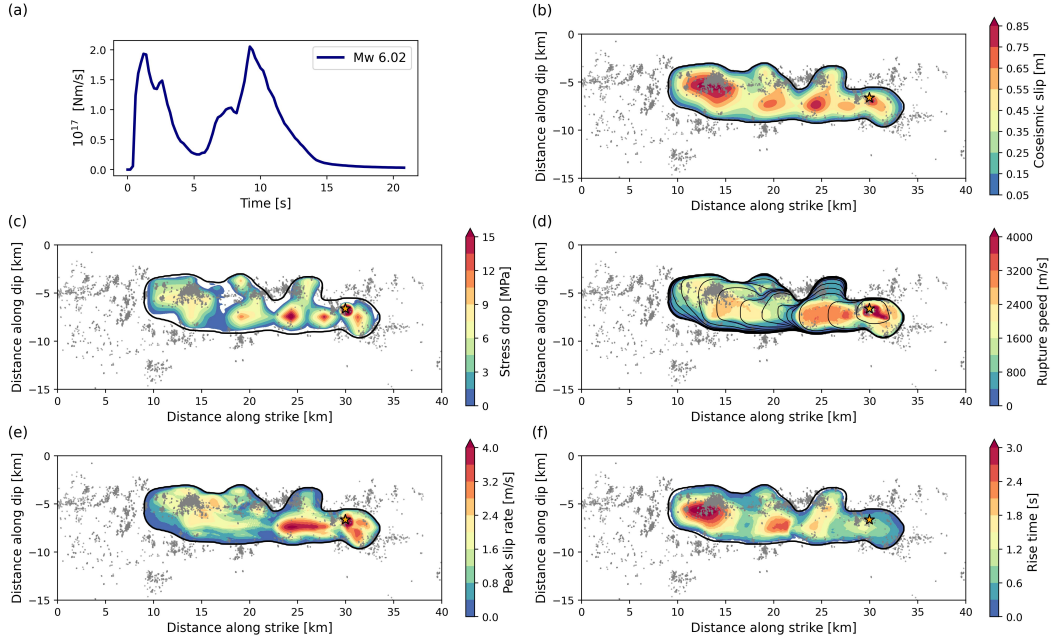


Figure 3. Coseismic dynamic rupture parameters of the PM. Grey dots show 90-day aftershock locations (Neves et al., 2022) projected on the planar fault plane, the black contour indicates the coseismic rupture extent, and the star marks the hypocenter. (a) Moment release rate and moment magnitude. (b) Coseismic slip. (c) Stress drop. (d) Local rupture speed and rupture front contours every 1 s. (e) Peak slip rate. (f) Rise time.

446 the afterslip regions. L noticeably increases above and beneath the top and bottom rup-
 447 ture edges, respectively.

448 3.2.1.3 Weakening and initial slip rates

449 The weakening slip rate \dot{s}_w and the initial slip rate \dot{s}_{init} are allowed to vary only within
 450 VS regions (Sec. 2.3). The \dot{s}_{init} distribution shows that the shallow afterslip regions mostly
 451 creep at a slip rate of 10^{-9} m/s (31.56 mm/yr), which is close to the plate rate. In the
 452 shallow afterslip regions, \dot{s}_w increases to values larger than 0.2 m/s. These larger \dot{s}_w val-
 453 ues do not directly affect the afterslip evolution because postseismic slip rates are gener-
 454 ally smaller than \dot{s}_w .

455 3.2.2 Coseismic rupture dynamics

456 The spatially variable coseismic dynamic rupture characteristics of the PM are shown
 457 in Fig. 3, together with 90-day aftershock locations (Neves et al., 2022). The PM is more

458 complex than the IM described above. In Movie S1, we provide an animation of the PM's
 459 coseismic slip rate evolution to illustrate this complexity. Coseismic rupture separates
 460 into two distinct phases set apart by strong deceleration and acceleration of the rupture
 461 front. The minimum rupture speed occurs at 5 s rupture time. The PM concentrates slip
 462 within several asperities of varying sizes. The first phase of dynamic rupture propaga-
 463 tion involves several smaller asperities in the vicinity of the hypocenter. The largest as-
 464 perity is located in the northwestern part of the fault and ruptures during the second
 465 phase. In the northwest, rupture arrest is collocated with where the creeping section of
 466 the SAF is inferred to begin. Dynamic rupture is inferred to be pulse-like with high peak
 467 slip rates and low rise times during the first phase and transitions to crack-like with lower
 468 peak slip rates and high rise times within the large northwestern asperity. The transi-
 469 tion from pulse-like to crack-like rupture occurs as the rupture propagates to the north-
 470 west, towards the creeping section of the SAF. We detail our definition of pulse- and crack-
 471 like rupture styles based on the ratio of rise time to rupture duration in the Supplemen-
 472 tary Information (Text S3) (Heaton, 1990).

473 *3.2.2.1 Seismic moment release and coseismic slip*

474 Fig. 3a shows the moment rate function that consists of two sharply separated peaks
 475 with a local minimum at 5 s representing the two phases of the rupture. The on-fault
 476 measured moment magnitude of M_w 6.02 corresponds to a seismic moment of $M_0 = 1.33 \times 10^{18}$ Nm,
 477 which slightly exceeds the kinematically inferred values that fall between $1.05\text{--}1.21 \times 10^{18}$ Nm
 478 (Liu et al., 2006; Custódio et al., 2009; Twardzik et al., 2012).

479 The coseismic slip is confined to depths of 4–9 km and extends 3 km in the south-
 480 east direction and 20 km in the northwest direction from the hypocenter. The model's
 481 average coseismic slip is 39 cm, and the highest values reach approximately 80 cm at sev-
 482 eral small asperities close to the hypocenter and within the largest asperity 14–19 km
 483 northwest of the hypocenter. Rupture extent and asperity locations agree well with pre-
 484 vious results from kinematic inversions (Custódio et al., 2009; Twardzik et al., 2012).

485 *3.2.2.2 Stress drop and rupture velocity*

486 The modeled stress drop is spatially highly variable and locally takes negative values.
 487 It reaches a local maximum of 21.5 MPa, and its average is 2.7 MPa, which is similar
 488 to Ma et al. (2008)'s dynamic rupture model but lower than the value of 4.2 MPa inferred
 489 from the lowest misfit model by Twardzik et al. (2014). The highest stress drop values

490 are reached at the asperities close to the hypocenter. Stress drops within the large north-
491 western asperity do not exceed 9 MPa. 7.9% of the coseismic rupture area exhibits a neg-
492 ative stress drop.

493 The fault-local rupture velocity shown in Fig. 3d is highly variable. The average
494 local rupture velocity of the PM is 1.4 km/s. This value is the spatial average of rup-
495 ture speed at each grid point that coseismically slips more than 1 cm and is not equiv-
496 alent to the average rupture velocity of 1.8 km/s measured from the hypocenter to the
497 northern rupture extent. During the first second of dynamic rupture propagation, it reaches
498 supershear velocity (Freund, 1979; Burridge et al., 1979; Das, 2015) of 4.0 km/s during
499 the nucleation of the rupture, which is unexpectedly slow and below the Eshelby speed.
500 While we do not account for a fault damage zone in our forward simulations, this result
501 of the inversion may reflect the presence of a low-velocity fault zone in Parkfield (Bao
502 et al., 2019). We discuss the challenges of accurately modeling earthquake nucleation in
503 dynamic rupture simulations in Sec. 4. The PM ruptures with an average velocity of ap-
504 proximately 3.0 km/s to the northwest for the next two seconds of rupture time. After
505 breaking through an asperity, the rupture dramatically slows down to speeds slower than
506 0.8 km/s between 3 and 5 seconds of simulation time. During the second phase, the rup-
507 ture accelerates again to 2.5 km/s while breaking the large northwestern asperity. Af-
508 ter 11 seconds, the rupture slows down until it arrests at 14 seconds after the nucleation.
509 This slow stopping of the rupture leads to a rupture duration exceeding results from other
510 models (Ma et al., 2008; Custódio et al., 2009; Twardzik et al., 2012).

511 *3.2.2.3 Peak slip rate and rise time*

512 The coseismic peak slip rate distribution correlates with the rupture speed distribu-
513 tion (Schmedes et al., 2010; Gabriel et al., 2013). Slip rates reach their highest values
514 of approximately 4.0 m/s around the hypocenter but do not exceed 2.8 m/s within the
515 large northwestern asperity. The spatial average peak slip rate is 1.3 m/s.

516 Coseismic rise time and peak slip rate are anti-correlated and express distinctly dif-
517 ferent rupture styles within each rupture phase. We define the coseismic rise time as the
518 duration over which the slip rate exceeds 0.1 m/s. The rise time around the hypocen-
519 ter is mostly below 1 s in accordance with results from kinematic studies (Liu et al., 2006;
520 Custódio et al., 2009). Rise time is much larger in the northwestern asperity, where it
521 exceeds 3 s.

522 *3.2.3 Seismic and geodetic verification of coseismic rupture dynamics*

523 Fig. 4 shows observed and synthetic seismic waveforms of the PM at the 30 near-
 524 field strong-motion stations used to constrain the inversion (Sec. 2.2). We show the max-
 525 imum variance reduction at each station after cross-correlation. However, during the in-
 526 version, misfits are calculated without time shifts. The overall variance reduction, cal-
 527 culated from each available seismic data point, is 0.42. We generally fit the onset of the
 528 observed seismic waveforms well. The individual stations' variance reductions vary greatly.
 529 Station FZ7 exhibits the best individual variance reduction of 0.64. Station FZ11, lo-
 530 cated nearby, has the worst fit with a strongly negative variance reduction. In general,
 531 we cannot identify a clear spatial pattern in the seismic variance reduction (see Fig. S7),
 532 except that the three stations closest to the hypocenter, where the modeled dynamic rup-
 533 ture is initiating due to overstress, have a less-than-average variance reduction between
 534 -0.09 and 0.18. This suggests that local effects may dominantly cause the misfits away
 535 from the hypocenter, e.g., site effects or the fault damage zone with highly variable char-
 536 acteristics along-strike (Lewis & Ben-Zion, 2010). We note that even kinematic source
 537 inversions using the same frequency bandwidth struggle to achieve a high seismic vari-
 538 ance reduction (e.g., Kim & Dreger, 2008).

539 Fig. 5a shows the observed and synthetic coseismic static horizontal GPS displace-
 540 ments at 12 GPS stations. Synthetic and observed coseismic displacements are compared
 541 at 90 s after the rupture onset following Jiang et al. (2021a). The overall coseismic static
 542 displacement variance reduction, calculated from each available coseismic displacement
 543 data point, is 0.95, which is better than the achieved fit of a kinematic source model con-
 544 strained by equally weighted seismic strong-motion and GPS data (see Fig. 6b in Kim
 545 & Dreger, 2008). The modeled and observed amplitudes and directions fit nearly per-
 546 fectly at most stations. Our model overpredicts the coseismic displacement at station
 547 LOWS, which is located at approximately twice the distance to the fault trace than the
 548 second farthest station.

549 *3.2.4 Geodetic verification of postseismic faulting dynamics*

550 Fig. 5b shows the normalized time evolution of the observed and modeled post-
 551 seismic horizontal displacements at 11 GPS stations that constrain the 90 days of mod-
 552 eled afterslip. At all 11 GPS stations, largely steadily increasing postseismic displace-

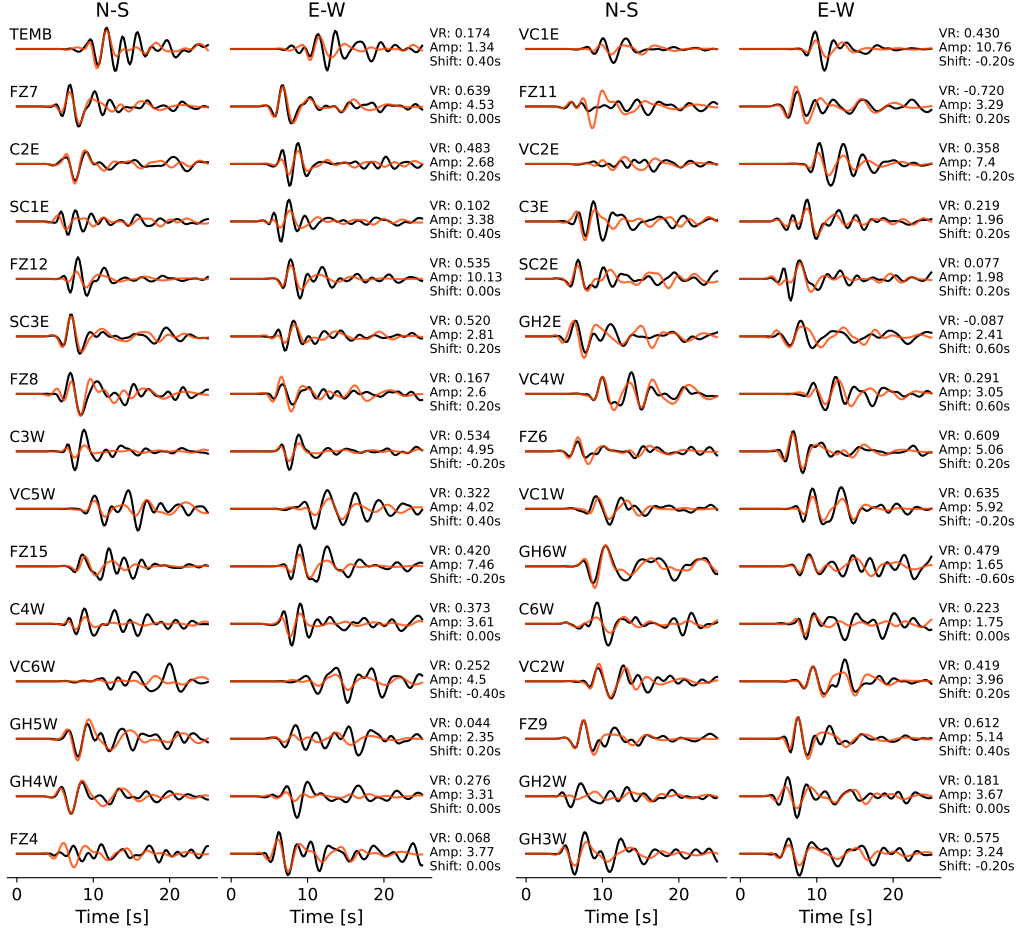


Figure 4. Observed (black) and synthetic (orange) seismic velocity waveforms from the PM, bandpass filtered between 0.16–0.5 Hz at the 30 stations used to constrain the inversion. Each waveform (synthetic and observed) is normalized by the respective station’s maximum amplitude (Amp, in cm/s, either synthetic or observed maximum). In this Figure, the observed waveforms at each station are cross-correlated and time-shifted relative to the synthetics to maximize the variance reduction (VR) and to account for unmodeled effects of topography and the 3D velocity structure.

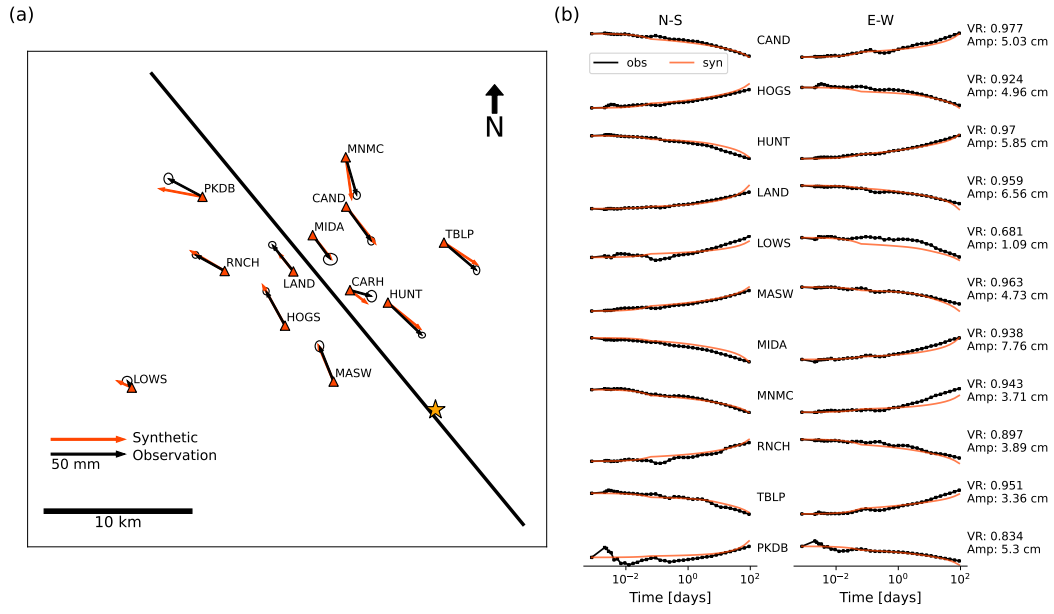


Figure 5. (a) Coseismic horizontal static displacements at 12 GPS stations. Black and orange arrows show observed (Jiang et al., 2021a) and synthetic displacements from the PM, respectively. Black ellipses depict uncertainties of the observations. The black line indicates the model's fault trace and the star marks the epicenter. Both synthetic and observed coseismic displacements are given at 90 s after the rupture onset. (b) Postseismic evolution of the normalized displacements at 11 GPS stations (excluding station CARH) during the first 90 days following the earthquake. Black curves show observations (Jiang et al., 2021a), and orange curves show the synthetics of the PM. The time scale is logarithmic. For each station, we annotate its variance reduction inferred after removing the coseismic displacement and its maximum amplitude.

553 ments reach between 1–8 cm on each horizontal component after 90 days. All compo-
554 nents show similar logarithmic decay rates.

555 The PM of our joint dynamic rupture and afterslip inversion captures the first 90
556 days of observed postseismic GPS deformation well. It achieves an overall variance re-
557 duction of 0.94 calculated from each available postseismic data point, which is remark-
558 able for a dynamically consistent joint dynamic rupture and afterslip model. Similarly
559 to the coseismic displacement misfits, station LOWS has the lowest variance reduction
560 of 0.69. However, its contribution to the overall variance reduction is small due to the
561 small absolute displacement amplitudes at this large distance to the fault. In particu-
562 lar, station PKDB shows spurious oscillations during the first minutes and hours after
563 the earthquake, which probably reflects observational artifacts from an anomalous pe-
564 riod of the entire network (Jiang et al., 2021a). We use a logarithmic time scale to ac-
565 curately sample the early postseismic phase when computing the misfits during the in-
566 version. This leads to a lower implicit weighting of the model’s last weeks. For exam-
567 ple, we observe a late acceleration of postseismic slip evolution at stations LAND, MASW,
568 and PKDB 50 days after the earthquake in our model but not in observations, which likely
569 reflects this weaker penalty. The GPS stations used in our inversion are expected to re-
570 solve shallow slip above the coseismic rupture area accurately. However, their resolution
571 is low at depths larger than 7 km and areas located outside of the lateral extent of the
572 coseismic rupture zone (Page et al., 2009; Barbot et al., 2009).

573 Fig. 6a shows the postseismic slip distribution which our PM accumulates during
574 the modeled 90 days of afterslip. The inferred afterslip is mainly confined between the
575 free surface and the coseismic rupture area at 0–5 km depth. Postseismic slip reaches
576 maximum values of 50–60 cm within several slip patches, which is comparable to the max-
577 imum coseismic slip. Our model’s surface offsets reach 11–17 cm after 60 days, which
578 agrees well with surface offsets ranging from 12–20 cm measured on alignment arrays (Lienkaemper
579 et al., 2006). Considerable parts of the fault that slipped coseismically continue to host
580 afterslip. Dynamic rupture entering VS regions that host afterslip is a well-resolved and
581 persistent feature of our model ensemble. Afterslip can reach up to 35 cm within areas
582 that slipped coseismically, which is almost half of the maximal inferred coseismic slip.
583 Overall, the postseismic slip evolution reflects a smooth transition from the co- to the
584 postseismic phase supported by employing the same friction law.

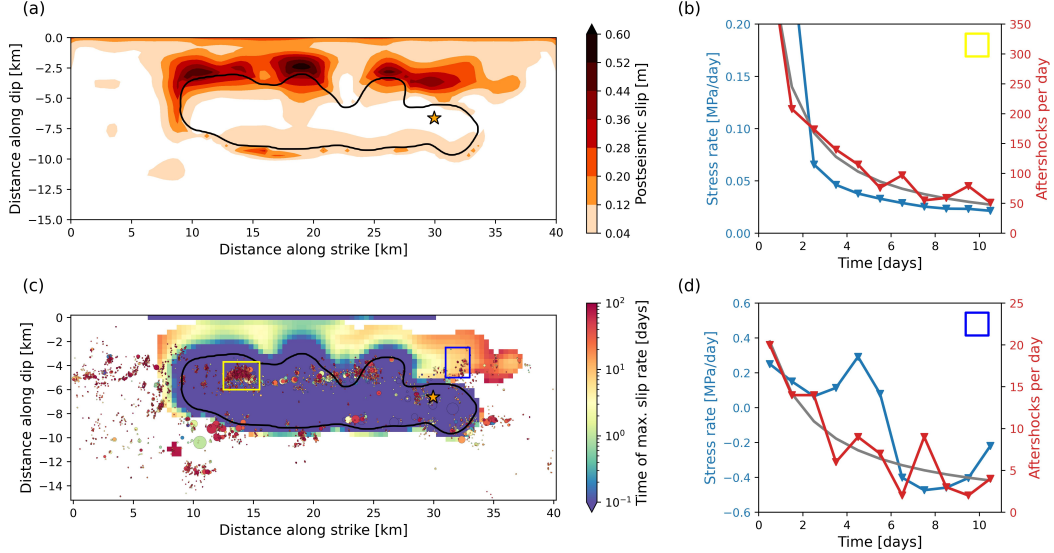


Figure 6. (a) 90-day postseismic slip of the PM. The black contour shows the extent of the coseismic rupture, and the star marks the hypocenter. (b) Aftershock rates (red) compared to average stress rates (blue) of our PM within the yellow aftershock clusters marked in (c). The grey curve shows Omori's law ($n(t) = \frac{k}{c+t}$) fitted to the aftershock rates with $c = 0.68$ days and $k = 534.4$, where n represents the daily frequency of aftershocks depending on the time t since the mainshock. We selected the y-scales to emphasize the similar relative decay rates after 2 days. The apparent delay in the stress rate with respect to the aftershock rate between 1.5 and 2.5 days is just an artifact of this scaling choice. (c) Time evolution of the postseismic rupture front defined as the time of the maximum postseismic slip rate of each point where the maximum slip rate is higher than 10^{-8} m/s. The plate rate is approximately 10^{-9} m/s (Lisowski et al., 1991). Aftershock locations (Neves et al., 2022) are annotated and colored by the same logarithmic color scale, and their size is proportional to their seismic moment. The yellow and dark blue rectangles outline two aftershock clusters for which we compare aftershock rates and mean stress rates in (b) and (d). (d) Same as (b) for the aftershock cluster located within the dark blue rectangle marked in (c). Omori's law is fitted using $c = 1.78$ days and $k = 46.51$.

585 A striking feature of the model’s afterslip distribution is a pronounced gap in the
 586 afterslip located directly above the coseismic rupture area approximately 7–8 km north-
 587 west of the hypocenter. Such a local lack of slip is also present in the postseismic slip
 588 model of Murray and Langbein (2006). In our PM, the same area that features a gap
 589 in the afterslip acts as a strong barrier to the coseismic dynamic rupture propagation
 590 and causes strong rupture deceleration starting at 3 seconds after the nucleation (Fig
 591 3b). This may reflect geologic heterogeneity along this transitional segment of the San
 592 Andreas Fault. As mentioned before, the minimum coseismic rupture speed is reached
 593 at 5 s propagation time.

594 *3.2.5 Kinematics of afterslip and aftershocks*

595 Fig. 6c shows the temporal evolution of the maximum postseismic slip rate and 90-
 596 day aftershock activity following the earthquake (Neves et al., 2022). During the first
 597 three hours after the earthquake, an afterslip front develops at the shallow perimeter of
 598 the coseismic rupture and migrates up to 2 km above the coseismic slip. Surface after-
 599 slip, possibly aided by locally low confining stress in our forward models, also initiates
 600 during the first two hours after the earthquake (Langbein et al., 2005) but is initially not
 601 connected to the afterslip front migrating away from the coseismic rupture area. The fastest
 602 afterslip front is located 12 km northwest of the hypocenter and reaches the surface ap-
 603 proximately one day after the earthquake. All major afterslip patches reach their max-
 604 imum slip rate during the first 10 days following the mainshock. A small afterslip patch
 605 southeast of the hypocenter spontaneously emerges 10 days after the event and later con-
 606 nects to an afterslip front originating from the coseismic rupture area. The maximum
 607 modeled slip rate within this emerging afterslip patch reaches 10^{-6} m/s. However, the
 608 afterslip inferred at the southeastern part of the fault has a higher uncertainty as the
 609 sensitivity of the GPS network is lower (see Sec. 3.3.1 and Page et al., 2009; Barbot et
 610 al., 2009). Despite the dynamic complexity of afterslip evolution governed by rate-and-
 611 state friction, the overall mean postseismic slip rate steadily decays after 10 seconds (Fig.
 612 S8).

613 Aftershock locations are related to the coseismic slip distribution. At the bottom
 614 and the lateral sides of the coseismic rupture area, aftershocks are mostly located at the
 615 edge or outside of the coseismic rupture area. A band of aftershocks, including the most
 616 active clusters, occurs mostly within the coseismic rupture zone between 4–6 km depth.

617 Below 6 km depth, the coseismic rupture area is widely depleted of aftershocks reflect-
 618 ing coseismic stress release.

619 To analyze the spatiotemporal relationship between afterslip and aftershocks, we
 620 compare afterslip stressing rates and aftershock seismicity evolution with time. Figs. 6b,d
 621 show aftershock rates of two aftershock clusters during the first 10 days after the main-
 622 shock. The aftershock rate of the largest aftershock cluster (yellow rectangle) compares
 623 well to our model’s mean stressing rate within the cluster region. The decay of the af-
 624 tershock rate n with time since the mainshock t follows Omori’s law ($n(t) = \frac{k}{c+t}$, grey
 625 curve in Fig. 6b) with $c = 0.68$ days. The inferred c value in this area falls within the
 626 typical range of 0–1 days and is often associated with incomplete detection of small events
 627 (Utsu et al., 1995; Kagan & Houston, 2005).

628 Aftershocks located within the blue rectangle in Fig. 6c may be driven by an af-
 629 terslip front that arrives 5–6 days after the mainshock. This afterslip front originates 4 km
 630 northwest from the hypocenter and propagates backward in the southeast direction. The
 631 average stressing rate within this region shows considerable complexity due to the pas-
 632 sage of the afterslip front. The average stress rate decreases during the first days after
 633 the mainshock. However, after 3 days, it starts to increase again, peaking at 4.5 days,
 634 which is aligned with the arrival of the afterslip stress front. Then, the stress rate rapidly
 635 decreases and turns negative due to the stress release caused by the passing afterslip. This
 636 may explain the observed considerable aftershock increase 7.5 days after the mainshock,
 637 which coincides with the maximum negative stress rate in our model. It is difficult to
 638 apply Omori’s law to this aftershock cluster. To match the aftershock rate peak at 7.5 days,
 639 an unusually large c value of 1.78 is required. Removing the peak reduces c to 1.54, which
 640 is yet larger than typical values. We note that afterslip in this region remains present
 641 in the mean of our best-fitting model ensemble but with increased uncertainty (see Sec.
 642 3.3.1). The cumulative aftershock moments in the yellow and blue regions correspond
 643 to 4% and less than 0.1% of the PM’s moment released by afterslip in the same regions
 644 and period, respectively. These values are likely too small to considerably affect observed
 645 surface displacements or to support the argument that aftershocks may drive afterslip
 646 (Barbot et al., 2009).

647 Fig. 7a shows the afterslip rise times of the PM, which vary by more than two or-
 648 ders of magnitude. Within the coseismic rupture area, afterslip rise times are short and

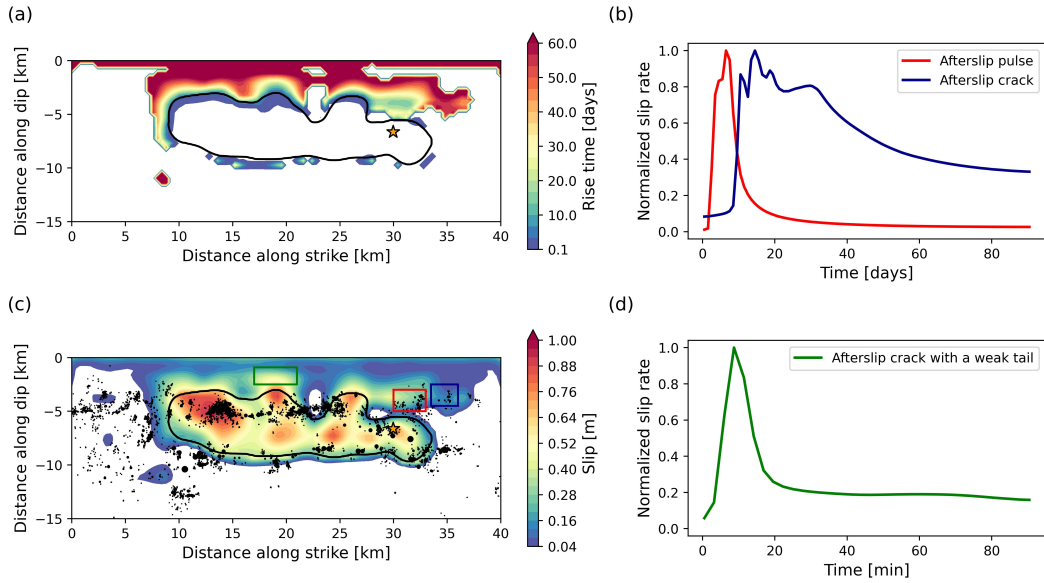


Figure 7. (a) Afterslip rise times defined as the time it takes to reach 80% of the final slip. (b) Normalized average slip rates within the red and blue rectangle marked in (c). (c) Combined coseismic slip and 90 days of postseismic slip of the PM. Colored rectangles indicate regions for which mean slip rates are shown in subplots b and d. The black line indicates the extent of the coseismic rupture, black dots show aftershock locations, and the star marks the hypocenter. (d) Normalized average slip rate within the green rectangle marked in (c). The analyzed regions in (b) and (d) are not located within the coseismic rupture area, which results in the observed slip rate accelerations as the afterslip front reaches these regions.

649 range between a few hours to a few days. Outside the coseismic rupture area, afterslip
 650 rise times rapidly increase to weeks and months. This increase gradually occurs over a
 651 distance of approximately 2 km away from the edge of coseismic rupture.

652 An interesting exception is a localized, approximately 4 km wide region above the
 653 hypocenter, where afterslip rise time remains constant between 15–20 days. Afterslip in
 654 this epicentral region originates from 4 km northwest along-strike from the hypocenter.
 655 There, coseismic rupture penetrates the shallow velocity-strengthening zone and initi-
 656 ates an afterslip front that propagates with constant rise time in the backward direction
 657 of coseismic rupture. This afterslip front propagates at a speed of approximately one kilo-
 658 meter per day, which is comparable to rupture velocities of slow slip events (e.g., Vavra
 659 et al., 2023). This afterslip front may drive aftershock activity (Fig. 6c and Movie S2).

660 The afterslip in our rate-and-state framework takes the form of different rupture
 661 styles resembling coseismic pulse-like and crack-like rupture across the same fault. The
 662 red curve in Fig. 7b shows a pulse-like afterslip slip rate function associated with the af-
 663 terslip region within the red rectangle in Fig. 7c, where the backward propagating af-
 664 terslip front is located. The average slip rate function of the adjacent region marked with
 665 a blue rectangle (blue curve in Fig. 7b) reveals a distinctly different slip rate behavior.
 666 Here, the slip rate function resembles a crack-like style of afterslip, remaining above 35%
 667 of the peak slip rate until the end of the 90-day simulation time. This region represents
 668 a coalescence of two afterslip fronts, the first arriving from the northwest region marked
 669 in red and the second originating from the spontaneously emerging afterslip patch to the
 670 southeast. However, the latter feature is associated with considerable uncertainties (see
 671 Sec. 3.3.1) and falls within the low GPS sensitivity fault region.

672 The green curve associated with the fault segment marked by a green rectangle (Fig.
 673 7c,d) shows the normalized mean slip rate function of the area with the maximum af-
 674 terslip. The time scale of the afterslip in the region marked in green (minutes) differs
 675 from the time scales of the afterslip in the regions marked in red and blue (days). The
 676 associated time scales rapidly increase with distance to the extent of the coseismic rup-
 677 ture. This slip rate function resembles an intermediate afterslip style falling in between
 678 a pulse-like and crack-like characteristic. It is characterized by a sharper peak in the be-
 679 ginning and a weaker tail remaining at approximately 20% of the peak slip rate.

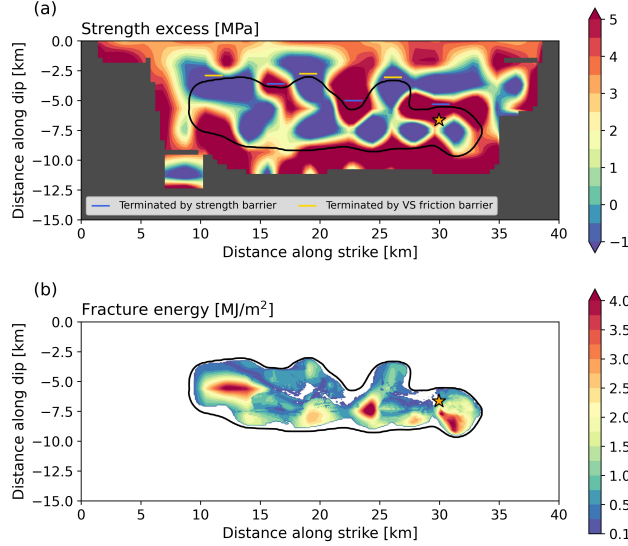


Figure 8. PM’s (a) initial strength excess ($\sigma_n f_0 - \tau_0$), (b) coseismic fracture energy distributions. We only show the strength excess where coseismic and postseismic slip combined exceed 10 cm somewhere within a radius of 1.2 km, which we consider as constrained by the inversion.

3.2.6 Strength excess and fracture energy

Fig. 8 shows the initial strength excess ($\sigma_n f_0 - \tau_0$) and the coseismic fracture energy distribution of our PM. We calculate the strength excess using the reference friction coefficient f_0 to approximate the static fault strength (see Sec. 4.4). However, the maximum friction coefficient reached during rupture is not a fixed, prescribed parameter of our forward model. In our simulations, the reference friction coefficient represents a lower bound of static friction within the velocity-weakening regions (Ulrich et al., 2019). The strength excess distribution implies two fundamentally different coseismic rupture-stopping mechanisms. The strength excess within the coseismic rupture area is generally low, with a spatial average of 1.05 MPa. It contains negative values. Shallow coseismic rupture is partly terminated at local fault strength ‘barriers’, marked with blue lines in Fig. 8a, which are areas with larger strength excess than their surroundings (Pulido & Dalguer, 2009). In distinction, coseismic rupture stops in regions with negative strength excess at three shallow locations (yellow lines in Fig. 8a).

We find that fracture energy is correlated with stress drop distribution (Fig. 3c). We define fracture energy per unit area as:

$$G = \int_0^{x_{\tau_{min}}} [\tau(x) - \tau_{min}] dx, \quad (1)$$

where τ is shear stress, x is slip, τ_{min} is minimum shear stress, and $x_{\tau_{min}}$ is slip at the minimum shear stress. The three regions with the largest fracture energy are located (i) southeast below the hypocenter, (ii) 7 km northwest of the hypocenter, where dynamic rupture decelerates abruptly, and (iii) within the large asperity 15 km northwest of the hypocenter. The spatial average of the fracture energy within the coseismic rupture area is 0.95 MJ/m². Our inference here is similar to the 1.1 MJ/m² inferred for the similarly-sized 2016 M_w 6.2 Amatrice normal faulting event (Gallovič et al., 2019b). A smaller value of 0.044 MJ/m² has been recently inferred from earlier 3D dynamic rupture models of a sequence of small (M_w 1.9) repeating earthquakes on the SAF 25 km northwest to the 2004 Parkfield hypocenter (Lui & Lapusta, 2018; Gabriel et al., 2024), in line with the observed fracture energy scaling with earthquake - or rupture - size (Cocco et al., 2023; Gabriel et al., 2024).

3.3 Model ensemble characteristics and dynamic parameter trade-offs

To assess model uncertainties and trade-offs, we analyze model average quantities and their variability obtained from an ensemble of best-fitting models (Sec. 2.4) containing 10,500 unique model parameterizations. All standard deviations are computed with respect to the mean of the best-fitting model ensemble. The ensemble average distributions of slip, rise time, afterslip, and dynamic parameters are similar to the ones of the PM. The separation into two coseismic rupture phases with different rupture styles and the locations of co- and postseismic slip asperities are stable features of the model ensemble.

3.3.1 Ensemble averages and uncertainties

Fig. 9 shows the best model ensemble's average and standard deviation of the coseismic slip, the rise time, and the afterslip. The mean coseismic slip distribution is very similar to the slip distribution of the PM. Its spatial median coefficient of variation is 17.3%. The standard deviation distribution has its lowest values 8 km northwest of the hypocenter, where the rupture strongly decelerates. This illustrates that this rapid rupture deceleration is a critical phase of the coseismic rupture dynamics. Large standard

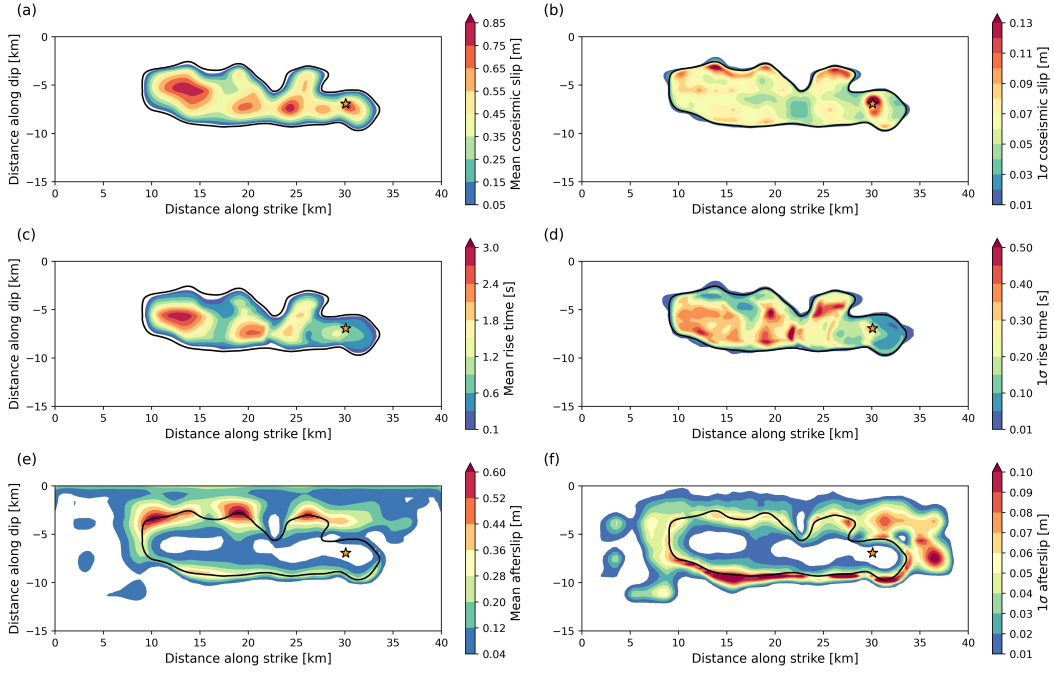


Figure 9. Ensemble average (a) coseismic slip, (c) rise time, (e) postseismic slip, and their respective standard deviations (b,d,f). Averages and standard deviations are computed from the best-fitting model ensemble containing 10,500 unique models.

725 deviation values are mostly concentrated close to the rupture edges. They reach partic-
 726 ularly high values where the rupture terminates due to the transition to the velocity-strengthening
 727 regime, indicating that the abruptness of rupture termination depends on the stopping
 728 mechanism. The locally high standard deviation of the rupture contours at the same lo-
 729 cation (Fig. S9) confirms this observation.

730 The mean rise time distribution shows short rise times around the hypocenter and
 731 an area with increased rise times at the northwestern end of the rupture. The coefficient
 732 of variation of both rise-time features lies in the range of 10–20%, indicating that they
 733 are stable results of the inversion. The rise time standard deviation distribution reaches
 734 its largest value approximately 9 km northwest of the hypocenter, where the rupture ac-
 735 celerates again after nearly terminating.

736 The afterslip variability is greatest at the bottom of the coseismic rupture zone,
 737 reflecting the combined effects of varying rupture extent and the GPS network’s low res-
 738 olution. Another zone of high afterslip variability above and southeast of the hypocen-
 739 ter likely reflects the weak constraints due to the GPS network configuration, with all

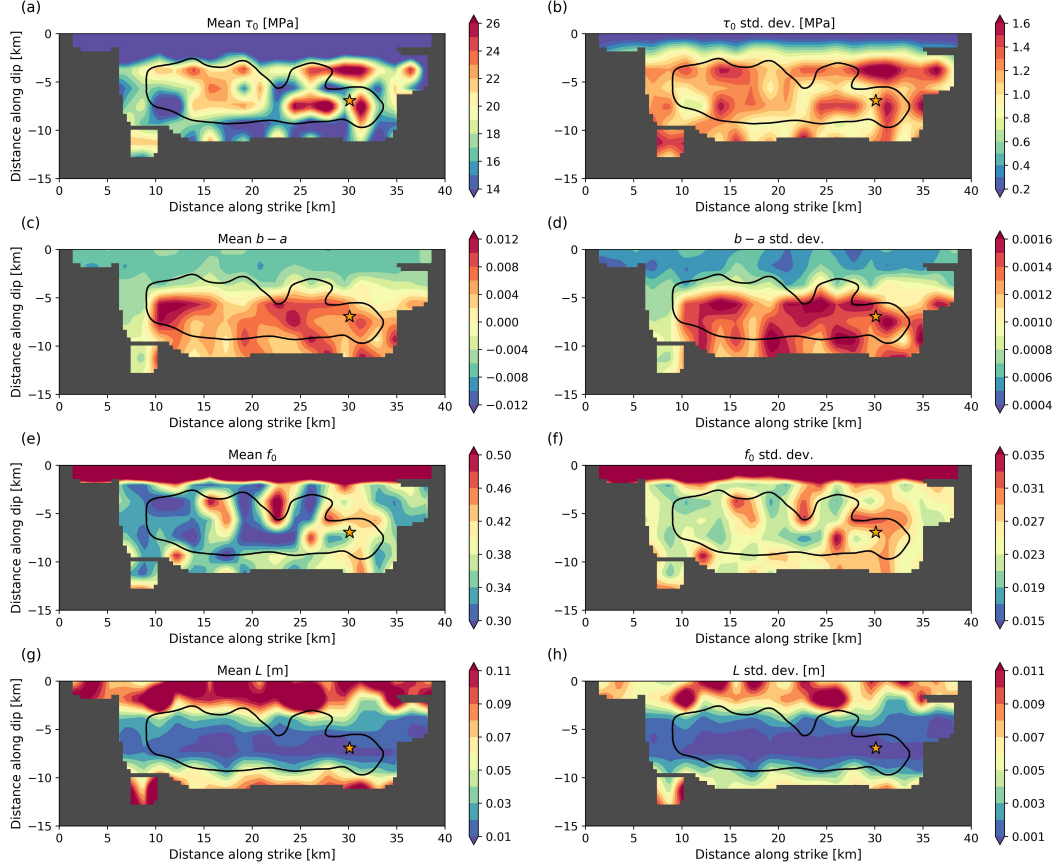


Figure 10. Mean distributions of the best-fitting model ensemble’s (a) prestress τ_0 , (c) $b - a$, (e) reference friction f_0 , (g) characteristic slip distance L , and their respective standard deviations (b,d,f,h). The model ensemble contains 10,500 models. We mask areas where the sum of coseismic and postseismic slip does not exceed 10 cm within an area of a radius of 1.2 km, which we consider unconstrained.

740 stations located northwest of the hypocenter. The variability is generally reduced close
 741 to the free surface, where the sensitivity of the GPS network increases.

742 The dynamic parameters do not vary extensively within the ensemble. Figure 10
 743 shows the ensemble mean and the standard deviation distributions of the prestress τ_0 ,
 744 $b - a$, the reference friction f_0 , and the characteristic slip distance L . The means of all
 745 four dynamic parameters are comparable to the PM (see Fig. 2). The standard devia-
 746 tions are relatively small and highly correlated with the corresponding mean distribu-
 747 tions. Plotting the coefficient of variation of the four dynamic parameters or a strictly
 748 positive equivalent (see Fig. S10) confirms this observation. The coefficients of variation

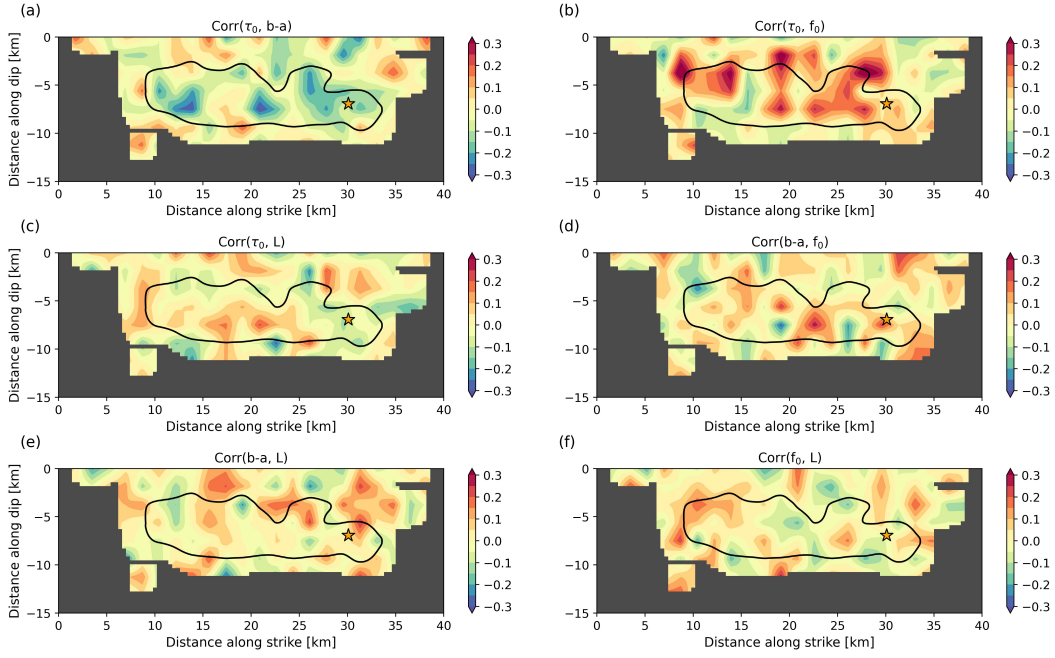


Figure 11. Ensemble correlation coefficients' spatial distribution of dynamic parameter pairs (a) τ_0 and $b - a$, (b) τ_0 and f_0 , (c) τ_0 and L , (d) $b - a$ and f_0 , (e) $b - a$ and L , (f) f_0 and L . The black contour indicates the extent of the coseismic rupture, and the star marks the hypocenter. We mask areas where the sum of coseismic and postseismic slip does not exceed 10 cm within an area of a radius of 1.2 km, which we consider unconstrained.

749 of all four parameters are spatially rather homogeneous, with values ranging mostly be-
 750 tween 4–8%. Within the coseismic rupture area, τ_0 has the smallest and L the largest
 751 relative uncertainties.

752 *3.3.2 Ensemble correlations and source parameters*

753 The prestress is locally (anti-)correlated with $b - a$ and f_0 , while overall correla-
 754 tion values between different dynamic parameters are small. Fig. 11 shows correlation
 755 coefficients of the ensemble's dynamic parameters to analyze trade-offs between them.
 756 Correlation coefficients rarely exceed ± 0.4 . Locally, prestress τ_0 and reference friction
 757 coefficient f_0 share the highest positive correlation. Maximum values up to 0.4 are reached
 758 in areas where coseismic and postseismic slip overlap, likely because prestress variations
 759 can be dynamically balanced by changes in the reference friction coefficient. τ_0 and $b - a$
 760 show an anticorrelation of up to -0.3. High anticorrelation in areas with large rise times

761 may indicate that a careful balance between τ_0 and $b-a$ is important to facilitate sus-
 762 tained crack-like rupture. Slip-weighted average correlation coefficients of the other four
 763 parameter pairs are below 0.02.

764 When considering only afterslip, still f_0 and τ_0 still exhibit the strongest correla-
 765 tions. Zhao and Yue (2023) showed that the afterslip evolution under steady-state as-
 766 sumption depends on the difference $\tau_0 - \sigma_n f_0$. Our results also indicate significant trade-
 767 offs between τ_0 and f_0 when accounting for the weakening phase. The advantage of prob-
 768 abilistic approaches is their ability to accommodate trade-offs and unresolved parame-
 769 ters. Nevertheless, the parameter space of future dynamic inversions might be minimized
 770 by jointly inverting for $\tau_0 - \sigma_n f_0$. Additionally, we find a locally high anticorrelation
 771 between s_{init} and $b - a$ for the afterslip above the hypocenter (Fig. S11).

772 The dynamic source inversion approach facilitates computing fundamental earth-
 773 quake source parameters such as radiated energy and fracture energy while simultane-
 774 ously relying on observed data and the underlying physics. Fig. S12 displays histograms
 775 of various coseismic and postseismic rupture parameters of the best-fitting model ensem-
 776 ble. We find an ensemble average radiated energy of 2.19×10^{13} J and an average co-
 777 seismic fracture energy of 8.30×10^{13} J, which translates to an average radiation effi-
 778 ciency of 21%.

779 4 Discussion

780 4.1 Mixed crack- and pulse-like rupture dynamics governed by local fault 781 heterogeneity

782 It remains debated whether earthquakes predominantly propagate as cracks or as
 783 pulses (Heaton, 1990). For example, Lambert et al. (2021) hypothesize that large megath-
 784 rust events mainly rupture as ‘mild’ cracks whereas crustal strike-slip faults rupture in
 785 the form of self-healing pulses. We infer a clear transition from pulse-like to crack-like
 786 (see Text S3) coseismic rupture of the crustal strike-slip 2004 Parkfield earthquake. This
 787 may indicate that the style of earthquake rupture rather depends on local rheological
 788 and frictional properties than on the regional tectonic setting and that one earthquake
 789 may comprise more than one rupture style (e.g., Gabriel et al., 2012).

790 We analyze the spatial correlation between rise times and dynamic parameters (Fig.
 791 S13) of our preferred model (PM) to understand the underlying factors causing the co-

792 seismic rupture style transition. The overall geometrical simplicity of the Parkfield seg-
 793 ment suggests that the observed rupture behavior is driven mainly by initial stresses and
 794 specific local frictional properties. While rise time does not correlate with the prestress
 795 τ_0 (correlation coefficient $cc = -0.05$), it depends on the interplay between $f_0 - f_w$, $b -$
 796 a , and L . The reference friction drop exhibits the highest (anti-)correlation of -0.59 with
 797 rise time. The largest rise times are reached when the reference friction drop is smaller
 798 than 0.05 . L shows an anticorrelation (-0.39) with rise time and $b - a$ shows a positive
 799 correlation of 0.47 with rise time. These results imply that a velocity-weakening regime,
 800 with small L and small $f_0 - f_w$, promotes crack-like rupture. The observed anticorre-
 801 lation between rise time and reference friction drop is consistent with the dynamics of
 802 self-healing rupture pulses (Brune, 1970; Heaton, 1990). From theory (Perrin et al., 1995;
 803 Zheng & Rice, 1998) and previous numerical studies (e.g., Gabriel et al., 2012), we ex-
 804 pect that for dynamically sufficiently weak faults the selection between cracks and pulses,
 805 and their coexistence, has a non-trivial dependence on initial conditions. However, heal-
 806 ing fronts emerging from coseismic rupture termination also locally reduce rise times,
 807 as seen above the hypocenter and at the northwestern end of coseismic rupture (see Movie
 808 S1). Contrary to our results, Ampuero and Rubin (2008) report an anticorrelation be-
 809 tween $b - a$ and rise time. Velocity-strengthening regions affect these correlations. When
 810 only considering velocity-weakening parts, the correlations between rise time and $b -$
 811 a , $f_0 - f_w$, and L , change to 0.39 , -0.71 , and -0.30 , respectively. We conclude that a com-
 812 plex interplay of fault-local dynamic parameters determines the rupture style.

813 In our PM, both rupture styles produce vastly varying seismic radiation. Fig. S14
 814 shows a waveform comparison with synthetics generated by a 5 s version of our PM, in-
 815 cluding only the initial pulse-like phase. The short model's overall seismic variance re-
 816 duction reaches 95.3% of the full model's variance reduction, but the short model can-
 817 not explain the displacements measured by the GPS stations. The initial pulse-like phase
 818 produces most of the seismic radiation while accounting only for 35.7% of the seismic
 819 moment, in agreement with observations (Allmann & Shearer, 2007).

820 This is consistent with our inferred gradual transition from the coseismic to the post-
 821 seismic phase. Coseismic rupture dynamics initiate as a strongly radiating phase, fol-
 822 lowed by a mildly radiating phase, which only weakly imprints on the seismic data but
 823 produces dynamic perturbations in the GPS data (Jiang et al., 2021a). Finally, aseis-
 824 mic afterslip dominates with rise times increasing with time and distance from the co-

825 seismic rupture area (Fig. 7). These results highlight the importance of complementary
826 data sets to infer kinematic and dynamic source models and have important implications
827 for seismic hazard assessment: Similarly sized earthquakes can cause vastly different ground
828 motions based on the dominantly operating rupture style, and large earthquakes can ex-
829 perience strong local amplifications due to dynamic rupture complexity (Schliwa & Gabriel,
830 2023).

831 4.2 Rupture duration and rupture speed variability

832 We observe locally pronounced variations in rupture speed in the dynamic inver-
833 sion, with rupture durations exceeding those inferred from many kinematic source mod-
834 els (e.g., Custódio et al., 2005, 2009; Liu et al., 2006). The rupture speed changes cause
835 a bimodal moment rate function, which together with the long rupture duration are sta-
836 ble features of the best-fitting model ensemble (Fig. S15). Fletcher et al. (2006) deter-
837 mined the rupture velocity using back-projection, identifying the last well-correlated high-
838 frequency pulse at 4 seconds after nucleation, 9 km from the hypocenter. This timing
839 aligns with the changes in rupture speed and rupture style in our dynamic inversion model
840 (Fig. S16). They did not find high-frequency sources at the northwestern asperity, where
841 we observe a mildly radiating crack-like rupture, which produces only weak seismic ra-
842 diation > 0.16 Hz (cf. Fig. 4 to S14). In contrast, Allmann and Shearer (2007) still found
843 a burst of high-frequency seismic radiation originating at the southern edge of the north-
844 ern high-slip patch approximately 13 km northwest of the hypocenter. Our model en-
845 semble persistently features a strong rupture deceleration and subsequent acceleration
846 between the southeastern and northwestern parts of the rupture. Such abrupt changes
847 in rupture velocity can explain the observed high-frequency radiation (e.g., Madariaga,
848 1977; Shi & Day, 2013; Schliwa & Gabriel, 2023). Jiang et al. (2021a) observed that dy-
849 namic displacements measured with GPS stations, which are sensitive to lower frequen-
850 cies, lasted twice as long (60 seconds) as the shaking recorded with strong motion sen-
851 sors. This may help explain the rupture duration differences between our results and many
852 kinematic models that rely solely on accelerometer recordings with frequencies > 0.16 Hz.
853 Additionally, a study analyzing near-fault strong ground motions reported no evidence
854 of sustained supershear rupture (Shakal et al., 2006), while some kinematic models re-
855 quire (near) supershear rupture speeds that produce minimal slip (Custódio et al., 2005;
856 Liu et al., 2006).

857 Different studies disagree on the potential supershear onset of the 2004 Parkfield
 858 earthquake. Similar to the rupture speed in our PM, Custódio et al. (2009) reported a
 859 supershear rupture onset with velocities above 4 km/s during the first second of their
 860 kinematic source model. However, Ma et al. (2008)’s forward dynamic rupture model
 861 B does not exhibit an initial supershear rupture velocity, while Twardzik et al. (2014)’s
 862 simple 2-ellipse dynamic inversion model nucleates at supershear speed (3.8 km/s), il-
 863 lustrating the non-uniqueness of proposed early rupture phases fitting observations with
 864 different model approaches. Dynamic rupture simulations mostly employ prescribed nu-
 865 cleation procedures, which can introduce additional challenges in accurately modeling
 866 rupture onset. We note that dynamically, supershear rupture may initiate at the onset
 867 of rupture, without requiring propagating a certain distance, if the fault is locally weak
 868 or highly prestressed (e.g., Gabriel et al., 2012). The above mentioned models do not fea-
 869 ture the strong rupture deceleration after 3 seconds. Fletcher et al. (2006) also inferred
 870 a fast rupture onset but without reaching supershear speeds. In their study, the rupture
 871 starts with a velocity of 3.3 km/s and then drops below 1 km/s. The observed drop in
 872 rupture velocity aligns perfectly with the rupture deceleration in our PM (Fig. S16).

873 The rupture speed change in our model ensemble is caused by a strong fault strength
 874 barrier (Fig. S17a) that extends from 8–3 km depth and also creates an afterslip gap (Fig.
 875 9e). This barrier is a well-constrained feature of our model ensemble and coincides with
 876 a low v_s area in along strike-direction imaged at 3 km depth (see Fig. 6d in Zeng et al.,
 877 2016), which might represent a geological or rheological feature.

878 Abercrombie et al. (2020) investigate source properties of repeating earthquake se-
 879 quences along the Parkfield section of the SAF. One analyzed sequence is located within
 880 the northwestern slip asperity of the 2004 Parkfield event. In their analysis, this sequence
 881 exhibits lower rupture velocities ($0.6\text{--}0.8v_s$), which is consistent with the second, mild,
 882 crack-like rupture phase of our model that is slower than the first pulse-like phase.

883 **4.3 Dynamic rupture arrest**

884 We find that distinct dynamic rupture-stopping mechanisms of different parts of
 885 coseismic rupture correlate with locally distinct afterslip evolution.

886 During dynamic rupture, elastic strain energy release competes with the consump-
 887 tion of fracture energy (Ke et al., 2018; Barras et al., 2023; Cocco et al., 2023). On a pla-

888 nar fault, dynamic rupture terminates if (i) it dynamically runs out of available strain
 889 energy; or (ii) local changes in normal stress or frictional conditions increase the required
 890 fracture energy or lead to velocity-strengthening conditions. At three shallow locations
 891 (yellow lines in Fig. 8a), coseismic rupture stops in regions with negative strength ex-
 892 cess. Comparing the coseismic rupture contours with the $b - a$ distribution (Fig. 2b)
 893 reveals that dynamic rupture terminates at these locations because it enters velocity-
 894 strengthening regions. Later, these three locations form the origin of main afterslip patches
 895 (Fig. 6a). There is no or very little afterslip evolving in regions where coseismic rupture
 896 is stopped due to local strength excess barriers.

897 The dynamic parameters L and \dot{s}_w additionally contribute to the dynamic rupture
 898 arrest. When coseismic rupture propagates into velocity-strengthening parts of the fault,
 899 slip rates cannot reach the locally increased \dot{s}_w values anymore (Fig. 2e), accelerating
 900 the rupture arrest. L noticeably increases above and beneath the coseismic rupture area
 901 (Fig. 2d). However, rupture arrest in the along-strike direction is not associated with
 902 an increase of L .

903 **4.4 Coseismic stress drop, friction drop and implications for the heat** 904 **flow paradox**

905 Our modeled low average coseismic stress drop may reflect the Parkfield section's
 906 comparably short recurrence times. The PM's average on-fault measured coseismic stress
 907 drop is 2.76 MPa which is rather small. We compare the on-fault dynamic stress drop
 908 to a seismological Brune-type stress drop estimate from calculating the average stress
 909 drop from the moment rate function spectrum using the following equation (e.g., Kaneko
 910 & Shearer, 2014):

$$911 \quad \Delta\sigma_{ef} = \frac{7}{16} \left(\frac{f_c}{k\beta} \right)^3 M_0, \quad (2)$$

912 where $f_c = 0.156$ Hz is the corner frequency of a Brune spectrum (Brune, 1970)
 913 fitted to the moment rate function spectrum of the PM (Fig. 3a), $\beta = 3600$ m/s the
 914 average S-wave velocity, $M_0 = 1.33 \times 10^{18}$ Nm the seismic moment, and k is a con-
 915 stant depending on the assumed source model. The resulting $\Delta\sigma_{ef} = 2.72$ MPa repro-
 916 duces the average on-fault stress drop when assuming $k = 0.26$, which is the value for
 917 S-wave spectra of the cohesive-zone model by Kaneko and Shearer (2014). Allmann and

918 Shearer (2009) found that moderate to large strike-slip earthquakes have a median stress
 919 drop of 10 MPa when assuming the Madariaga (1976) source model. We infer $\Delta\sigma_{ef} =$
 920 5.16 MPa when using $k = 0.21$ from the Madariaga source model, which is approximately
 921 half of the 10 MPa median value that Allmann and Shearer (2009) inferred for moder-
 922 ate to large strike-slip earthquakes. The mean f_c of the 10,500 models of the best-fitting
 923 model ensemble is 0.159 ± 0.018 Hz. Zhang et al. (2022) analyzed the spatial variabil-
 924 ity of stress drops of M_w 0–4 earthquakes along the Parkfield section of the SAF. They
 925 found exceptionally high stress drops close to the 2004 Parkfield hypocenter, which aligns
 926 with the area where our dynamic models also exhibit the highest stress drops. This cor-
 927 relation may reflect locally persistent frictional conditions that favor higher stress drop
 928 ruptures.

929 The SAF is a mature fault system that is assumed to operate under relatively low
 930 absolute stress levels based on the absence of a heat flow anomaly (e.g., Lachenbruch &
 931 Sass, 1980; Rice, 1992; Williams et al., 2004) and borehole measurements at the San An-
 932 dreas Fault Observatory at Depth (e.g., Hickman & Zoback, 2004). The absence of a heat
 933 flow anomaly above the SAF may be explained by statically strong and dynamically weak
 934 faults due to strong dynamic weakening at coseismic slip rates or by an effectively low
 935 static fault strength with respect to Byerlee’s law (Byerlee, 1978). A statically weak SAF
 936 may be caused by weak fault gouge (Lockner et al., 2011) or elevated pore fluid pressure
 937 (Rice, 1992).

938 Using a friction law with a rapid-weakening mechanism at coseismic slip rates al-
 939 lows faults to operate at low average shear stress (Noda et al., 2009; Ulrich et al., 2019).
 940 Our PM exhibits a small average reference friction drop ($f_0 - f_w$) of 0.058 within the
 941 coseismic rupture area, which would not align with the concept of statically strong and
 942 dynamically weak faults. However, the reference friction drop, is not necessarily repre-
 943 sentative of the effective friction drop. The low-velocity steady-state friction f_{LV} depends
 944 on the initial slip rate \dot{s}_{init} , the reference slip rate \dot{s}_0 , and $b-a$ (see Eq. 5 in Text S1).
 945 The maximum friction coefficient reached during rupture is not a prescribed model pa-
 946 rameter but varies along the fault and often exceeds f_0 , but rarely falls below this value.
 947 We calculate the effective friction drop as $f_{max} - f_{min} = \tau_{max}/\sigma_n - \tau_{min}/\sigma_n$ and infer
 948 an average value of 0.41 within the VW regions of the coseismic rupture area of the PM.
 949 This larger effective friction drop is yet smaller than expected from Byerlee’s law and
 950 a lithostatic pressure gradient.

951 We note that our ensemble of dynamic rupture models might be biased by the choice
952 of the initial model (IM), which has an even smaller average reference friction drop. Al-
953 though we cannot exclude that an alternative dynamic rupture model with a different
954 reference friction drop may fit the data, the construction of the IM (Sec. 3.1) demon-
955 strates that considerably larger fracture energy is likely incompatible with the earthquake’s
956 large-scale rupture properties. The comparably small average coseismic characteristic
957 slip distance of 3 cm is approximately 25% of the expected value considering the earth-
958 quake’s magnitude and rupture size (Gabriel et al., 2024; Palgunadi et al., 2024). As we
959 cannot achieve a higher reference friction drop without a shorter characteristic slip dis-
960 tance while preserving fracture energy, we consider a higher friction drop dynamic model
961 unlikely to be mechanically viable.

962 **4.5 Negative coseismic stress drop may promote afterslip and aftershocks**

963 In our PM, 7.9% of the coseismic rupture area exhibits a negative coseismic stress
964 drop. We find that the largest connected area of negative coseismic stress drop at 12–
965 13 km northwest to the hypocenter (Fig. 3c) coincides with the area of most afterslip
966 within the extent of the coseismic rupture (Fig. 6a). Mikumo and Miyatake (1995)’s dy-
967 namic rupture model of the 1984 Morgan Hill earthquake featured negative stress drops
968 to explain small slip over a shallow fault section, which they associated with velocity-
969 strengthening behavior (Quin, 1990; Blanpied et al., 1991). Similar to Mikumo and Miy-
970 atake (1995)’s model, our results include a small average strength excess, which likely
971 promotes negative stress drops. Using dynamic-weakening friction, Noda and Lapusta
972 (2010) inferred regions of negative stress drop also for velocity-weakening areas with slip
973 larger than the average slip.

974 We observe that areas of negative stress drop align with the depth of increased af-
975 tershock activity. Custódio et al. (2009) found that aftershocks tend to occur in regions
976 of negative stress change in a stress change model inferred from a kinematic slip model.
977 Here, we observe an interesting relationship between the aftershock locations and the slip
978 distribution of our PM, which is compatible with this observation. At the bottom and
979 the lateral edges of the coseismic rupture area, aftershocks are mostly located outside
980 of the coseismic rupture area (Fig. 6c), where a stress increase is expected (Fig. S18).
981 In contrast, the shallow aftershock clusters between 4–6 km depth occur still within the
982 coseismic rupture zone, where a static stress change model would produce a negative stress

983 change. In our rate-and-state friction model, shallow rupture is often stopped by velocity-
984 strengthening friction. The shallow aftershocks coincide with the transition from a velocity-
985 weakening to a velocity-strengthening regime (Fig. 2b). Our model demonstrates that
986 this transition zone can exhibit a considerable area of negative stress drop, which is com-
987 patible with increased aftershock activity.

988 **4.6 Correlations of kinematic parameters**

989 The relationship between kinematic parameters has been analyzed in previous en-
990 sembles of dynamic rupture models (Oglesby & Day, 2002; Guatteri et al., 2004; Schmedes
991 et al., 2010, 2012; Gabriel et al., 2013; Song et al., 2013; Mai et al., 2017; Vyas et al.,
992 2023) and differences may depend on the local heterogeneity of dynamic parameters. Schmedes
993 et al. (2010) generated a correlation matrix of kinematic rupture parameters from > 300
994 heterogenous strike-slip dynamic rupture models using linear slip-weakening or linear time-
995 weakening friction. Consistent with their results, we find correlations greater than 0.8
996 between rupture speed and peak slip rate, as well as between rise time and slip for the
997 best-fitting model ensemble (Fig. S19). While Schmedes et al. (2010) reported weak an-
998 tiorrelations between rise time and peak slip rate, and between rise time and rupture
999 speed, our ensemble shows these as weakly positive. Vyas et al. (2023) correlated kine-
1000 matic rupture parameters of dynamic rupture models with thermal pressurization and
1001 mostly homogeneous initial conditions. Contrary to our results, they find anticorrela-
1002 tions between peak slip rate and slip, rupture speed and slip, and rise time and peak slip
1003 rate. Despite the additional weakening effects due to thermal pressurization, we spec-
1004 ulate that these differences stem primarily from the homogeneous initial conditions and
1005 simple rupture dynamics, which create a shared dependence on rupture propagation dis-
1006 tance.

1007 **4.7 Limitations and future developments**

1008 The dynamic inversion is constrained by frequencies up to 0.5 Hz which limits the
1009 spatial and temporal resolution. However, due to the nonlinearity of the forward prob-
1010 lem and the physics-based constraints provided by rate-and-state friction, it remains chal-
1011 lenging to directly infer the achieved resolution from the data resolution. Nevertheless,
1012 small-scale features of our models need to be interpreted with care. We use rise time dif-
1013 ferences to differentiate between rupture styles, which appear reasonably constrained by

1014 the dynamic relations enforced by the friction law. The dynamic inversion tracks the rup-
1015 ture front, and thereby, constrains the rupture speed. The final model ensemble shows
1016 high rupture speeds near the hypocenter, consistent with array-based rupture front track-
1017 ing (Fig S16, Fletcher et al., 2006) and previous kinematic models (e.g., Liu et al., 2006;
1018 Custódio et al., 2009). High rupture speed correlates with high peak slip rate in our best-
1019 fitting model ensemble, where the correlation coefficient is 0.85 (Fig. S19). While the
1020 dynamic inversion constrains friction parameters and, consequently, radiation efficiency,
1021 resolving whether there is a weak slip rate tail (Lambert et al., 2021) using strong mo-
1022 tion data alone is difficult. Similarly, the observational estimation of rise time remains
1023 severely challenged by the limited resolution and inherent non-uniqueness of kinematic
1024 source inversions (Ide et al., 2005; Page et al., 2011; Gallovič & Ampuero, 2015). How-
1025 ever, in our inversion, GPS data additionally constrain the modeled slip and the rise time
1026 of an impulsive rupture with a high slip rate. This is supported by the rise time vari-
1027 ability of the initial impulsive phase within the model ensemble, which is mostly below
1028 0.25 s (Fig. 9). We set the threshold for computing rise time relatively high (> 0.1 m/s)
1029 to ensure reasonable constraints between crack- and pulse-like rupture (Text S3).

1030 Our 90-day afterslip simulation does not account for viscoelastic effects. Freed (2007)
1031 suggest that the 2004 Parkfield postseismic deformation was solely caused by afterslip,
1032 and viscoelastic relaxation and poroelastic rebound had no significant contribution. In
1033 distinction, Bruhat et al. (2011) argue that viscoelastic relaxation is required to explain
1034 as much as 20% of the postseismic displacement at the GPS station farthest from the
1035 source (LOWS, see Fig. 1a) 5 years after the earthquake. Based on their analysis, the
1036 contribution of viscoelastic relaxation to near-source displacements during the early post-
1037 seismic time may be negligible (see Fig. 8b in Bruhat et al., 2011). There is also evidence
1038 for deep afterslip from substantial acceleration of low-frequency earthquake (LFE) oc-
1039 currences (Shelly & Johnson, 2011; Johnson et al., 2013), deeper than our model domain.

1040 Despite running more than 2 million dynamic rupture forward simulations, our in-
1041 version visits only a tiny portion of the large model space associated with ≈ 1100 dy-
1042 namic parameters. Our inverse problem also has a large null space (model parameters
1043 not affecting the misfit) because wide parts of the fault do not slip significantly, which
1044 can be realized by a wide range of model parameters. By providing a reasonable IM and
1045 guiding the inversion during the convergence phase by occasionally selecting our preferred
1046 model and restarting all Markov chains with the chosen model, we were able to find an

1047 ensemble of models that explains the coseismic and postseismic data, which is a simi-
1048 lar approach to previous studies (Galovič et al., 2019b; Premus et al., 2022). However,
1049 our best-fitting model ensemble cannot be assumed to be completely independent of the
1050 initial model. In particular, many parameter combinations can facilitate dynamic rup-
1051 ture arrest without being constrained by subsequent afterslip. Parameters in these re-
1052 gions have high uncertainties, low impact on the misfit, and may still depend on the ini-
1053 tial model. While the model uncertainties we provide represent ranges of parameters that
1054 can fit the data, we cannot expect the uncertainty quantification to be mathematically
1055 complete in a Bayesian probabilistic sense.

1056 The overall similarity between models within the ensemble may bias the absolute
1057 correlation coefficients. We find that the correlations between the different dynamic pa-
1058 rameters of the ensemble (Fig. 11) are generally low (< 0.5). However, the correlation
1059 coefficients of the best-fitting model ensemble increase with the length of the Markov chains
1060 and might rise further when the inversion is continued. Longer Markov chains would re-
1061 duce the dependence on the initial model.

1062 The earthquake dynamic inversion problem suffers from the so-called “curse of di-
1063 mensionality” - the volume of the parameter space exponentially increases with the num-
1064 ber of parameters. Further increasing the computational resources consumed ($> 57,000$
1065 GPU hours for this study) will likely be impermissible or at least highly inefficient be-
1066 cause the error of the MCMC results decreases more slowly with the number of steps (Sokal,
1067 1997).

1068 Instead, future methodological improvements may be achieved by either (i) the in-
1069 troduction of advanced modeling methods or (ii) reducing the number of model param-
1070 eters. With respect to (i), new methods such as reduced-order modeling and machine
1071 learning techniques may aid in considerably speeding up the forward model calculation
1072 (Rekoske et al., 2023). Physics-based neural networks were recently applied to the rup-
1073 ture problem with rate and state friction and allow for dynamic parameter estimation
1074 as part of the training process (Rucker & Erickson, 2023). Recently, Stiernström et al.
1075 (2024) derived an adjoint-based inversion formulation for dynamic rupture, which may
1076 reduce the time-to-solution of dynamic source inversions but cannot provide model un-
1077 certainties. For (ii), reducing the number of control points by, e.g., decreasing their den-
1078 sity at the edges of the fault or places with no expected slip will decrease the dimension-

1079 ality of the forward problem. However, increasing the density of control points may open
 1080 new possibilities to constrain the inversion, e.g. by correlating dynamic parameters with
 1081 properties of repeating small earthquakes (e.g., Abercrombie et al., 2020). Similarly, us-
 1082 ing a simpler linear-slip weakening friction law requires fewer model parameters and com-
 1083 putational resources but can only capture coseismic rupture dynamics (e.g., Gallovič et
 1084 al., 2019b). Lastly, integrating additional datasets, such as surface creep data (Langbein
 1085 et al., 2006) or InSAR, given its much higher spatial resolution, may be promising fu-
 1086 ture directions.

1087 5 Conclusions

1088 In this study, we conduct a joint dynamic rupture and afterslip finite-fault inver-
 1089 sion of the 2004 M_w 6.0 Parkfield earthquake, resolving the spatial variability of prestress
 1090 and fault friction parameters across time scales. Using the best-fitting model ensemble,
 1091 we delineate the uncertainty bounds of dynamic model parameters and reveal their in-
 1092 herent trade-offs. The preferred dynamic model unifies the complexities of co- and post-
 1093 seismic fault slip, jointly constrained by seismic and geodetic observations. We observe
 1094 significant spatial heterogeneity in coseismic dynamic rupture and identify a pulse-like
 1095 rupture phase followed by a crack-like rupture phase. The two distinct coseismic rup-
 1096 ture phases are separated by a shallow strength barrier located 7–8 km northwest of the
 1097 hypocenter, which nearly arrests coseismic slip and subsequently causes a pronounced
 1098 gap in the 90-day afterslip evolution. Our joint rate-and-state framework elucidates dis-
 1099 tinct dynamic rupture termination mechanisms, which are closely tied to the subsequent
 1100 evolution of afterslip. Dynamic rupture entering velocity-strengthening regions that host
 1101 subsequent afterslip is a well-resolved and persistent feature of our model ensemble. Across
 1102 the entire area of fault slip, including regions hosting afterslip, the spatial average of b -
 1103 a levels at 0.000 (with a standard deviation of 0.0059). Postseismic slip rate functions
 1104 mostly resemble crack-like behavior with rise times gradually increasing with distance
 1105 to the edge of the coseismic rupture area. We detect a backward propagating afterslip
 1106 front, which aligns with delayed aftershock activity located above the hypocenter. Our
 1107 analysis provides data-constrained and physics-based estimates of source parameters and
 1108 their interactions. We observe areas of negative coseismic stress drop that may explain
 1109 the occurrence of shallow aftershock clusters within the coseismic rupture area. The in-
 1110 ferred friction drop aligns with a statically stronger and dynamically weaker Parkfield

1111 section of the San Andreas Fault. The 10,500 best-fitting model ensemble’s average co-
1112 coseismic radiation efficiency is 0.21, its coseismic stress drop is 2.73 MPa, and its aver-
1113 age postseismic stress drop is 0.39 MPa, despite similarly large co- and postseismic mo-
1114 ments. This study demonstrates how physics-based models using modern computational
1115 techniques can uncover new insights and unprecedented details of well-recorded earth-
1116 quakes.

1117 **6 Open Research**

1118 All seismic data are obtained through the CESMD (Center for Engineering Strong
1119 Motion Data) web service and we only use stations from the California Strong Motion
1120 Instrumentation Program (CSMIP, California Geological Survey, 1972). We use processed
1121 coseismic and postseismic GPS data by Jiang et al. (2021a), which are publicly avail-
1122 able (Jiang et al., 2021b). The FD3D.TSN (Premus et al., 2020) version and all required
1123 input files to run the dynamic source inversion of the 2004 Parkfield earthquake are avail-
1124 able (Schliwa, 2024).

1125 **Acknowledgments**

1126 The authors declare no conflict of interest. The manuscript greatly benefited from com-
1127 ments by Roland Bürgmann. We thank two anonymous reviewers, the Editor Rachel Aber-
1128 crombie, and the anonymous Associate Editor for their constructive comments. This study
1129 was supported by the European Union’s Horizon 2020 Research and Innovation Programme
1130 (TEAR, grant number 852992), Horizon Europe (ChEESE-2P, grant number 101093038,
1131 DT-GEO, grant number 101058129, and Geo-INQUIRE, grant number 101058518), the
1132 Deutsche Forschungsgemeinschaft (DFG, German Research Foundation, grant number
1133 495931446), the National Aeronautics and Space Administration (80NSSC20K0495), the
1134 National Science Foundation (grant numbers EAR-2225286, EAR-2121568, OAC-2139536,
1135 OAC-2311208) and the Statewide California Earthquake Center (SCEC awards 22135,
1136 23121). F. G. was supported by the Johannes Amos Comenius Programme (P JAC), project
1137 No. CZ.02.01.01/00/22_008/0004605, Natural and anthropogenic georisks. Computing
1138 resources were provided by the Institute of Geophysics of LMU Munich (Oeser et al., 2006).

1139 **References**

1140 Abercrombie, R. E., Chen, X., & Zhang, J. (2020). Repeating Earthquakes With

- 1141 Remarkably Repeatable Ruptures on the San Andreas Fault at Parkfield. *Geo-*
 1142 *physical Research Letters*, 47.
- 1143 Allmann, B. P., & Shearer, P. M. (2007). A High-Frequency Secondary Event Dur-
 1144 ing the 2004 Parkfield Earthquake. *Science*, 318.
- 1145 Allmann, B. P., & Shearer, P. M. (2009). Global variations of stress drop for moder-
 1146 ate to large earthquakes. *Journal of Geophysical Research: Solid Earth*, 114.
- 1147 Ampuero, J.-P., & Rubin, A. M. (2008). Earthquake nucleation on rate and state
 1148 faults – Aging and slip laws. *Journal of Geophysical Research: Solid Earth*,
 1149 113.
- 1150 Andrews, D. J. (1976). Rupture velocity of plane strain shear cracks. *Journal of*
 1151 *Geophysical Research*, 81.
- 1152 Bakun, W. H., Aagaard, B., Dost, B., Ellsworth, W., Hardebeck, J., Harris, R., ...
 1153 Waldhauser, F. (2005). Implications for Prediction and Hazard Assessment
 1154 from the 2004 Parkfield Earthquake. *Nature*, 437.
- 1155 Bakun, W. H., & Lindh, A. G. (1985). The Parkfield, California, Earthquake Predic-
 1156 tion Experiment. *Science*, 229.
- 1157 Bakun, W. H., & McEvilly, T. V. (1984). Recurrence models and Parkfield, Califor-
 1158 nia, earthquakes. *Journal of Geophysical Research: Solid Earth*, 89.
- 1159 Bao, H., Ampuero, J. P., Meng, L., Fielding, E., Liang, C., Milliner, C., ... Huang,
 1160 H. (2019). Early and persistent supershear rupture of the 2018 magnitude 7.5
 1161 Palu earthquake. *Nature Geoscience*, 12.
- 1162 Barbot, S., Fialko, Y., & Bock, Y. (2009). Postseismic deformation due to the Mw
 1163 6.0 2004 Parkfield earthquake: Stress-driven creep on a fault with spatially
 1164 variable rate-and-state friction parameters. *Journal of Geophysical Research:*
 1165 *Solid Earth*, 114.
- 1166 Barbot, S., Lapusta, N., & Avouac, J.-P. (2012). Under the Hood of the Earthquake
 1167 Machine: Toward Predictive Modeling of the Seismic Cycle. *Science*, 336.
- 1168 Barras, F., Thøgersen, K., Aharonov, E., & Renard, F. (2023). How Do Earthquakes
 1169 Stop? Insights From a Minimal Model of Frictional Rupture. *Journal of Geo-*
 1170 *physical Research: Solid Earth*, 128.
- 1171 Bilham, R. (2005). Coseismic Strain and the Transition to Surface Afterslip
 1172 Recorded by Creepmeters near the 2004 Parkfield Epicenter. *Seismological*
 1173 *Research Letters*, 76.

- 1174 Blanpied, M. L., Lockner, D. A., & Byerlee, J. D. (1991). Fault stability inferred
 1175 from granite sliding experiments at hydrothermal conditions. *Geophysical Re-*
 1176 *search Letters*, 18.
- 1177 Brengman, C. M. J., Barnhart, W. D., Mankin, E. H., & Miller, C. N. (2019).
 1178 Earthquake-Scaling Relationships from Geodetically Derived Slip Distribu-
 1179 tions. *Bulletin of the Seismological Society of America*, 109.
- 1180 Bruhat, L., Barbot, S., & Avouac, J.-P. (2011). Evidence for postseismic deforma-
 1181 tion of the lower crust following the 2004 Mw6.0 Parkfield earthquake. *Journal*
 1182 *of Geophysical Research: Solid Earth*, 116.
- 1183 Brune, J. N. (1970). Tectonic stress and the spectra of seismic shear waves from
 1184 earthquakes. *Journal of Geophysical Research*, 75.
- 1185 Burridge, R., Conn, G., & Freund, L. B. (1979). The stability of a rapid mode
 1186 II shear crack with finite cohesive traction. *Journal of Geophysical Research:*
 1187 *Solid Earth*, 84.
- 1188 Byerlee, J. D. (1978). Friction of rocks. *Pure and Applied Geophysics*, 116.
- 1189 California Geological Survey. (1972). *California strong motion instrumentation pro-*
 1190 *gram*. International Federation of Digital Seismograph Networks. doi: 10.7914/
 1191 B34Q-BB70
- 1192 Cattania, C., Hainzl, S., Wang, L., Enescu, B., & Roth, F. (2015). Aftershock
 1193 triggering by postseismic stresses: A study based on Coulomb rate-and-state
 1194 models. *Journal of Geophysical Research: Solid Earth*, 120.
- 1195 Chang, S.-H., Avouac, J.-P., Barbot, S., & Lee, J.-C. (2013). Spatially variable fault
 1196 friction derived from dynamic modeling of aseismic afterslip due to the 2004
 1197 Parkfield earthquake. *Journal of Geophysical Research: Solid Earth*, 118.
- 1198 Churchill, R. M., Werner, M. J., Biggs, J., & Fagereng, Å. (2022). Relative Afterslip
 1199 Moment Does Not Correlate With Aftershock Productivity: Implications for
 1200 the Relationship Between Afterslip and Aftershocks. *Geophysical Research*
 1201 *Letters*, 49.
- 1202 Churchill, R. M., Werner, M. J., Biggs, J., & Fagereng, r. (2024). Spatial Relation-
 1203 ships Between Coseismic Slip, Aseismic Afterslip, and On-Fault Aftershock
 1204 Density in Continental Earthquakes. *Journal of Geophysical Research: Solid*
 1205 *Earth*, 129.
- 1206 Cocco, M., Aretusini, S., Cornelio, C., Nielsen, S. B., Spagnuolo, E., Tinti, E., &

- 1207 Di Toro, G. (2023). Fracture Energy and Breakdown Work During Earth-
 1208 quakes. *Annual Review of Earth and Planetary Sciences*, 51.
- 1209 Cocco, M., & Bizzarri, A. (2002). On the slip-weakening behavior of rate- and state
 1210 dependent constitutive laws. *Geophysical Research Letters*, 29.
- 1211 Cotton, F., & Coutant, O. (1997). Dynamic stress variations due to shear faults in a
 1212 plane-layered medium. *Geophysical Journal International*, 128.
- 1213 Custódio, S., Liu, P., & Archuleta, R. J. (2005). The 2004 Mw6.0 Parkfield, Cali-
 1214 fornia, earthquake: Inversion of near-source ground motion using multiple data
 1215 sets. *Geophysical Research Letters*, 32.
- 1216 Custódio, S., Page, M. T., & Archuleta, R. J. (2009). Constraining earthquake
 1217 source inversions with GPS data: 2. A two-step approach to combine seismic
 1218 and geodetic data sets. *Journal of Geophysical Research: Solid Earth*, 114.
- 1219 Dalguer, L. A., & Day, S. M. (2007). Staggered-grid split-node method for sponta-
 1220 neous rupture simulation. *Journal of Geophysical Research: Solid Earth*, 112.
- 1221 Das, S. (2015). Supershear Earthquake Ruptures – Theory, Methods, Laboratory
 1222 Experiments and Fault Superhighways: An Update. *Geotechnical, Geological
 1223 and Earthquake Engineering*, 39.
- 1224 Day, S. M., Dalguer, L. A., Lapusta, N., & Liu, Y. (2005). Comparison of finite
 1225 difference and boundary integral solutions to three-dimensional spontaneous
 1226 rupture. *Journal of Geophysical Research: Solid Earth*, 110.
- 1227 Dieterich, J. H. (1992). Earthquake nucleation on faults with rate-and state-
 1228 dependent strength. *Tectonophysics*, 211.
- 1229 Fletcher, J. B., Spudich, P., & Baker, L. M. (2006). Rupture Propagation of the
 1230 2004 Parkfield, California, Earthquake from Observations at the UPSAR. *Bul-
 1231 letin of the Seismological Society of America*, 96.
- 1232 Freed, A. M. (2007). Afterslip (and only afterslip) following the 2004 Parkfield, Cali-
 1233 fornia, earthquake. *Geophysical Research Letters*, 34.
- 1234 Freund, L. B. (1979). The mechanics of dynamic shear crack propagation. *Journal of
 1235 Geophysical Research: Solid Earth*, 84.
- 1236 Fukuyama, E., & Mikumo, T. (1993). Dynamic rupture analysis: Inversion for the
 1237 source process of the 1990 Izu-Oshima, Japan, earthquake ($M = 6.5$). *Journal
 1238 of Geophysical Research: Solid Earth*, 98.
- 1239 Gabriel, A.-A., Ampuero, J.-P., Dalguer, L. A., & Mai, P. M. (2012). The transition

- 1240 of dynamic rupture styles in elastic media under velocity-weakening friction.
 1241 *Journal of Geophysical Research: Solid Earth*, 117.
- 1242 Gabriel, A.-A., Ampuero, J.-P., Dalguer, L. A., & Mai, P. M. (2013). Source proper-
 1243 ties of dynamic rupture pulses with off-fault plasticity. *Journal of Geophysical*
 1244 *Research: Solid Earth*, 118.
- 1245 Gabriel, A.-A., Garagash, D. I., Palgunadi, K. H., & Mai, P. M. (2024). Fault
 1246 size-dependent fracture energy explains multiscale seismicity and cascading
 1247 earthquakes. *Science*, 385.
- 1248 Gallovič, F., Valentová, L., Ampuero, J.-P., & Gabriel, A.-A. (2019a). Bayesian Dy-
 1249 namic Finite-Fault Inversion: 1. Method and Synthetic Test. *Journal of Geo-*
 1250 *physical Research: Solid Earth*, 124.
- 1251 Gallovič, F., Valentová, L., Ampuero, J.-P., & Gabriel, A.-A. (2019b). Bayesian
 1252 Dynamic Finite-Fault Inversion: 2. Application to the 2016 Mw 6.2 Amatrice,
 1253 Italy, Earthquake. *Journal of Geophysical Research: Solid Earth*, 124.
- 1254 Gallovič, F., Zahradník, J., Plicka, V., Sokos, E., Evangelidis, C., Fountoulakis, I., &
 1255 Turhan, F. (2020). Complex rupture dynamics on an immature fault during
 1256 the 2020 Mw 6.8 Elazığ earthquake, Turkey. *Commun. Earth Environ.*, 1.
- 1257 Gallovič, F. (2008). Heterogeneous Coulomb stress perturbation during earthquake
 1258 cycles in a 3D rate-and-state fault model. *Geophysical Research Letters*, 35.
- 1259 Gallovič, F., & Ampuero, J.-P. (2015). A New Strategy to Compare Inverted Rup-
 1260 ture Models Exploiting the Eigenstructure of the Inverse Problem. *Seismologi-*
 1261 *cal Research Letters*, 86.
- 1262 Guatteri, M., Mai, P. M., & Beroza, G. C. (2004). A Pseudo-Dynamic Approxima-
 1263 tion to Dynamic Rupture Models for Strong Ground Motion Prediction. *Bul-*
 1264 *letin of the Seismological Society of America*, 94.
- 1265 Hallo, M., & Gallovič, F. (2016). Fast and cheap approximation of Green func-
 1266 tion uncertainty for waveform-based earthquake source inversions. *Geophysical*
 1267 *Journal International*, 207.
- 1268 Harris, R. A., Barall, M., Aagaard, B., Ma, S., Roten, D., Olsen, K., . . . Dalguer,
 1269 L. (2018). A Suite of Exercises for Verifying Dynamic Earthquake Rupture
 1270 Codes. *Seismological Research Letters*, 89.
- 1271 Heaton, T. H. (1990). Evidence for and implications of self-healing pulses of slip in
 1272 earthquake rupture. *Physics of the Earth and Planetary Interiors*, 64.

- 1273 Heinecke, A., Breuer, A., Rettenberger, S., Bader, M., Gabriel, A.-A., Pelties, C.,
 1274 ... Dubey, P. (2014). Petascale High Order Dynamic Rupture Earthquake
 1275 Simulations on Heterogeneous Supercomputers. In *SC '14: Proceedings of*
 1276 *the International Conference for High Performance Computing, Networking,*
 1277 *Storage and Analysis*.
- 1278 Hickman, S., & Zoback, M. (2004). Stress orientations and magnitudes in the
 1279 SAFOD pilot hole. *Geophysical Research Letters*, *31*.
- 1280 Ide, S., Beroza, G. C., & Mcguire, J. J. (2005). Imaging Earthquake Source Com-
 1281 plexity. In *Seismic Earth: Array Analysis of Broadband Seismograms* (p. 117-
 1282 135). American Geophysical Union (AGU).
- 1283 Jiang, J., Bock, Y., & Klein, E. (2021a). Coevolving early afterslip and aftershock
 1284 signatures of a San Andreas fault rupture. *Science Advances*, *7*.
- 1285 Jiang, J., Bock, Y., & Klein, E. (2021b). *Data and Models for 'Coevolving Early*
 1286 *Afterslip and Aftershock Signatures of a San Andreas Fault Rupture'* [Dataset].
 1287 Zenodo. doi: 10.5281/zenodo.4278477
- 1288 Johanson, I. A., Fielding, E. J., Rolandone, F., & Bürgmann, R. (2006). Coseismic
 1289 and Postseismic Slip of the 2004 Parkfield Earthquake from Space-Geodetic
 1290 Data. *Bulletin of the Seismological Society of America*, *96*.
- 1291 Johnson, K. M., Bürgmann, R., & Larson, K. (2006). Frictional Properties on the
 1292 San Andreas Fault near Parkfield, California, Inferred from Models of After-
 1293 slip following the 2004 Earthquake. *Bulletin of the Seismological Society of*
 1294 *America*, *96*.
- 1295 Johnson, K. M., Shelly, D. R., & Bradley, A. M. (2013). Simulations of tremor-
 1296 related creep reveal a weak crustal root of the San Andreas Fault. *Geophysical*
 1297 *Research Letters*, *40*.
- 1298 Jolivet, R., Simons, M., Agram, P. S., Duputel, Z., & Shen, Z.-K. (2015). Aseismic
 1299 slip and seismogenic coupling along the central San Andreas Fault. *Geophysical*
 1300 *Research Letters*, *42*.
- 1301 Kagan, Y. Y., & Houston, H. (2005). Relation between mainshock rupture process
 1302 and Omori's law for aftershock moment release rate. *Geophysical Journal In-*
 1303 *ternational*, *163*.
- 1304 Kaneko, Y., & Shearer, P. M. (2014). Seismic source spectra and estimated stress
 1305 drop derived from cohesive-zone models of circular subshear rupture. *Geophys-*

- 1306 *ical Journal International*, 197.
- 1307 Ke, C.-Y., McLaskey, G. C., & Kammer, D. S. (2018). Rupture Termination in
1308 Laboratory-Generated Earthquakes. *Geophysical Research Letters*, 45.
- 1309 Kim, A., & Dreger, D. S. (2008). Rupture process of the 2004 Parkfield earthquake
1310 from near-fault seismic waveform and geodetic records. *Journal of Geophysical
1311 Research: Solid Earth*, 113.
- 1312 Kostka, F., & Gallovič, F. (2016). Static Coulomb stress load on a three-dimensional
1313 rate-and-state fault: Possible explanation of the anomalous delay of the 2004
1314 Parkfield earthquake. *Journal of Geophysical Research: Solid Earth*, 121.
- 1315 Krenz, L., Uphoff, C., Ulrich, T., Gabriel, A.-A., Abrahams, L. S., Dunham, E. M.,
1316 & Bader, M. (2021). 3D acoustic-elastic coupling with gravity: the dynam-
1317 ics of the 2018 Palu, Sulawesi earthquake and tsunami. In *Proceedings of the
1318 international conference for high performance computing, networking, storage
1319 and analysis*. Association for Computing Machinery.
- 1320 Lachenbruch, A. H., & Sass, J. H. (1980). Heat flow and energetics of the San An-
1321 dreas Fault Zone. *Journal of Geophysical Research: Solid Earth*, 85.
- 1322 Lambert, V., Lapusta, N., & Perry, S. (2021). Propagation of large earthquakes as
1323 self-healing pulses or mild cracks. *Nature*, 591.
- 1324 Langbein, J., Borchardt, R., Dreger, D., Fletcher, J., Hardebeck, J. L., Hellweg, M.,
1325 ... Treiman, J. A. (2005). Preliminary Report on the 28 September 2004, M
1326 6.0 Parkfield, California Earthquake. *Seismological Research Letters*, 76.
- 1327 Langbein, J., Murray, J. R., & Snyder, H. A. (2006). Coseismic and Initial Post-
1328 seismic Deformation from the 2004 Parkfield, California, Earthquake, Observed
1329 by Global Positioning System, Electronic Distance Meter, Creepmeters, and
1330 Borehole Strainmeters. *Bulletin of the Seismological Society of America*, 96.
- 1331 Lewis, M. A., & Ben-Zion, Y. (2010). Diversity of fault zone damage and trapping
1332 structures in the Parkfield section of the San Andreas Fault from comprehen-
1333 sive analysis of near fault seismograms. *Geophysical Journal International*,
1334 183.
- 1335 Li, Y.-G., Leary, P., Aki, K., & Malin, P. (1990). Seismic Trapped Modes in the
1336 Oroville and San Andreas Fault Zones. *Science*.
- 1337 Lienkaemper, J. J., Baker, B., & McFarland, F. S. (2006). Surface Slip Associ-
1338 ated with the 2004 Parkfield, California, Earthquake Measured on Alinement

- 1339 Arrays. *Bulletin of the Seismological Society of America*, 96.
- 1340 Lisowski, M., Savage, J. C., & Prescott, W. H. (1991). The velocity field along the
1341 San Andreas Fault in central and southern California. *Journal of Geophysical*
1342 *Research: Solid Earth*, 96.
- 1343 Liu, P., Custódio, S., & Archuleta, R. J. (2006). Kinematic Inversion of the 2004 M
1344 6.0 Parkfield Earthquake Including an Approximation to Site Effects. *Bulletin*
1345 *of the Seismological Society of America*, 96.
- 1346 Lockner, D., Morrow, C., Moore, D., & Hickman, S. (2011). Low strength of deep
1347 San Andreas Fault gouge from SAFOD core. *Nature*, 472.
- 1348 Lui, S. K. Y., & Lapusta, N. (2018). Modeling High Stress Drops, Scaling, Inter-
1349 action, and Irregularity of Repeating Earthquake Sequences Near Parkfield.
1350 *Journal of Geophysical Research: Solid Earth*, 123.
- 1351 Ma, S., Custódio, S., Archuleta, R. J., & Liu, P. (2008). Dynamic modeling of
1352 the 2004 Mw 6.0 Parkfield, California, earthquake. *Journal of Geophysical*
1353 *Research: Solid Earth*, 113.
- 1354 Madariaga, R. (1976). Dynamics of an expanding circular fault. *Bulletin of the Seis-*
1355 *mological Society of America*, 66.
- 1356 Madariaga, R. (1977). High-frequency radiation from crack (stress drop) models of
1357 earthquake faulting. *Geophysical Journal International*, 51.
- 1358 Madden, E. H., Ulrich, T., & Gabriel, A.-A. (2022). The State of Pore Fluid Pres-
1359 sure and 3-D Megathrust Earthquake Dynamics. *Journal of Geophysical Re-*
1360 *search: Solid Earth*, 127.
- 1361 Mai, P., Galis, M., Thingbaijam, K. K., Vyas, J., & Dunham, E. (2017). Account-
1362 ing for Fault Roughness in Pseudo-Dynamic Ground-Motion Simulations. *Pure*
1363 *and Applied Geophysics*, 174.
- 1364 Mikumo, T., & Miyatake, T. (1995). Heterogeneous distribution of dynamic stress
1365 drop and relative fault strength recovered from the results of waveform inver-
1366 sion: the 1984 Morgan Hill, California, earthquake. *Bulletin of the Seismologi-*
1367 *cal Society of America*, 85.
- 1368 Murray, J., & Langbein, J. (2006). Slip on the San Andreas Fault at Parkfield, Cal-
1369 ifornia, over Two Earthquake Cycles, and the Implications for Seismic Hazard.
1370 *Bulletin of the Seismological Society of America*, 96.
- 1371 Neves, M., Peng, Z., & Lin, G. (2022). A High-Resolution Earthquake Catalog

- 1372 for the 2004 Mw 6 Parkfield Earthquake Sequence Using a Matched Filter
1373 Technique. *Seismological Research Letters*, 94.
- 1374 Noda, H., Dunham, E. M., & Rice, J. R. (2009). Earthquake ruptures with thermal
1375 weakening and the operation of major faults at low overall stress levels. *Journal of Geophysical Research: Solid Earth*, 114.
- 1376
- 1377 Noda, H., & Lapusta, N. (2010). 3D simulations of long-term fault slip with dy-
1378 namic weakening: relation between locked patches and earthquake-induced
1379 stress changes. In *Workshop on earthquake source dynamics: Data and data-
1380 constrained numerical modeling*.
- 1381 Oeser, J., Bunge, H.-P., & Mohr, M. (2006). Cluster design in the earth sciences
1382 tethys. In M. Gerndt & D. Kranzlmüller (Eds.), *High performance computing
1383 and communications*. Springer Berlin Heidelberg.
- 1384 Oglesby, D. D., & Day, S. M. (2002). Stochastic Fault Stress: Implications for Fault
1385 Dynamics and Ground Motion. *Bulletin of the Seismological Society of Amer-
1386 ica*, 92.
- 1387 Okada, Y. (1985). Surface deformation due to shear and tensile faults in a half-
1388 space. *Bulletin of the Seismological Society of America*, 75.
- 1389 Olsen, K. B., Day, S. M., & Bradley, C. R. (2003). Estimation of Q for Long-Period
1390 (>2 sec) Waves in the Los Angeles Basin. *Bulletin of the Seismological Society
1391 of America*, 93.
- 1392 Page, M. T., Custódio, S., Archuleta, R. J., & Carlson, J. M. (2009). Constraining
1393 earthquake source inversions with GPS data: 1. Resolution-based removal of
1394 artifacts. *Journal of Geophysical Research: Solid Earth*, 114.
- 1395 Page, M. T., Mai, P. M., & Schorlemmer, D. (2011). Testing Earthquake Source In-
1396 version Methodologies. *Eos, Transactions American Geophysical Union*, 92.
- 1397 Palgunadi, K. H., Gabriel, A.-A., Garagash, D. I., Ulrich, T., & Mai, P. M. (2024).
1398 Rupture Dynamics of Cascading Earthquakes in a Multiscale Fracture Net-
1399 work. *Journal of Geophysical Research: Solid Earth*, 129.
- 1400 Peng, Z., & Zhao, P. (2009). Migration of early aftershocks following the 2004 Park-
1401 field earthquake. *Nature Geoscience*, 2.
- 1402 Perrin, G., Rice, J. R., & Zheng, G. (1995). Self-healing slip pulse on a frictional
1403 surface. *Journal of the Mechanics and Physics of Solids*, 43.
- 1404 Peyrat, S., & Olsen, K. B. (2004). Nonlinear dynamic rupture inversion of the 2000

- 1405 Western Tottori, Japan, earthquake. *Geophysical Research Letters*, 31.
- 1406 Premus, J., Gallovič, F., & Ampuero, J.-P. (2022). Bridging time scales of faulting:
1407 From coseismic to postseismic slip of the M_w 6.0 2014 South Napa, California
1408 earthquake. *Science Advances*, 8.
- 1409 Premus, J., Gallovič, F., Hanyk, L., & Gabriel, A. (2020). FD3D-TSN: A Fast and
1410 Simple Code for Dynamic Rupture Simulations with GPU Acceleration. *Seis-*
1411 *mological Research Letters*, 91.
- 1412 Press, F. (1968). Earth models obtained by Monte Carlo Inversion. *Journal of Geo-*
1413 *physical Research (1896-1977)*, 73.
- 1414 Pulido, N., & Dalguer, L. A. (2009). Estimation of the High-Frequency Radiation
1415 of the 2000 Tottori (Japan) Earthquake Based on a Dynamic Model of Fault
1416 Rupture: Application to the Strong Ground Motion Simulation. *Bulletin of the*
1417 *Seismological Society of America*, 99.
- 1418 Quin, H. (1990). Dynamic stress drop and rupture dynamics of the October 15, 1979
1419 Imperial Valley, California, earthquake. *Tectonophysics*, 175.
- 1420 Rekoske, J. M., Gabriel, A.-A., & May, D. A. (2023). Instantaneous Physics-Based
1421 Ground Motion Maps Using Reduced-Order Modeling. *Journal of Geophysical*
1422 *Research: Solid Earth*, 128.
- 1423 Rice, J. R. (1992). Fault Stress States, Pore Pressure Distributions, and the Weak-
1424 ness of the San Andreas Fault. In B. Evans & T. fong Wong (Eds.), *Fault*
1425 *mechanics and transport properties of rocks* (Vol. 51, p. 475-503). Academic
1426 Press.
- 1427 Rice, J. R. (1993). Spatio-temporal complexity of slip on a fault. *Journal of Geo-*
1428 *physical Research: Solid Earth*, 98.
- 1429 Rucker, C., & Erickson, B. A. (2023). *Physics-Informed Deep Learning of Rate-and-*
1430 *State Fault Friction*.
- 1431 Ruina, A. (1983). Slip instability and state variable friction laws. *Journal of Geo-*
1432 *physical Research: Solid Earth*, 88.
- 1433 Rymer, M. J., Tinsley, I., John C., Treiman, J. A., Arrowsmith, J. R., Clahan,
1434 K. B., Rosinski, A. M., . . . Bawden, G. W. (2006). Surface Fault Slip As-
1435 sociated with the 2004 Parkfield, California, Earthquake. *Bulletin of the*
1436 *Seismological Society of America*, 96.
- 1437 Schliwa, N. (2024). *FD3D-TSN/2004Parkfield* [Software]. Zenodo. doi: 10.5281/

1438 zenodo.11072717

1439 Schliwa, N., & Gabriel, A. (2023). Equivalent Near-Field Corner Frequency Analysis
1440 of 3D Dynamic Rupture Simulations Reveals Dynamic Source Effects. *Seismo-*
1441 *logical Research Letters*.

1442 Schmedes, J., Archuleta, R. J., & Lavallée, D. (2010). Correlation of earthquake
1443 source parameters inferred from dynamic rupture simulations. *Journal of Geo-*
1444 *physical Research: Solid Earth*, 115.

1445 Schmedes, J., Archuleta, R. J., & Lavallée, D. (2012). A kinematic rupture model
1446 generator incorporating spatial interdependency of earthquake source paramete-
1447 ters. *Geophysical Journal International*, 192.

1448 Shakal, A., Haddadi, H., Graizer, V., Lin, K., & Huang, M. (2006). Some Key
1449 Features of the Strong-Motion Data from the M 6.0 Parkfield, California,
1450 Earthquake of 28 September 2004. *Bulletin of the Seismological Society of*
1451 *America*, 96.

1452 Shelly, D. R., & Johnson, K. M. (2011). Tremor reveals stress shadowing, deep
1453 postseismic creep, and depth-dependent slip recurrence on the lower-crustal
1454 San Andreas fault near Parkfield. *Geophysical Research Letters*, 38.

1455 Shi, Z., & Day, S. M. (2013). Rupture dynamics and ground motion from 3-D rough-
1456 fault simulations. *Journal of Geophysical Research: Solid Earth*, 118.

1457 Simpson, R. W., Barall, M., Langbein, J., Murray, J. R., & Rymer, M. J. (2006).
1458 San Andreas Fault Geometry in the Parkfield, California, Region. *Bulletin of*
1459 *the Seismological Society of America*, 96.

1460 Sokal, A. (1997). Monte carlo methods in statistical mechanics: Foundations and
1461 new algorithms. In *Functional integration: Basics and applications*. Springer
1462 US.

1463 Song, S. G., Dalguer, L. A., & Mai, P. M. (2013). Pseudo-dynamic source modelling
1464 with 1-point and 2-point statistics of earthquake source parameters. *Geophysi-*
1465 *cal Journal International*, 196.

1466 Stiernström, V., Almquist, M., & Dunham, E. M. (2024). *Adjoint-based inversion*
1467 *for stress and frictional parameters in earthquake modeling*.

1468 Suppe, J. (2014). Fluid overpressures and strength of the sedimentary upper crust.
1469 *Journal of Structural Geology*, 69.

1470 Taufiqurrahman, T., Gabriel, A.-A., Li, D., Ulrich, T., Li, B., Carena, S., ...

- 1471 Gallovič, F. (2023). Dynamics, interactions and delays of the 2019 Ridge-
1472 crest rupture sequence. *Nature*.
- 1473 Thomas, M. Y., Lapusta, N., Noda, H., & Avouac, J.-P. (2014). Quasi-dynamic
1474 versus fully dynamic simulations of earthquakes and aseismic slip with and
1475 without enhanced coseismic weakening. *Journal of Geophysical Research: Solid*
1476 *Earth*, 119.
- 1477 Thurber, C., Zhang, H., Waldhauser, F., Hardebeck, J., Michael, A., & Eberhart-
1478 Phillips, D. (2006). Three-Dimensional Compressional Wavespeed Model,
1479 Earthquake Relocations, and Focal Mechanisms for the Parkfield, California,
1480 Region. *Bulletin of the Seismological Society of America*, 96.
- 1481 Tinti, E., Casarotti, E., Ulrich, T., Taufiqurrahman, T., Li, D., & Gabriel, A.-A.
1482 (2021). Constraining families of dynamic models using geological, geodetic
1483 and strong ground motion data: The Mw 6.5, October 30th, 2016, Norcia
1484 earthquake, Italy. *Earth and Planetary Science Letters*, 576.
- 1485 Titus, S. J., DeMets, C., & Tikoff, B. (2005). New slip rate estimates for the creep-
1486 ing segment of the San Andreas fault, California. *Geology*, 33.
- 1487 Tong, X., Sandwell, D. T., & Smith-Konter, B. (2013). High-resolution interseis-
1488 mic velocity data along the San Andreas Fault from GPS and InSAR. *Journal*
1489 *of Geophysical Research: Solid Earth*, 118.
- 1490 Twardzik, C., Das, S., & Madariaga, R. (2014). Inversion for the physical param-
1491 eters that control the source dynamics of the 2004 Parkfield earthquake. *Jour-*
1492 *nal of Geophysical Research: Solid Earth*, 119.
- 1493 Twardzik, C., Madariaga, R., Das, S., & Custódio, S. (2012). Robust features of
1494 the source process for the 2004 Parkfield, California, earthquake from strong-
1495 motion seismograms. *Geophysical Journal International*, 191.
- 1496 Ulrich, T., Gabriel, A.-A., Ampuero, J.-P., & Xu, W. (2019). Dynamic viability of
1497 the 2016 Mw 7.8 Kaikōura earthquake cascade on weak crustal faults. *Nature*
1498 *Communications*.
- 1499 Uphoff, C., Rettenberger, S., Bader, M., Madden, E. H., Ulrich, T., Wollherr, S., &
1500 Gabriel, A.-A. (2017). Extreme scale multi-physics simulations of the tsunami-
1501 genic 2004 sumatra megathrust earthquake. In *Proceedings of the international*
1502 *conference for high performance computing, networking, storage and analysis*.
1503 Association for Computing Machinery.

- 1504 Utsu, T., Ogata, Y., S, R., & Matsu'ura. (1995). The Centenary of the Omori For-
1505 mula for a Decay Law of Aftershock Activity. *Journal of Physics of the Earth*,
1506 43.
- 1507 Vavra, E., Fialko, Y., Rockwell, T. K., Bilham, R., Stepancikova, P., Stemberk, J.,
1508 ... Stemberk, J. (2023). Characteristic Slow-Slip Events on the Superstition
1509 Hills Fault, Southern California. *ESS Open Archive*.
- 1510 Vyas, J. C., Gabriel, A., Ulrich, T., Mai, P. M., & Ampuero, J. (2023). How Does
1511 Thermal Pressurization of Pore Fluids Affect 3D Strike-Slip Earthquake Dy-
1512 namics and Ground Motions? *Bulletin of the Seismological Society of America*,
1513 113.
- 1514 Wen, Y., Cai, J., He, K., & Xu, C. (2024). Dynamic Rupture of the 2021 MW
1515 7.4 Maduo Earthquake: An Intra-Block Event Controlled by Fault Geometry.
1516 *Journal of Geophysical Research: Solid Earth*, 129.
- 1517 Williams, C. F., Grubb, F. V., & Galanis Jr., S. P. (2004). Heat flow in the SAFOD
1518 pilot hole and implications for the strength of the San Andreas Fault. *Geo-*
1519 *physical Research Letters*, 31.
- 1520 Zeng, X., Thurber, C. H., Shelly, D. R., Harrington, R. M., Cochran, E. S., Benning-
1521 ton, N. L., ... McClement, K. (2016). 3-D P- and S-wave velocity structure
1522 and low-frequency earthquake locations in the Parkfield, California region.
1523 *Geophysical Journal International*, 206.
- 1524 Zhang, J., Chen, X., & Abercrombie, R. E. (2022). Spatiotemporal Variability of
1525 Earthquake Source Parameters at Parkfield, California, and Their Relationship
1526 With the 2004 M6 Earthquake. *Journal of Geophysical Research: Solid Earth*,
1527 127.
- 1528 Zhao, Z., & Yue, H. (2023). A two-step inversion for fault frictional properties using
1529 a temporally varying afterslip model and its application to the 2019 Ridgecrest
1530 earthquake. *Earth and Planetary Science Letters*, 602.
- 1531 Zheng, G., & Rice, J. R. (1998). Conditions under which velocity-weakening friction
1532 allows a self-healing versus a cracklike mode of rupture. *Bulletin of the Seismo-*
1533 *logical Society of America*, 88.

Supporting Information for ”The linked complexity of coseismic and postseismic faulting revealed by seismo-geodetic dynamic inversion of the 2004 Parkfield earthquake”

Nico Schliwa ¹, Alice-Agnes Gabriel ^{2,1}, Jan Premus ³, František Gallovič ⁴

¹Ludwig-Maximilians-Universität München, Munich, Germany

²Scripps Institution of Oceanography, UC San Diego, La Jolla, CA, USA

³Côte d’Azur University, Nice, France

⁴Charles University, Prague, Czech Republic

Contents of this file

1. Text S1 to S3
2. Figures S1 to S20
3. Tables S1 to S2

Additional Supporting Information (Files uploaded separately)

1. Captions for Movies S1 to S2

Text S1: Fast-velocity-weakening rate-and-state friction

We use a fast-velocity-weakening rate-and-state friction law (Ampuero & Ben-Zion, 2008; Noda et al., 2009) to simulate coseismic and postseismic slip in the same modeling framework (Premus et al., 2022). The following equations govern the fault's frictional resistance (Fig. 1b, Dunham et al., 2011):

$$\tau = \sigma_n a \operatorname{arsinh} \left[\frac{\dot{s}}{2\dot{s}_0} \exp \left(\frac{\Psi}{a} \right) \right], \quad (1)$$

$$\frac{d\Psi}{dt} = -\frac{\dot{s}}{L} (\Psi - \Psi_{SS}), \quad (2)$$

$$\Psi_{SS} = a \log \left[\frac{2\dot{s}_0}{\dot{s}} \sinh \left(\frac{f_{SS}}{a} \right) \right], \quad (3)$$

$$f_{SS} = f_w + \frac{f_{LV} - f_w}{\left(1 + \left(\frac{\dot{s}}{\dot{s}_w} \right)^8 \right)^{\frac{1}{8}}}, \quad (4)$$

$$f_{LV} = f_0 - (b - a) \log \left(\frac{\dot{s}}{\dot{s}_0} \right). \quad (5)$$

Eq. 1 gives the frictional resistance τ , which depends on the normal stress σ_n , the direct effect parameter a , the slip rate \dot{s} , the reference slip rate \dot{s}_0 , and the state variable Ψ . Eq. 1 is regularized to avoid divergence at $\dot{s} = 0$ (Rice & Ben-Zion, 1996; Lapusta et al., 2000). Eq. 2 is an ordinary differential equation describing the evolution of the state variable Ψ . L is the characteristic slip distance, and Ψ_{SS} is the steady-state value of the state variable, which is given by Eq. 3. Eq. 4 computes the steady-state friction f_{SS} , which depends on

the weakened friction coefficient f_w , the slip rate \dot{s} , the weakening slip rate \dot{s}_w , and the low-velocity steady-state friction coefficient f_{LV} . At $\dot{s} > \dot{s}_w$, f_{SS} drops rapidly from f_{LV} to f_w , with the $1/\dot{s}$ behavior resembling thermal weakening processes at coseismic slip rates such as flash-heating (Rice, 2006; Beeler et al., 2008). Eq. 5 calculates the low-velocity steady-state friction f_{LV} from the steady-state friction coefficient, the slip rate \dot{s} and the reference slip rate \dot{s}_0 , and the difference between the state evolution parameter b and the direct effect parameter a , which determines if the frictional behavior is velocity-weakening ($b - a > 0$) or velocity-strengthening ($b - a < 0$). We set the reference slip rate to 10^{-6} m/s, a common choice in dynamic rupture simulations (Harris et al., 2018). We note that the initial slip rate \dot{s}_{init} is a dynamic inversion parameter (Table 1) and differs from the reference slip rate \dot{s}_0 .

Text S2: Bayesian inversion method

We use a Bayesian framework to formulate the inverse problem (Tarantola, 2005; Gallovič et al., 2019), where we sample the posterior probability density function (PDF) $p(\mathbf{m}|\mathbf{d})$ to gain information on the likelihood of a set of dynamic model parameters \mathbf{m} given the observed seismic waveform and geodetic displacement data \mathbf{d} :

$$p(\mathbf{m}|\mathbf{d}) = \frac{p(\mathbf{m})p(\mathbf{d}|\mathbf{m})}{p(\mathbf{d})}. \quad (6)$$

We prescribe the prior PDF $p(\mathbf{m})$ as a uniform distribution between the pre-selected dynamic parameter bounds (see Table 1). The Bayesian evidence $p(\mathbf{d})$ normalizes the

posterior PDF. The PDF of the data given a model $p(\mathbf{d}|\mathbf{m})$ is based on a least-square misfit between the synthetics $\mathbf{s}_i(\mathbf{m})$ and the observed data \mathbf{d}_i :

$$p(\mathbf{d}|\mathbf{m}) = \exp\left(-\frac{1}{2} \sum_{i=1}^N \frac{\|\mathbf{s}_i(\mathbf{m}) - \mathbf{d}_i\|^2}{\sigma_i^2}\right). \quad (7)$$

N is the total number of stations, and σ_i are the standard deviations, which are assumed to be uncorrelated and represent the combined uncertainty of the model and data errors.

We explore the model space with the Parallel Tempering Markov chain Monte Carlo (MCMC) method (Sambridge, 2013). A Markov chain consists of a sequence of models where the parameters of the next model depend only on the previous model. Model parameters are randomly perturbed during each step, with the step size inferred from a log-normal distribution. The new model is checked against the parameter bounds and is either directly discarded if the bounds are violated or the algorithm runs the forward simulation and calculates the misfit. Proposed models with a smaller misfit are always accepted. If the new misfit is larger, the proposed model is accepted with a probability given by the Metropolis-Hastings rule (Metropolis et al., 1953). The Parallel Tempering approach explores the model space using several parallel Markov Chains, each with a temperature parameter T assigned. These Markov chains sample a modified posterior PDF:

$$p(\mathbf{m}|\mathbf{d}, T) = c_1 p(\mathbf{m}) \exp\left(-\frac{1}{T} \frac{1}{2} \sum_{i=1}^N \frac{\|\mathbf{s}_i(\mathbf{m}) - \mathbf{d}_i\|^2}{\sigma_i^2}\right). \quad (8)$$

Markov Chains with higher T have smoother PDFs, which increases the probability of accepting the next step and facilitates the escape from local minima. c_1 normalizes the PDF.

The Parallel Tempering algorithm proposes a temperature swap between the chains after each iteration. The probability of each swap is based on the Metropolis-Hastings rule. Final samples of the posterior PDF are drawn from the chains where $T = 1$. Sambridge (2013) demonstrated that the Parallel Tempering method is well-suited for non-linear problems with complicated PDFs and may converge more than 10 times faster than a non-tempered MCMC approach. In our specific case, each MPI rank hosts 8 Markov Chains, two with $T = 1$, and the other six temperatures are randomly drawn from a log-uniform distribution between 1 and 100, concentrating more values close to 1.

Text S3: Crack- and pulse-like rupture

The ratio of rise time to rupture duration is commonly used to distinguish between pulse-like and crack-like rupture (Heaton, 1990). A ratio close to 1 indicates a crack-like rupture, while a ratio $\ll 1$ suggests a pulse-like rupture. In this study, we refer to a rupture as pulse-like when the ratio is < 0.1 , which corresponds to a rise time of < 1.4 s for the PM, assuming a rupture duration of 14 s. This criterion defines the rupture in the hypocentral region as pulse-like. However, simply selecting a threshold for crack-like rupture is not straightforward, as the ratio also depends on the local initiation time of the rupture episode. For instance, the center of the northwestern asperity starts to rupture at 10 s

simulation time but still reaches rise times > 3 s and only stops when a healing front from the northwestern coseismic rupture edge arrives, which indicates a crack-like rupture.

Movie S1. Coseismic slip rate evolution of the preferred dynamic rupture and afterslip model. The black contour shows the coseismic rupture extent and the star marks the hypocenter.

Movie S2. 90-day postseismic slip rate evolution of the preferred joint dynamic rupture and afterslip model. Light blue dots show aftershocks during the latest 20% of the time since the mainshock and grey dots show the remaining aftershocks since the mainshock. The black line shows the coseismic rupture extent and the star marks the hypocenter.

2004 Parkfield dynamic source inversion approach

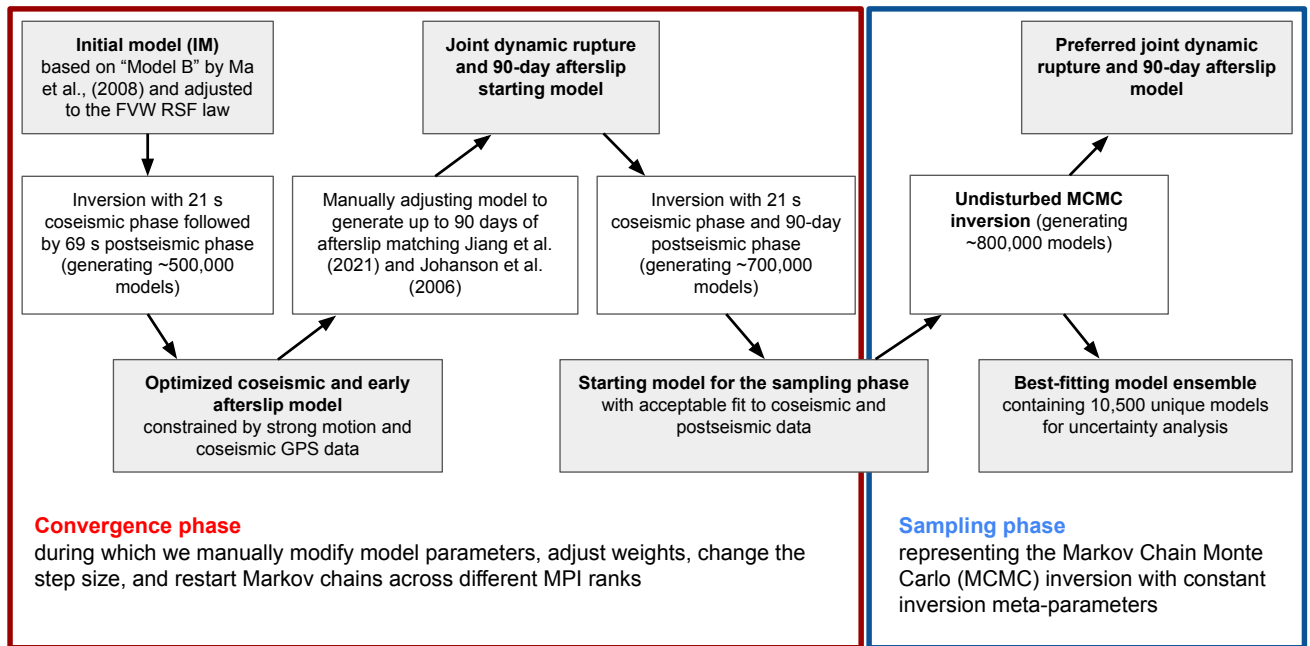


Figure S1. Outline of the dynamic source inversion approach. The inversion is divided into two main phases: the convergence phase (red box) and the sampling phase (blue box). The sampling phase represents the Markov Chain Monte Carlo (MCMC) inversion in a strict sense, i.e. without any further alternation of model parameters, data weights, step size, etc. (see main text Section 2.4). FVW = fast-velocity weakening, RSF = rate-and-state friction.

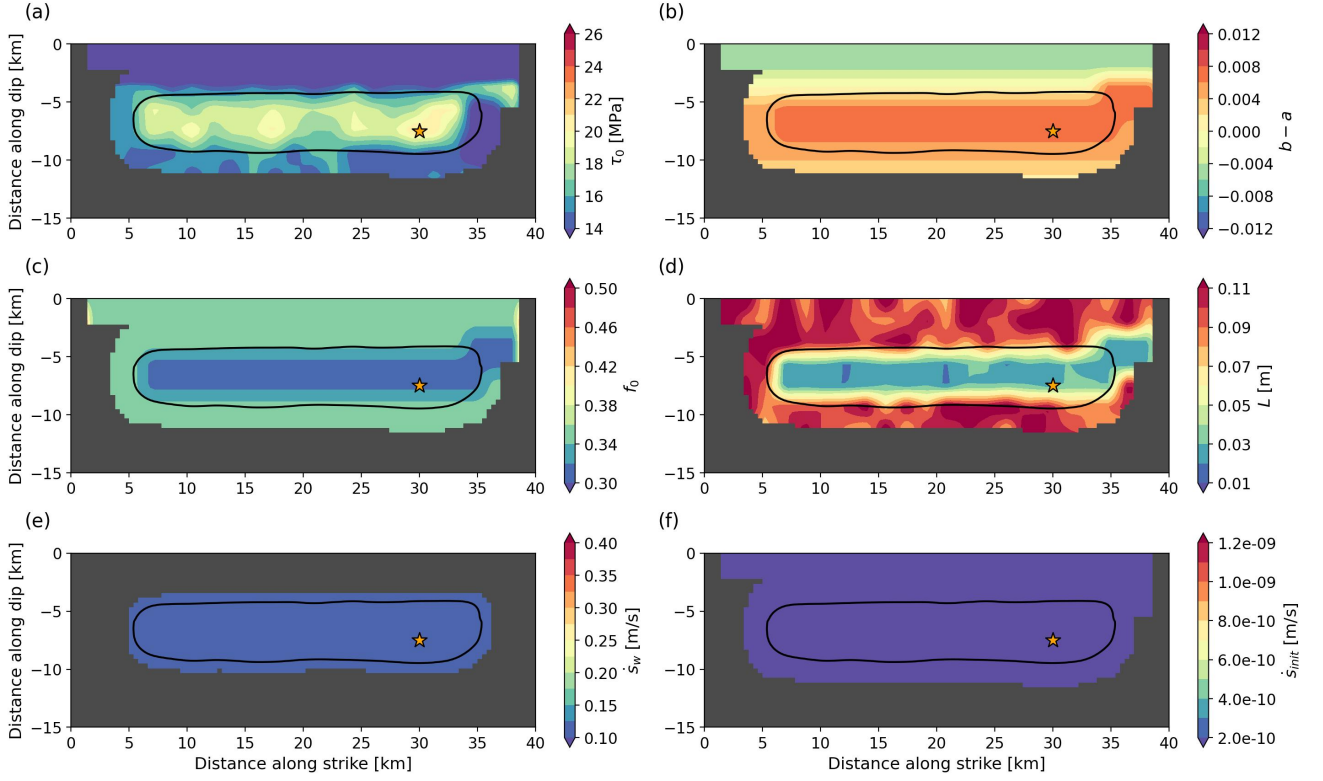


Figure S2. Dynamic parameters of the initial dynamic rupture model based on "Model B" of Ma et al. (2008). The parameters are bilinearly interpolated from the model grid (Fig. 1d) onto the grid of the quasi-dynamic solver, which has a 400 m spacing. We consider parameters to be unconstrained in all areas of the fault where the overall fault slip (coseismic + postseismic) does not exceed 10 cm within a radius of 1.2 km. We do not show dynamic parameters on these unconstrained fault grid points. The black line indicates the extent of the coseismic rupture, and the star marks the hypocenter of the mainshock. (a) Prestress τ_0 . (b) Difference between the state evolution and the direct effect parameter, $b - a$. (c) Reference friction coefficient f_0 . (d) Characteristic slip distance L . (e) Weakening slip rate \dot{s}_w . (f) Initial slip rate \dot{s}_{init} .

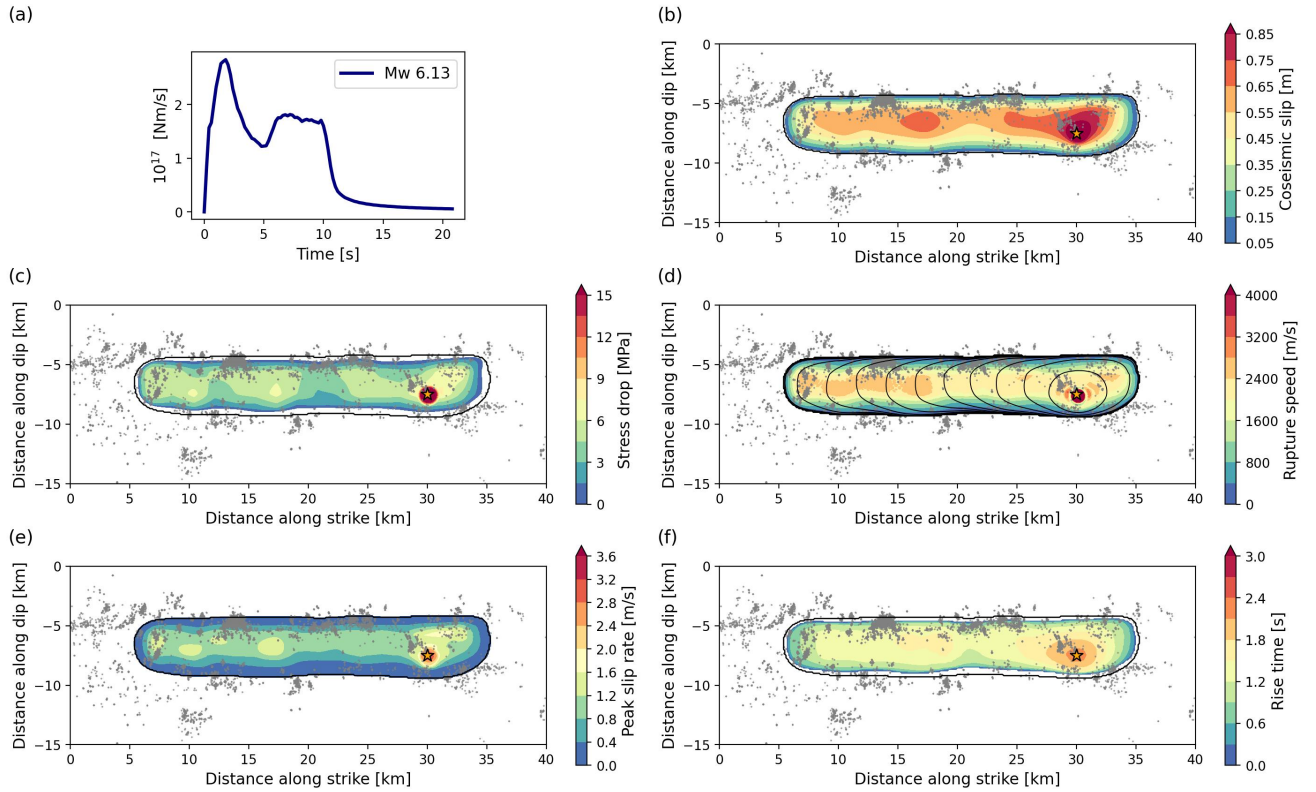


Figure S3. Coseismic dynamic rupture parameters of the initial dynamic rupture model based on "Model B" of Ma et al. (2008). Grey dots show 90-day aftershock locations (Neves et al., 2022) projected on the planar fault plane, the black contour indicates the coseismic rupture extent, and the star marks the hypocenter. (a) Moment release rate and moment magnitude. (b) Coseismic slip. (c) Stress drop. (d) Local rupture speed and rupture front contours every 1 s. (e) Peak slip rate. (f) Rise time.

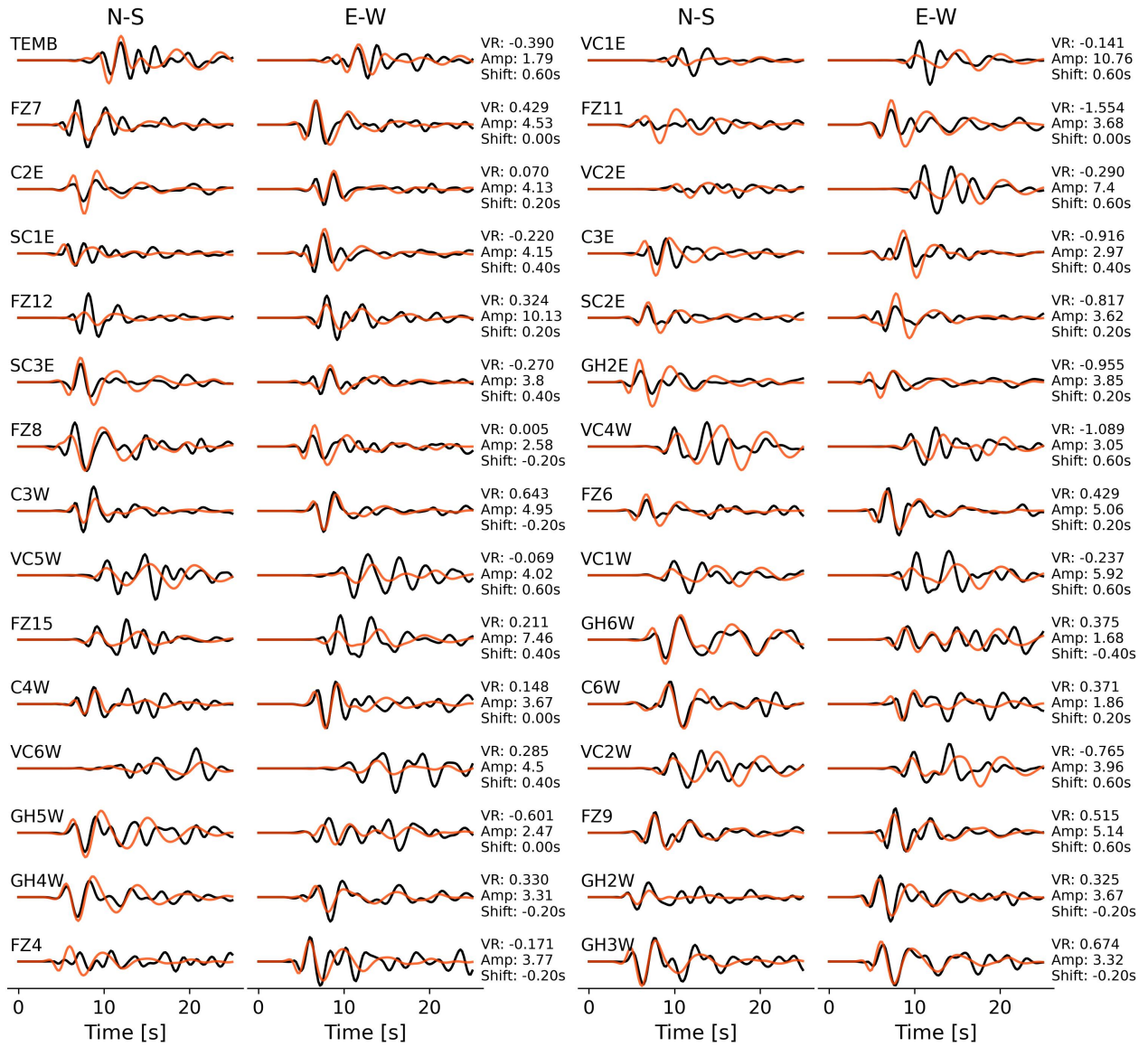


Figure S4. Observed (black) and synthetic (orange) seismic velocity waveforms from the initial dynamic rupture model based on "Model B" of Ma et al. (2008), bandpass filtered between 0.16–0.5 Hz at the 30 stations used to constrain the inversion. Each waveform (synthetic and observed) is normalized by the respective station's maximum amplitude (Amp, in cm/s, either synthetic or observed maximum). The observed waveforms at each station are cross-correlated and time-shifted relative to the synthetics to maximize the variance reduction (VR) and to account for unmodeled effects of topography and the 3D velocity structure.

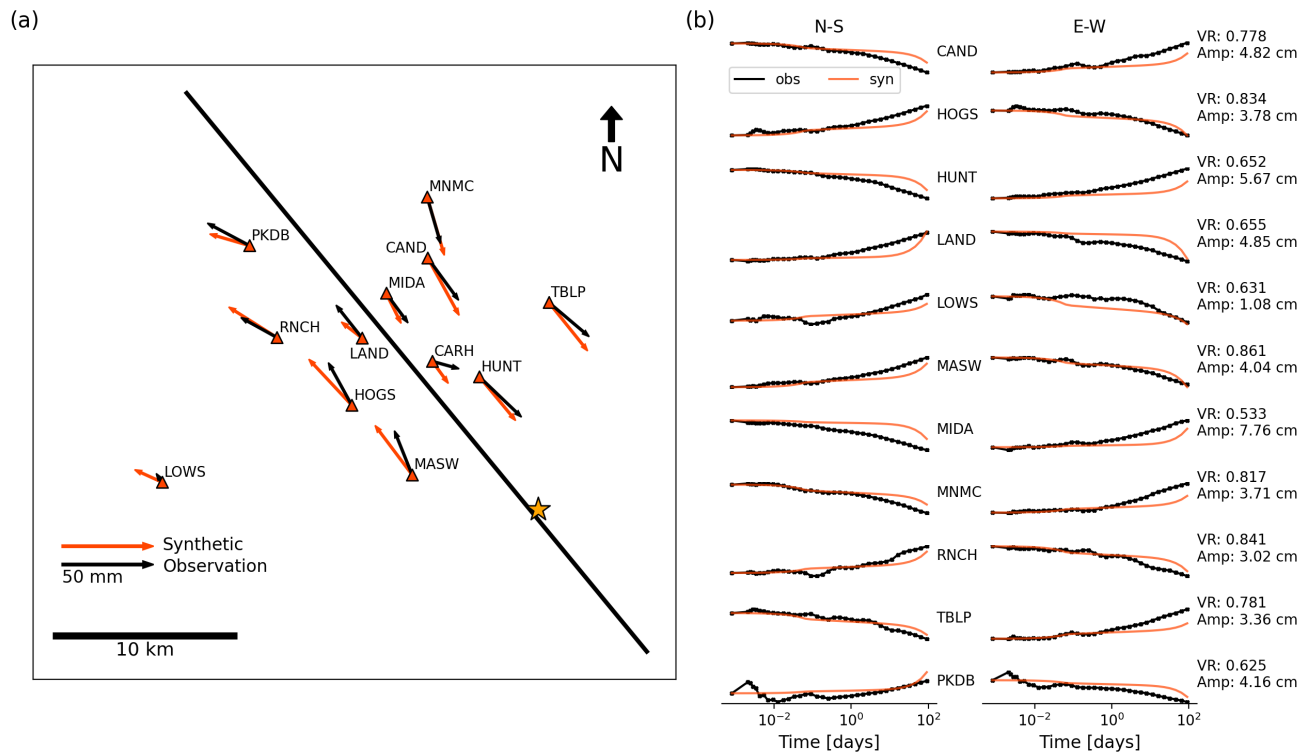


Figure S5. (a) Coseismic horizontal static displacements at 12 GPS stations. Black and orange arrows show observed (Jiang et al., 2021) and synthetic displacements from the initial dynamic rupture model based on "Model B" of Ma et al. (2008), respectively. The black line indicates the fault trace, and the star marks the epicenter. Both synthetic and observed coseismic displacements are given at 90 s after the rupture onset. (b) Postseismic evolution of the normalized displacements at 11 GPS stations (excluding station CARH) during the first 90 days following the earthquake. Black curves show observations (Jiang et al., 2021), and orange curves show the synthetics of our initial model. The time scale is logarithmic. For each station, we annotate its variance reduction inferred after removing the coseismic displacement and its maximum amplitude.

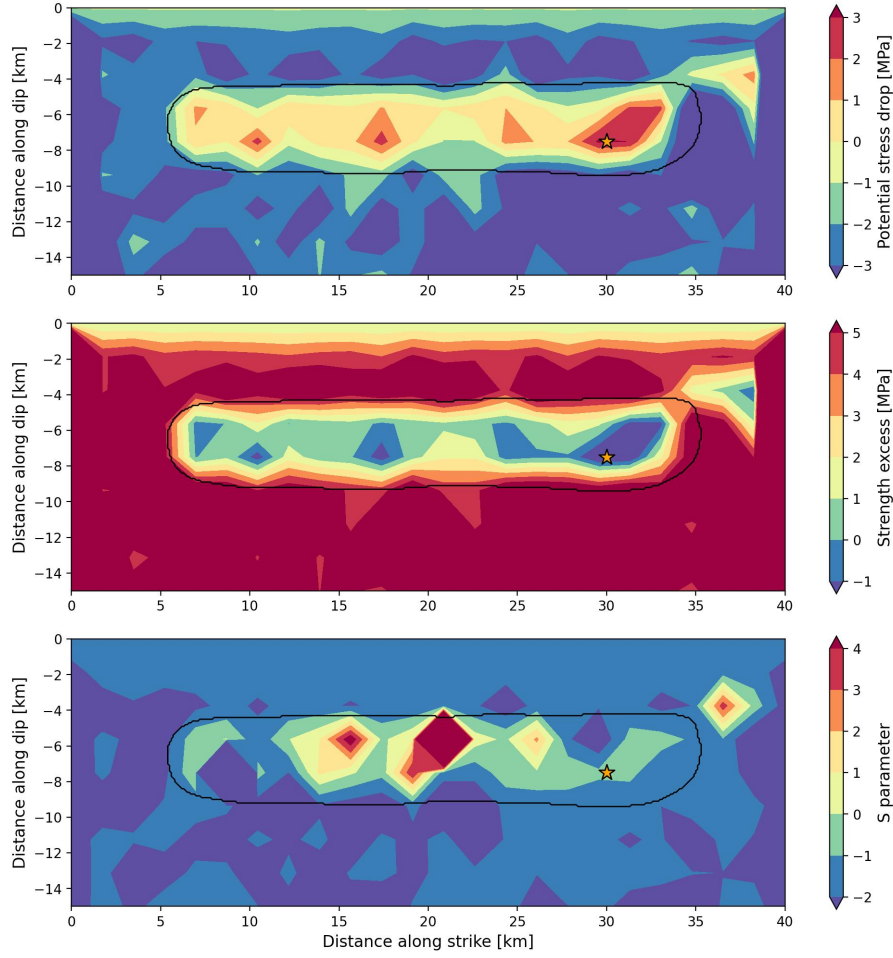


Figure S6. Derived quantities from the dynamic parameters of the initial dynamic rupture model based on "Model B" of Ma et al. (2008). The black contour indicates the coseismic rupture extent, and the star marks the hypocenter. (a) Potential stress drop ($\tau_0 - f_w \sigma_n$). (b) Strength excess ($f_0 \sigma_n - \tau_0$). (c) S parameter ($\frac{f_0 \sigma_n - \tau_0}{\tau_0 - f_w \sigma_n}$). In the rate-and-state framework, these parameters represent only approximations because the minimum and maximum friction coefficients are dynamically determined.

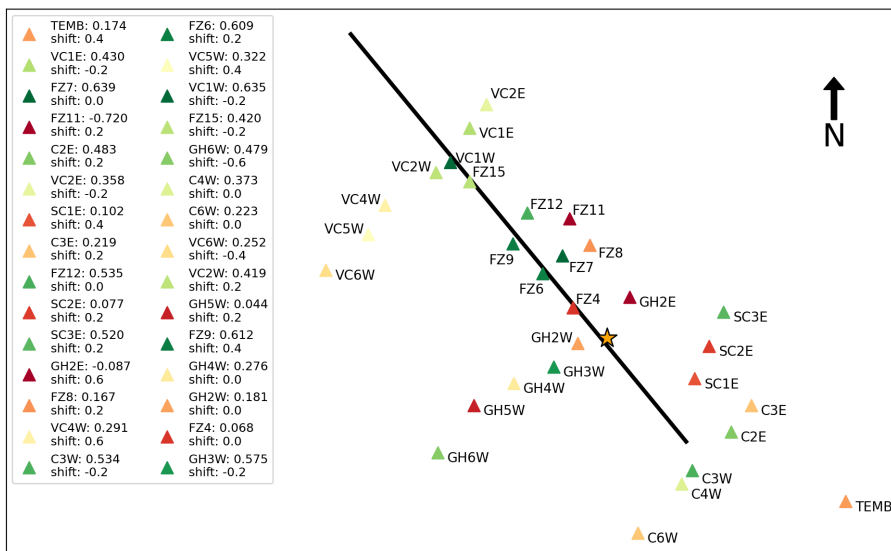


Figure S7. Stations used for constraining the inversion colored by their seismic variance reductions obtained from the preferred joint dynamic rupture and afterslip model. The star marks the epicenter and the black line shows the fault trace of our model’s planar fault.

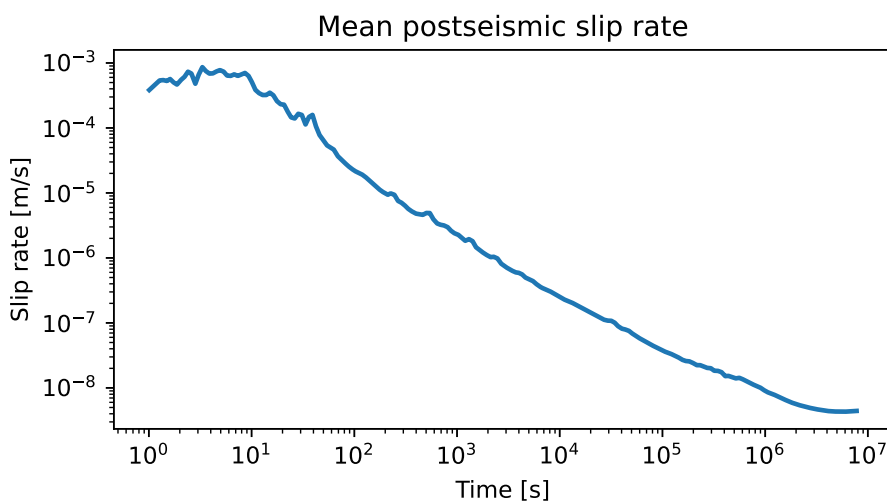


Figure S8. Mean postseismic slip rate of the PM calculated across the entire fault plane.

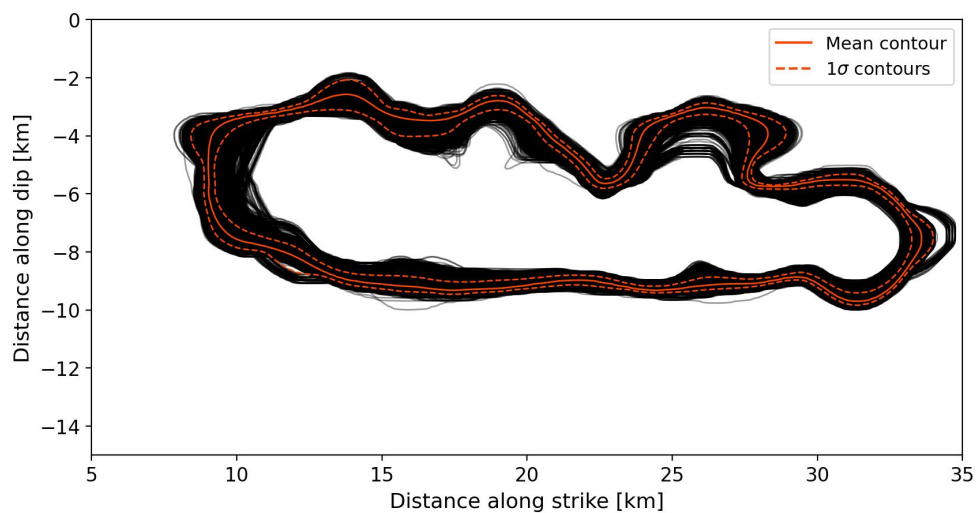


Figure S9. Dynamic rupture extent contours of the 10500 models of the best-fitting ensemble. Orange and dashed orange lines show the mean rupture edge and one standard deviation in both directions, respectively.

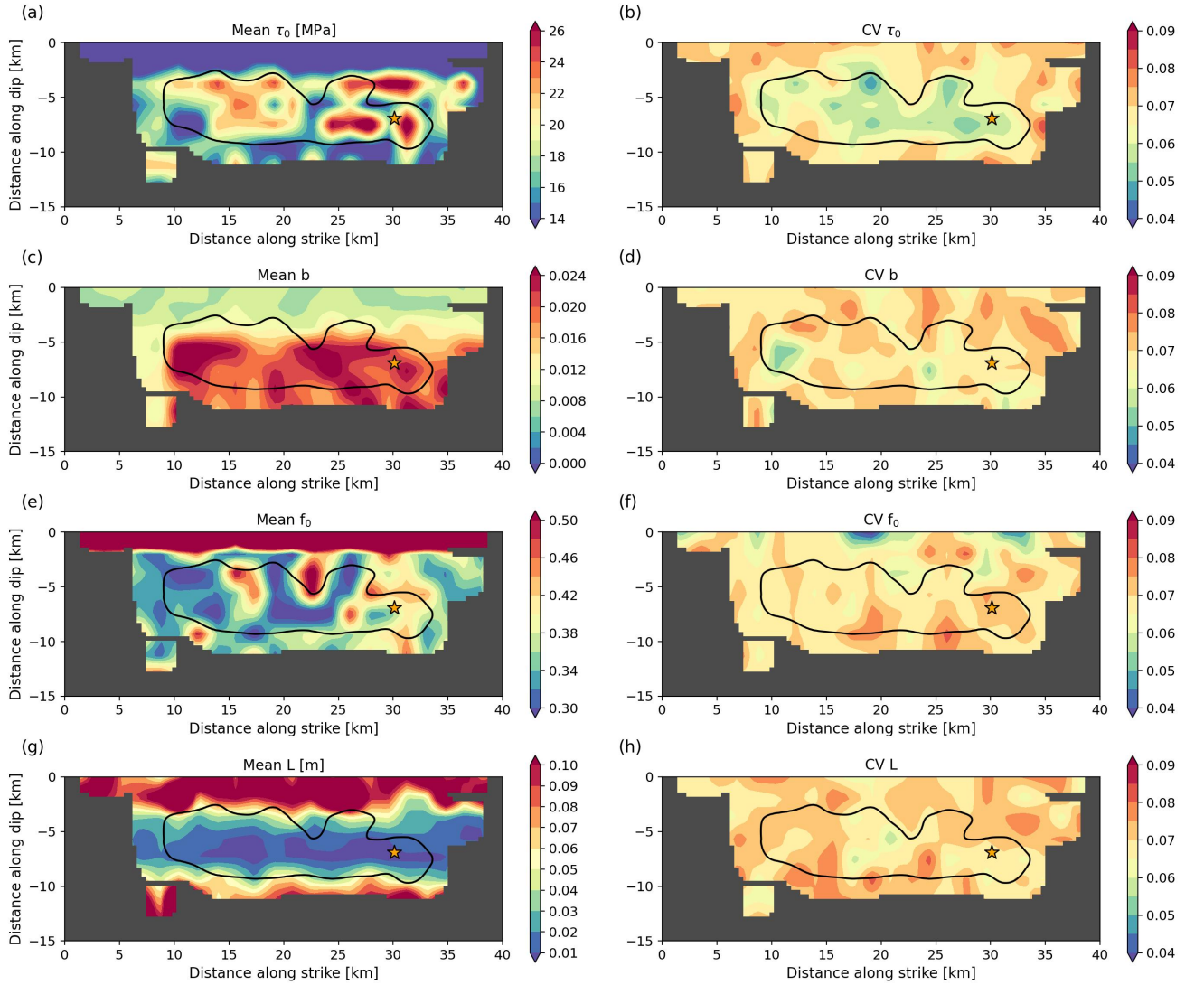


Figure S10. Mean distributions of the best-fitting model ensemble's (a) prestress τ_0 , (c) $b - a$, (e) reference friction coefficient f_0 , (g) characteristic slip distance L , and their corresponding coefficients of variation CV (b,d,f,h). The model ensemble contains 10500 models. We mask areas where the sum of coseismic and postseismic slip does not exceed 10 cm within 1.2 km, which we consider unconstrained.

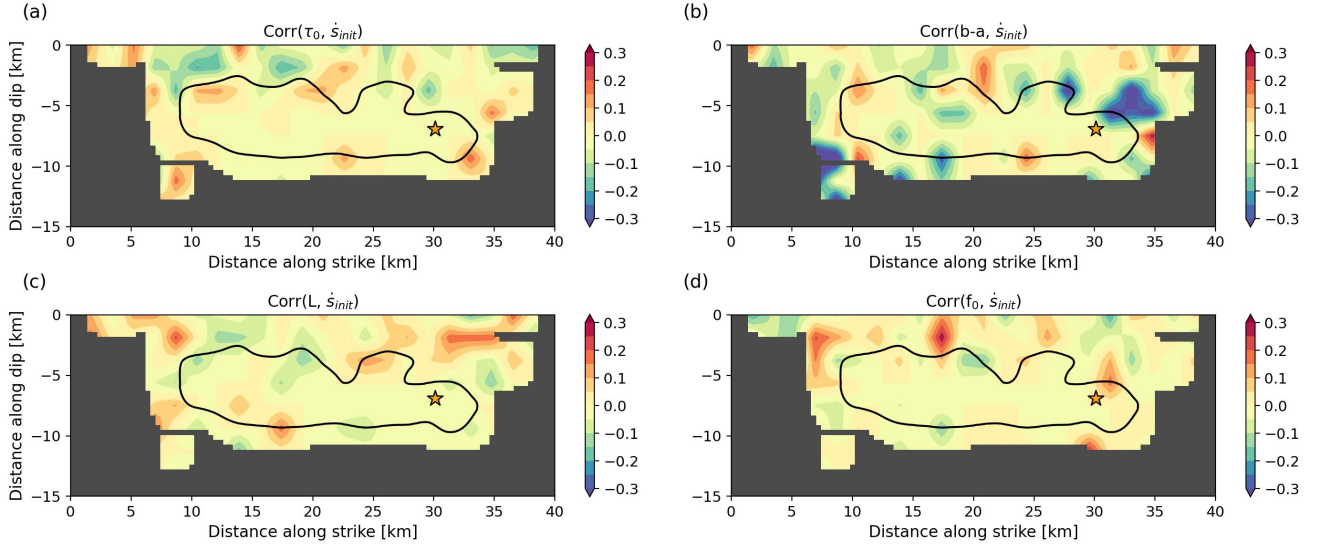


Figure S11. Spatial distributions of ensemble correlation coefficients of dynamic parameter pairs (a) τ_0 and \dot{s}_{init} , (b) $b - a$ and \dot{s}_{init} , (c) L and \dot{s}_{init} , (d) f_0 and \dot{s}_{init} . The black contour indicates the extent of the coseismic rupture, and the star marks the hypocenter. We mask areas where the sum of coseismic and postseismic slip does not exceed 10 cm within an area of a radius of 1.2 km, which we consider unconstrained. \dot{s}_{init} is set constant in velocity-weakening regions, which strongly affects correlations within the coseismic rupture area.

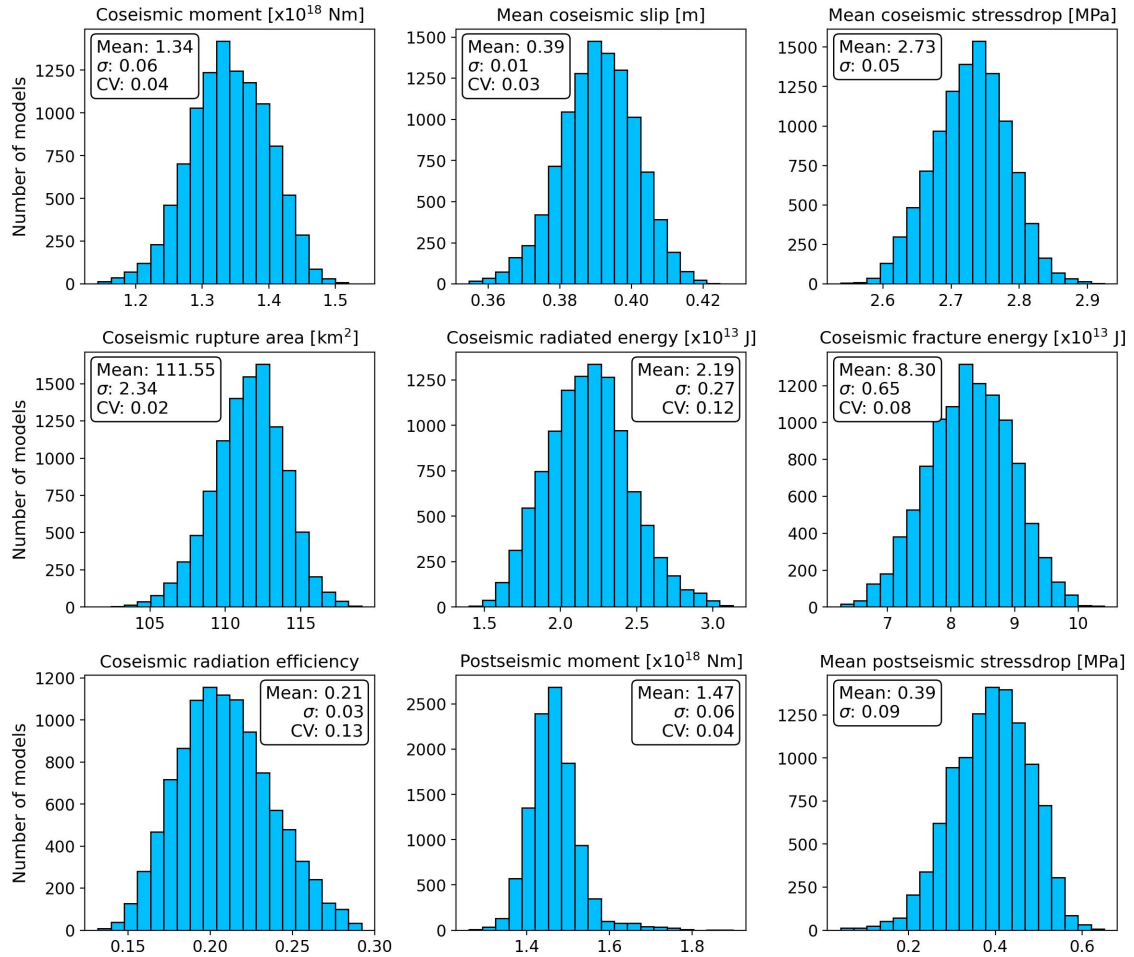


Figure S12. Histograms of various coseismic and postseismic rupture parameters of the best-fitting model ensemble containing 10500 unique joint dynamic rupture and afterslip models. Legends of each subplot show mean values, standard deviations σ , and coefficients of variation CV (ratio of the standard deviation to the mean) for quantities with an absolute zero.

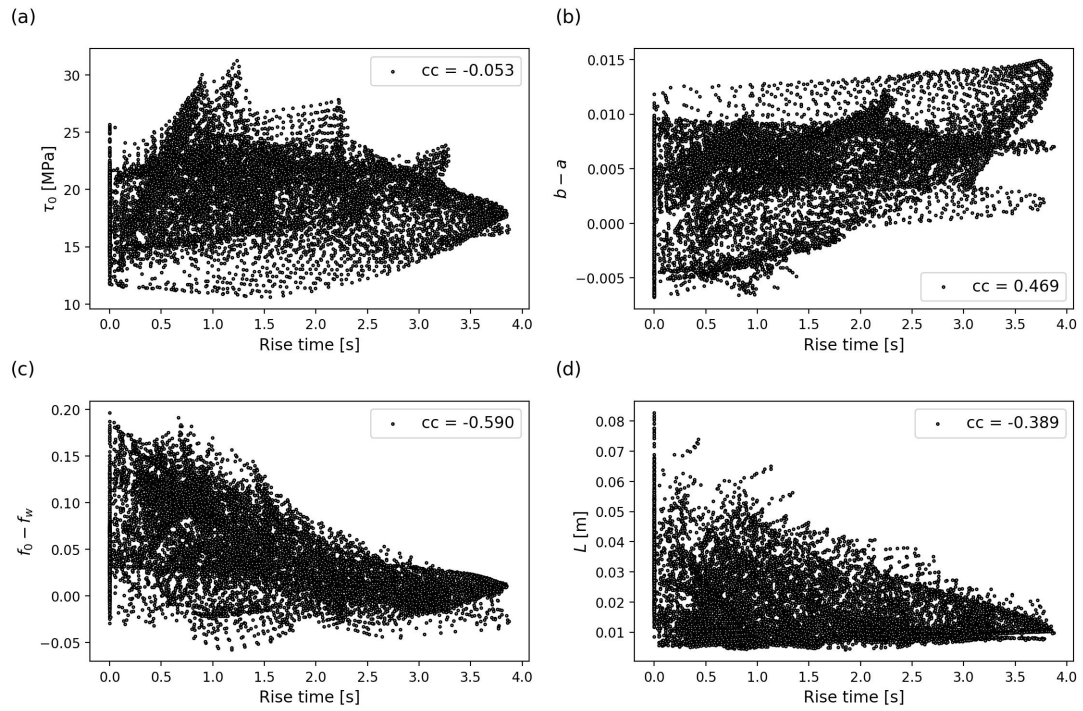


Figure S13. Rise times of each grid point of the preferred joint dynamic rupture and afterslip model plotted against (a) τ_0 , (b) $b - a$, (c), reference friction drop $f_0 - f_w$, (d) L . Subplot legends show correlation coefficients between both variables.

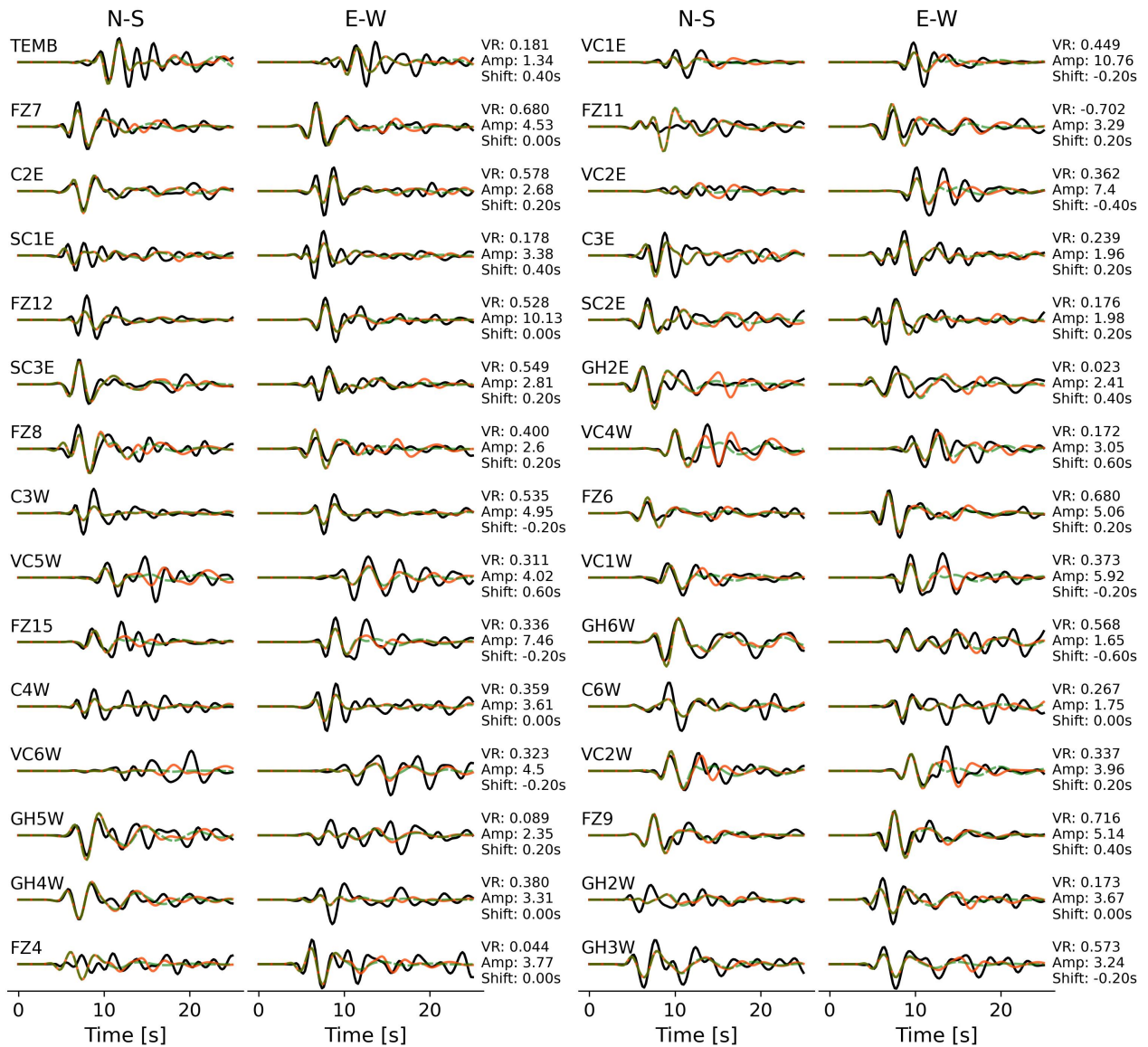


Figure S14. Observed (black) and synthetic (dashed green) velocity waveforms from a **5 s** version of the preferred joint dynamic rupture and afterslip model (including only the initial pulse-like rupture phase) filtered between 0.16 and 0.5 Hz at the 30 stations used to constrain the inversion. The reference model's waveforms (21 s simulation duration) are shown in orange. Each waveform is normalized by the respective station's maximum amplitude (Amp in cm/s). The variance reductions (VR) of the 5 s version are annotated. The observed waveforms at each station are shifted relative to the reference synthetics to account for the effects of topography and the 3D velocity structure by maximizing the VR.

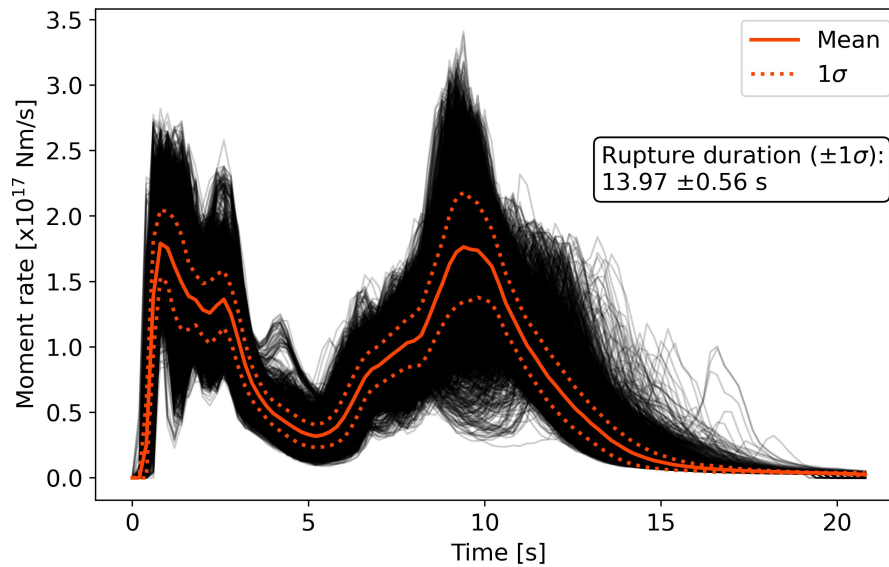


Figure S15. Coseismic moment rate functions of the best-fitting model ensemble, shown with their associated mean $\pm 1\sigma$. The model ensemble consists of 10,500 models. Rupture durations are defined as the time intervals during which the moment rates exceed 10% of the lower bound of the standard deviation (mean - 1σ) at its maximum.

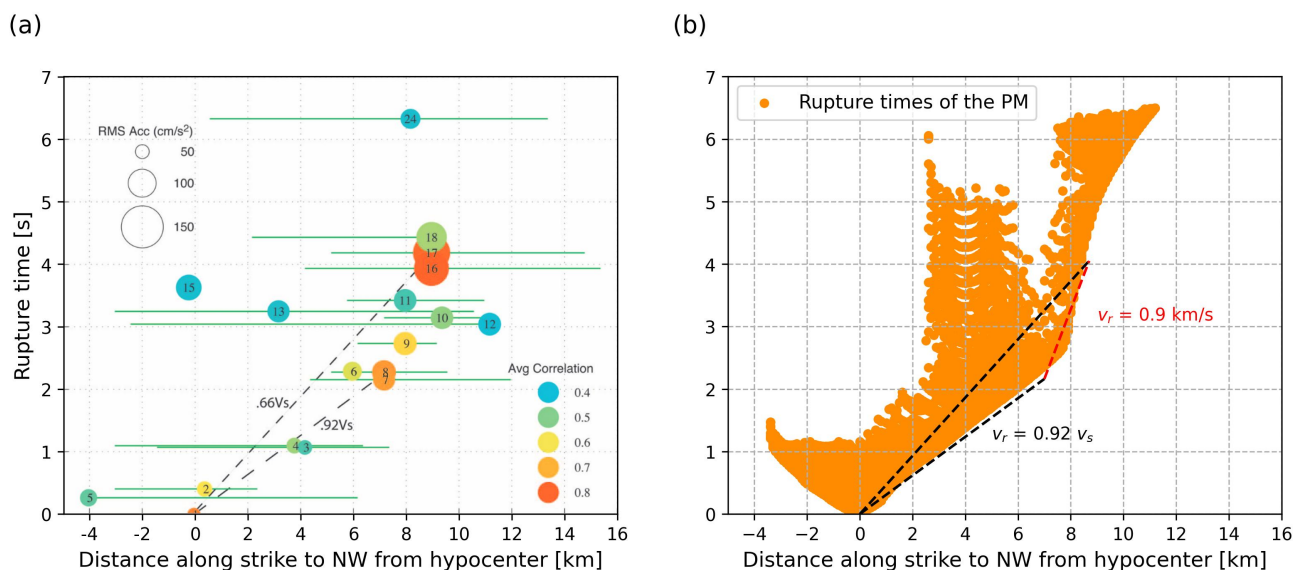


Figure S16. (a) Fig. 10 from Fletcher et al. (2006) showing source locations of the 2004 Parkfield rupture, tracked with a short baseline array, plotted as distance along strike versus rupture time. Dashed lines show the rupture velocities as a fraction of $v_s = 3.52$ km/s. Colors indicate average correlations. The along-strike direction is flipped compared to other figures in this study. (b) Rupture times of slipping grid points in our PM plotted against distance from the hypocenter, tracking the rupture front during the first 6.5 s. Dashed black lines represent the same rupture velocities as in (a). The dashed red line shows the mean rupture velocity between the best-correlated sources 7,8 and 16,17 in (a). Locations of the best-correlated sources identified by Fletcher et al. (2006) agree well with the rupture front in the PM.

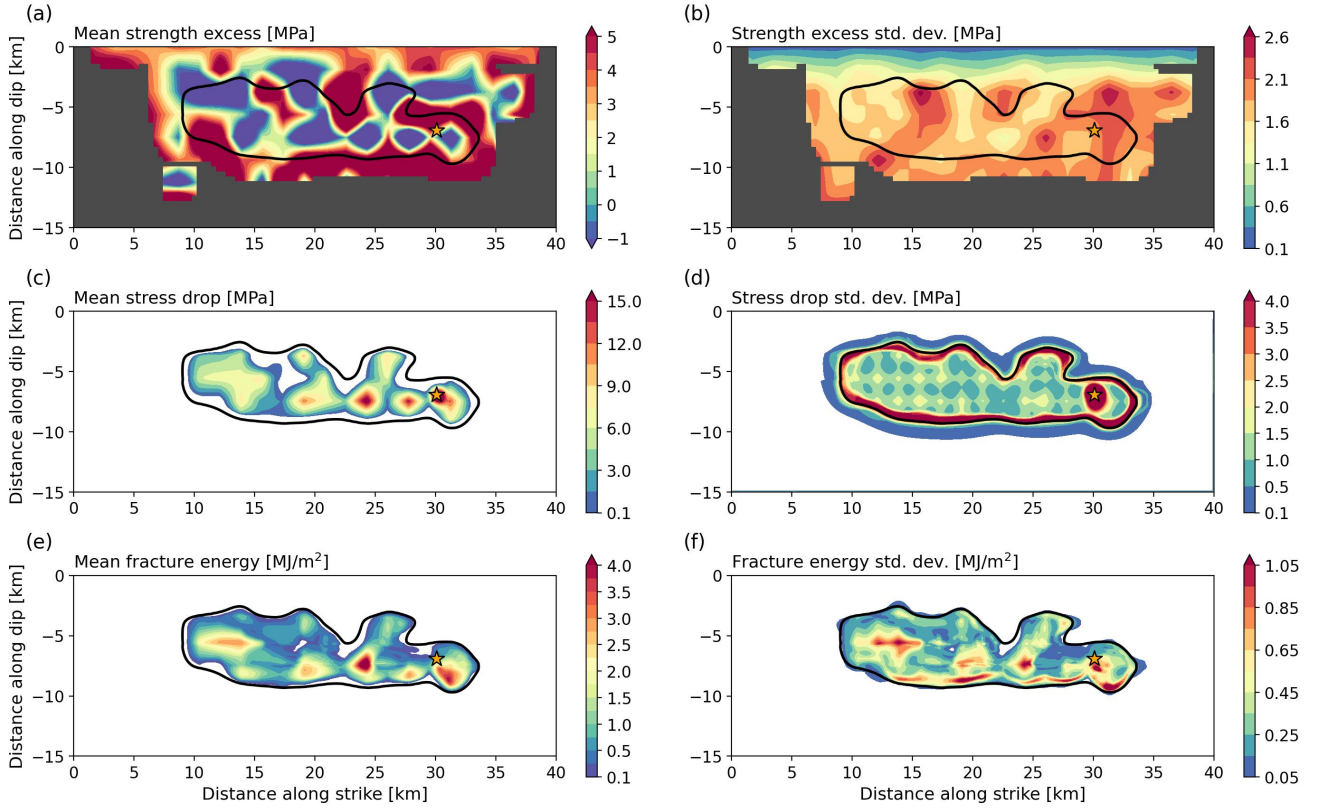


Figure S17. Means of the best-fitting model ensemble's (a) initial strength excess ($f_0\sigma_n - \tau_0$), (c) coseismic stress drop (e) coseismic fracture energy distributions, and the corresponding standard deviations (b,d,f). The model ensemble contains 10500 models. We only show the strength excess where coseismic and postseismic slip combined exceed 10 cm somewhere within a radius of 1.2 km, which we consider as constrained by the inversion.

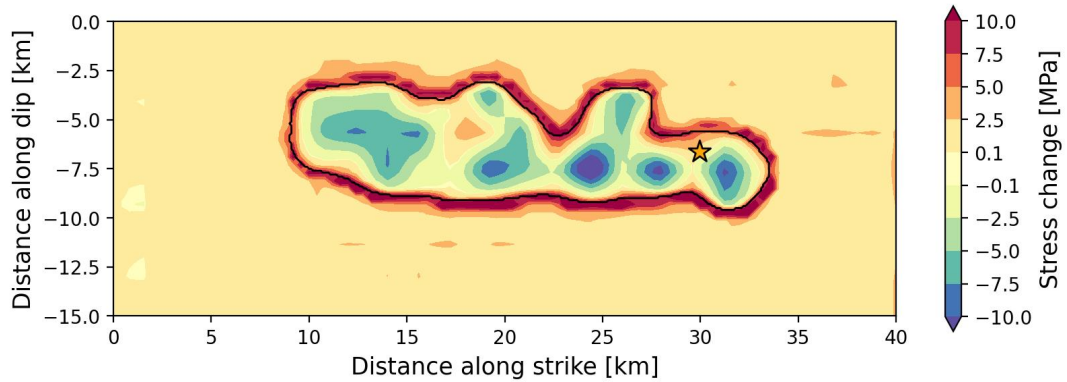


Figure S18. Coseismic stress change of the preferred joint dynamic rupture and afterslip model. The black line indicates the coseismic rupture extent and the star marks the hypocenter.

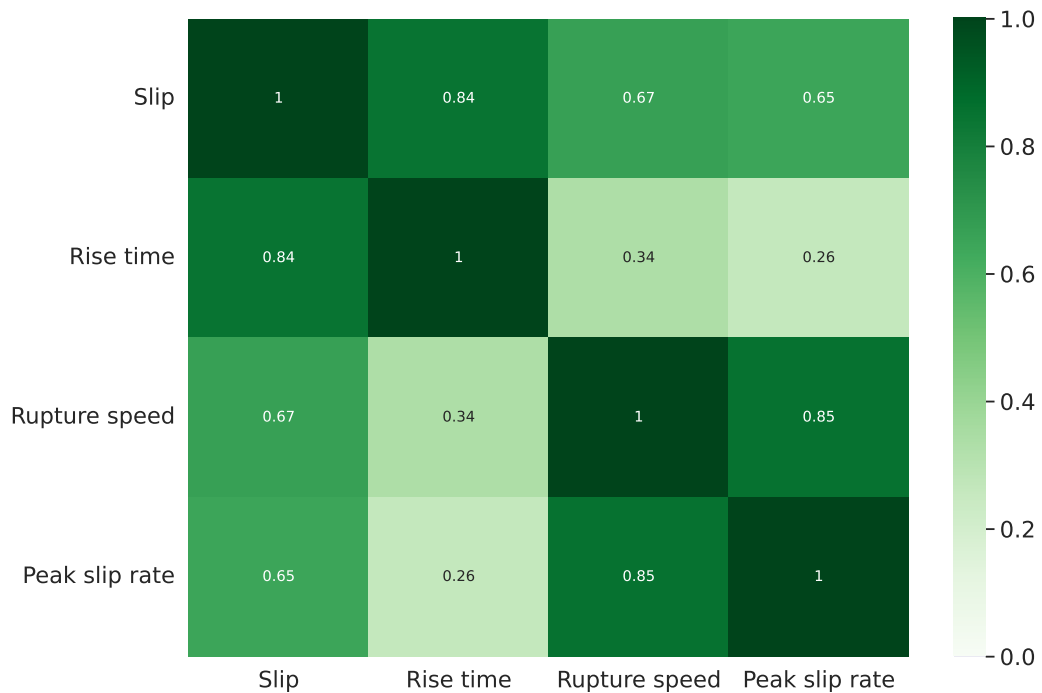


Figure S19. Correlation matrix of kinematic parameters of the 10,500 models of the best fitting ensemble, following Schmedes et al. (2010). We correlate dynamic parameters only on those points of the fault where the ensemble mean peak slip rate exceeds 0.1 m/s and exclude the nucleation region. The rupture speed is normalized by the fault-local S-wave velocity.

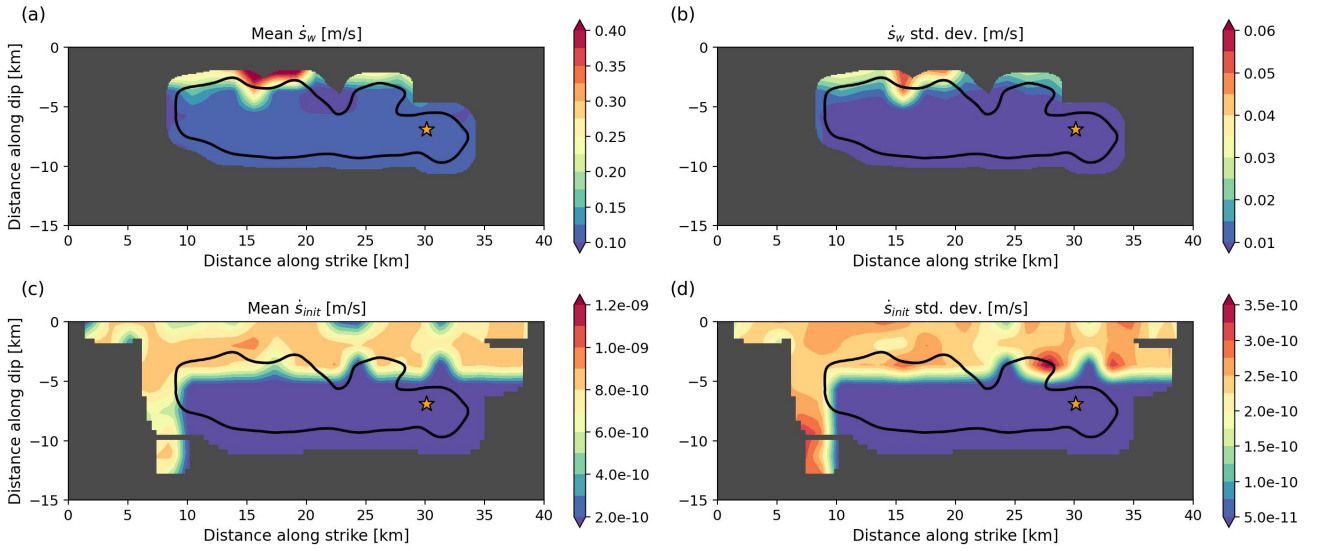


Figure S20. Mean distributions of the best-fitting model ensemble's (a) weakening slip rate \dot{s}_w , (c) initial slip rate \dot{s}_{init} , and the corresponding standard deviations (b,d). The model ensemble contains 10500 models. We hide areas where the sum of coseismic and postseismic slip does not exceed 10 cm within 1.2 km, which we consider unconstrained. For the weakening slip rate \dot{s}_w , we only consider coseismic slip.

Table S1. 1D velocity profiles on the southwest and northeast side of the fault (Custódio et al., 2005) used to calculate the Green's functions. The dynamic rupture solver uses the average velocity profile. Q values are based on v_s : $Q_s = 0.1 v_s$ (in m/s) and $Q_p = 1.5 Q_s$ (Olsen et al., 2003).

Lower extent [km]	v_p [m/s]	v_s [m/s]	Density [kg/m ³]	Q_p	Q_s
southwest					
1.0	2000	1100	2000	165	110
2.0	3500	2000	2300	300	200
3.0	4500	2500	2300	375	250
3.5	5200	3000	2500	450	300
5.8	5700	3200	2700	480	320
14.1	6200	3600	2700	540	360
17.1	6800	3600	2800	540	360
20.4	6800	4300	2800	645	430
∞	7300	4300	2800	645	430
northeast					
1.0	2000	1100	2000	165	110
1.8	3500	2200	2300	330	220
2.1	4200	2800	2300	420	280
3.4	4800	2700	2300	405	270
3.9	5200	2800	2300	420	280
8.3	5300	3200	2700	480	320
12.7	5700	3700	2800	555	370
17.5	6500	3800	2800	570	380
20.3	6700	4300	2800	645	430
∞	7300	4300	2800	645	430
average					
1.0	2000	1100	2000	165	110
2.0	3500	2100	2300	315	210
3.5	4400	2700	2300	405	270
5.8	5500	3000	2500	450	300
12.7	5800	3600	2700	540	360
17.1	6500	3800	2800	570	380
20.3	6800	4300	2800	645	430
∞	7300	4300	2800	645	430

Table S2. Step size ranges of the model parameter perturbations during the inversion. The parameter perturbations are drawn from a log-normal distribution and the step size represents its relative standard deviation. The step size is successively reduced to keep the model acceptance rate reasonable.

Label	Parameters	Log-normal step size (in %)
τ_0	Shear prestress	0.3–2.0
b	state evolution parameter	0.3–2.0
f_0	Reference friction coefficient at $\dot{s}_0 = 10^{-6}$	0.3–2.0
L	Characteristic slip distance	0.3–2.0
\dot{s}_w	Weakening slip rate	0.3–2.0
\dot{s}_{init}	Initial slip rate	2.0
h_x	Along-strike position of nucleation patch	0.3–2.0
h_z	Along-dip position of nucleation patch	0.3–2.0
r_{nuc}	Radius of the nucleation patch	0.3–2.0
σ_{nuc}	Stress increase within the nucleation patch	0.3–2.0

References

- Ampuero, J.-P., & Ben-Zion, Y. (2008). Cracks, pulses and macroscopic asymmetry of dynamic rupture on a bimaterial interface with velocity-weakening friction. *Geophysical Journal International*, 173.
- Beeler, N. M., Tullis, T. E., & Goldsby, D. L. (2008). Constitutive relationships and physical basis of fault strength due to flash heating. *Journal of Geophysical Research: Solid Earth*, 113.
- Custódio, S., Liu, P., & Archuleta, R. J. (2005). The 2004 Mw6.0 Parkfield, California, earthquake: Inversion of near-source ground motion using multiple data sets. *Geophysical Research Letters*, 32.
- Dunham, E. M., Belanger, D., Cong, L., & Kozdon, J. E. (2011). Earthquake Ruptures with Strongly Rate-Weakening Friction and Off-Fault Plasticity, Part 1: Planar Faults. *Bulletin of the Seismological Society of America*, 101.
- Fletcher, J. B., Spudich, P., & Baker, L. M. (2006). Rupture Propagation of the 2004 Parkfield, California, Earthquake from Observations at the UPSAR. *Bulletin of the Seismological Society of America*, 96.
- Gallovič, F., Valentová, L., Ampuero, J.-P., & Gabriel, A.-A. (2019). Bayesian Dynamic Finite-Fault Inversion: 1. Method and Synthetic Test. *Journal of Geophysical Research: Solid Earth*, 124.
- Harris, R. A., Barall, M., Aagaard, B., Ma, S., Roten, D., Olsen, K., . . . Dalguer, L. (2018). A Suite of Exercises for Verifying Dynamic Earthquake Rupture Codes. *Seismological Research Letters*, 89.
- Heaton, T. H. (1990). Evidence for and implications of self-healing pulses of slip in earthquake

- rupture. *Physics of the Earth and Planetary Interiors*, 64.
- Jiang, J., Bock, Y., & Klein, E. (2021). Coevolving early afterslip and aftershock signatures of a San Andreas fault rupture. *Science Advances*, 7.
- Lapusta, N., Rice, J. R., Ben-Zion, Y., & Zheng, G. (2000). Elastodynamic analysis for slow tectonic loading with spontaneous rupture episodes on faults with rate- and state-dependent friction. *Journal of Geophysical Research: Solid Earth*, 105.
- Ma, S., Custódio, S., Archuleta, R. J., & Liu, P. (2008). Dynamic modeling of the 2004 Mw 6.0 Parkfield, California, earthquake. *Journal of Geophysical Research: Solid Earth*, 113.
- Metropolis, N., Rosenbluth, A. W., Rosenbluth, M. N., Teller, A. H., & Teller, E. (1953). Equation of State Calculations by Fast Computing Machines. *The Journal of Chemical Physics*, 21.
- Neves, M., Peng, Z., & Lin, G. (2022). A High-Resolution Earthquake Catalog for the 2004 Mw 6 Parkfield Earthquake Sequence Using a Matched Filter Technique. *Seismological Research Letters*, 94.
- Noda, H., Dunham, E. M., & Rice, J. R. (2009). Earthquake ruptures with thermal weakening and the operation of major faults at low overall stress levels. *Journal of Geophysical Research: Solid Earth*, 114.
- Olsen, K. B., Day, S. M., & Bradley, C. R. (2003). Estimation of Q for Long-Period (>2 sec) Waves in the Los Angeles Basin. *Bulletin of the Seismological Society of America*, 93.
- Premus, J., Gallovič, F., & Ampuero, J.-P. (2022). Bridging time scales of faulting: From coseismic to postseismic slip of the M_w 6.0 2014 South Napa, California earthquake. *Science Advances*, 8.
- Rice, J. R. (2006). Heating and weakening of faults during earthquake slip. *Journal of Geo-*

physical Research: Solid Earth, 111.

Rice, J. R., & Ben-Zion, Y. (1996). Slip complexity in earthquake fault models. *Proceedings of the National Academy of Sciences*, 93.

Sambridge, M. (2013). A Parallel Tempering algorithm for probabilistic sampling and multimodal optimization. *Geophysical Journal International*, 196.

Schmedes, J., Archuleta, R. J., & Lavallée, D. (2010). Correlation of earthquake source parameters inferred from dynamic rupture simulations. *Journal of Geophysical Research: Solid Earth*, 115.

Tarantola, A. (2005). *Inverse Problem Theory and Methods for Model Parameter Estimation*. SIAM.